Improving the Utilization of Remote Sensing Data for Land Cover Characterization and Vegetation Dynamics Modelling

Liya Sun

München 2016

Improving the Utilization of Remote Sensing Data for Land Cover Characterization and Vegetation Dynamics Modelling

Liya Sun

Dissertation
an der Fakultät für Geowissenschaften
der Ludwig-Maximilians-Universität
München

vorgelegt von
Liya Sun
aus Shandong, China

München, den 08.09.2016

"The diversity of the phenomena of nature is so great, and the treasures hidden in the heavens so rich, precisely in order that the human mind shall never be lacking in fresh nourishment."

-- Johannes Kepler

ZUSAMMENFASSUNG

Die Landoberfläche und ihre Beschaffenheit beeinflussen maßgeblich Wasser- und Energieaustauschprozesse zwischen Boden und Atmosphäre. Häufig stellt die Landoberfläche aufgrund ihrer ausgeprägten räumlichen oder zeitlichen Variabilität ein äußerst komplexes System dar, wobei ihre Variabilität entscheidend durch die Landnutzung geprägt wird. Daher stellen Informationen zur Landnutzung und ihrer dynamischen Veränderung über die Zeit wichtige Eingangsgrößen für die skalenübergreifende Modellierung der Interaktionen von Landoberfläche, Pflanzen und Atmosphäre dar. Das Projekt „CAOS - "From Catchments as Organised Systems to Models based on Dynamic Functional Units" setzt daher einen Schwerpunkt auf die Verbesserung der Beschreibung von Eigenschaften der Landoberfläche für die Modellierung mesoskaliger Einzugsgebiete. Ziel der vorliegenden Arbeit, die im Rahmen des CAOS Projektes umgesetzt wurde, ist die Gewinnung räumlich verteilter Landnutzungsinformationen sowie die Beschreibung der Vegetationsdynamik unter Verwendung fernerkundlicher Methoden.

Fernerkundliche Methoden ermöglichen die Analyse großer Gebiete und stellen Landnutzungsdaten zu unterschiedlichen Zeitpunkten zur Verfügung. Aufgrund dieser Vorteile, wurden sie vielfältig zur Gewinnung von Informationen für Landoberflächenstudien eingesetzt. Die meisten dieser Methoden zur Klassifizierung unterschiedlicher Landnutzungen basieren auf der Auswertung von Bildern im sichtbaren und nahen Infrarot (VIS/NIR) Bereich des Lichtes. Im Gegensatz dazu, wurden die Einsatzmöglichkeiten von Thermalbildern (TIR) für die Beschreibung der Landnutzung bislang weniger ausführlich untersucht. Thermalbilder geben die Landoberflächentemperatur, die in enger Beziehung zu Wasser- und Energieflüssen an der Oberfläche steht, wider. Daher wurden Thermalbilder häufig als Eingangsdaten für die Modellierung der Energiebilanz der Erde, Bodenwasserverfügbarkeit sowie Verdunstung verwendet. Die Nutzung von thermalen Daten wird zusätzlich durch die immer wachsende

Zahl an thermalen Satellitensensoren vorangetrieben. Eines der Ziele dieser Arbeit ist daher, den Wert von TIR Daten für die Landnutzungsklassifizierung zu untersuchen.

Hierfür wurde eine umfassende Analyse der TIR und VIS/NIR Bänder von Landsat-Bildern durchgeführt. Im Gegensatz zu anderen Studien, die die Entwicklung von Klassifizierungsalgorithmen zum Ziel haben, wurde der Schwerpunkt in dieser Arbeit auf die Untersuchung der Charakteristika der Landsat-Bilder gelegt. Als Klassifizierungsalgorithmus wurden daher zwei bewährte Methoden, der „*k*-fold nearest neighborhood" Algorithmus sowie der etwas komplexere „Random Forest" Klassifikator, verwendet. Als Bildfeatures wurden Kenngrößen, die sich aus zwei bis sieben Bändern zusammensetzen, berechnet und zur Auswertung von Einzelbildern sowie Zeitreihen von Bildern herangezogen. Zur Quantifizierung der Unsicherheiten der Klassifizierungsergebnisse wurden sowohl pixelbasierte als auch polygonbasierte Kreuzvalidierungen („cross validation)" durchgeführt.

Es zeigte sich, dass die Berücksichtigung von TIR Informationen sowohl für Einzelbild- als auch Zeitreihenanalysen zu einer deutlichen Verbesserung der Klassifizierungsgenauigkeit führt. Aufbauend auf den Ergebnissen der pixelbasierten Kreuzvalidierung, führt die Integration von TIR Daten zu einer Steigerung der Gesamtgenauigkeit von 5% bzw. 6% für Einzelbilder der Landsat 8 Level 2 und Level 3 Daten sowie zu einer Erhöhung der Genauigkeit um 0.9% bzw. 3.6% für Zeitreihen von Landsat-Bildern der Levels 1 und 2. Bei Verwendung der polygonbasierten Kreuzvalidierung führt die Verwendung von TIR Bildern zu einer Verbesserung der Klassifizierung um 5% bzw. 12% für Einzelbilder der Levels 2 und 3. Im Unterschied hierzu führen der pixel- und polygonbasierte Validierungsansätze zu unterschiedlichen Ergebnisse bei der Analyse von Zeitreihen. Die Unterschiede in der Gesamtgenauigkeit liegen bei 4.5% bzw. 10% für Produkte der Levels 1 und 2. Diese Diskrepanz ergibt sich vorwiegend aus der Unsicherheit der pixelbasierten Methode, die sich durch die Korrelation von benachbarten Pixeln ergibt. Diese entsteht durch Erhöhung der Thermalbildauflösung durch „Resampling". Zusammenfassend kann gesagt werden, dass die

zusätzliche Verwendung von TIR Daten, neben VIS/NIR Daten, für die Klassifizierung der Landnutzung sinnvoll erscheint. Die Bewertung der Ergebnisse sollte in diesem Falle mithilfe einer polygonbasierten Validierungsstrategie durchgeführt werden.

Neben räumlich verteilten Informationen zur Landnutzung, sind räumlich-zeitliche Informationen zur Vegetationsdynamik für das Verständnis der Landschaft und ihrer Prozesse notwendig. Diese Informationen zur Vegetation sind sowohl für hydrologische als auch atmosphärische oder ökologische Studien unumgänglich. Veränderungen in der Vegetation stehen in Beziehung zum lokalen, regionalen, aber auch globalen Klima und beeinflussen wichtige klimatologische, meteorologische und hydrologische Prozesse wie die Speicherung von Kohlendioxid in der Atmosphäre, Verdunstung und Interzeption von Niederschlag. Der „Leaf Area Index" (LAI) dient als Kenngröße zur Beschreibung der Vegetationseigenschaften und wird in einer Vielzahl von Ansätzen zur Modellierung der Vegetationsdynamik verwendet. Der MODIS Satellit stellt ein LAI-Produkt mit höher zeitlicher Auflösung zur Verfügung und bildet daher eine geeignete Grundlage zur Analyse der Vegetationsdynamik. Diese Satelliteninformationen zur Vegetationsdynamik können (nach Nachbearbeitung) als Referenz für die Bewertung von Modellergebnissen genutzt werden.

Die Saisonalität der Photosynthese der Vegetation variiert aufgrund der jährlichen Variabilität des Wetters. Während die meisten Modelle nur die Variabilität der Temperatur berücksichtigen, fließt diese Klimavariabilität nur in komplexere Vegetationsdynamik-Modelle ein. Neueste Studien zeigen, dass eine Veränderung des Niederschlags zu einer Veränderung der Pflanzenphänologie und des Kohlenstoffaustausches führen könnte. Trotzdem wurde der Zusammenhang zwischen Niederschlag und Phänologie bis heute relativ wenig untersucht. In dieser Arbeit wurde ein neues Modell (TPVM - „temperature-precipitation vegetation dynamic model") zur Vorhersage der zeitlichen Veränderung des LAI mithilfe von Informationen zu Niederschlang und Temperatur entwickelt.

Die grundlegende Annahme dieses Modells ist, das Laubbäume im Sommer aktiv, im Winter inaktiv sind. Die LAI Zeitreihe wird mithilfe einer logistischen Funktion der Temperatur und des Niederschlags ermittelt. Das Potential dieses neuen Modells wurde durch den Vergleich mit zwei gängigen temperaturabhängigen Modell, dem „Double Logistic Model (DLM)" und dem „Canopy Structure Dynamic Model (CSDM)" evaluiert. Als Referenz zur Bestimmung der Modellgüte wurden Freilandmessungen herangezogen. Im Vergleich mit dem MODIS LAI Produkt und den modellierten LAI Werten der beiden Modelle DLM und CSDM, erreichte das hier beschriebene Modell TPVM die höchste Übereinstimmung mit den Feldmessungen. Deutlich bessere Ergebnisse im Vergleich zu den beiden anderen Modellen konnten vor allem für landwirtschaftliche Flächen erreicht werden. In einer weitführenden Analyse von Feedbacks der Klimavariabilität auf die Pflanzenphänologie konnten die dominante Rolle der Temperatur bei Laubwäldern und der kombinierte Einfluss von Temperatur und Niederschlag für landwirtschaftliche Flächen gezeigt werden. Aufgrund seiner Evaluierungsergebnisse eignet sich das TPVM Modell zur Beschreibung der zeitlichen Entwicklung des LAI und somit zur Anwendung in öko-hydrologischen Modellen.

SUMMARY

The land surface is strongly controlling the energy and water fluxes between the above-surface and subsurface systems. The complexity of the land surface system exhibits with large spatial heterogeneity of the land surface properties or high temporal variability of land surface processes. As the essential parts of the land surface system, land cover patterns and dynamic changes are strongly required in the land surface modelling across the temporal and spatial scales. Therefore, in the joint CAOS project ("From Catchement as Organised Systems to Models based on Dynamic Functional Units"), one primary objective is to improve the retrieval of land surface characteristics in a meso-scale catchment. Specifically, standing at the point of view by using remote sensing techniques, great efforts are made in this thesis to derive the spatially distributed land cover information and quantify the vegetation dynamics.

Remote sensing techniques provide multi-spatial and multi-temporal land cover information, which have been successfully applied in a variety of land surface studies. Current land cover mapping studies have been focusing on developing the classification methods by using the visible or near-infrared data (VIS/NIR). However, very limited studies have considered the effectiveness of the thermal infrared (TIR) data. TIR information has been proved to be tightly related to the energy and water fluxes in the land surface system. The land surface temperature (LST) is frequently used as an important parameter for the modelling of land surface energy balance, or the evaluation of surface moisture and evapotranspiration. Moreover, the development of satellite instruments have promoted the availability of TIR data. The valuable TIR data captured by the current satellite sensors should be fully exploited. Therefore, one of our objectives is to investigate the usefulness of the TIR data in the land cover classification.

A comprehensive study of the TIR and VIS/NIR bands from the Landsat images was conducted. Contrary to previous studies with tremendous efforts on developing the classification algorithms, the essential characteristics of the Landsat data are paid more

attention in this work. Therefore, the simple *k*-fold nearest neighborhood algorithm and advanced random forest method were selected as the classification algorithms. In the aspect of the data features, different variants were derived from the Landsat images ranging from two bands to seven bands composition. From the temporal scales, both single-date and multi-temporal Landsat images were evaluated. Furthermore, the classification results were analyzed by the pixel-based and polygon-based cross validation (CV) methods for uncertainty assessment.

The classification results of both single-date and time series of Landsat images showed that the inclusion of the thermal information could considerable improve the accuracy of the land cover classification. Based on the pixel-based CV method, the combination with the thermal band improves the overall accuracy (OA) by 5% and 6% for the single-date Landsat 8 image in Level 2 and Level 3 category and by about 0.9% to 3.6% for the time series of Landsat images in Level 1 and Level 2 category. Additionally based on the polygon-based CV method, the improvement of single-date image when including TIR data is clear for the Level 2 and Level 3 category with 5% and 12% respectively. Whereas, the pixel-based CV and polygon-based CV method retrieved slightly distinct results for the time series of Landsat images with the difference of OA from 4.5% to 10% for Level 1 and Level 2 category. The discrepancy mainly results from the uncertainty of the pixel-based CV method which is affected by the pixel correlation problem of the resampled thermal band. Additionally, the polygon-based CV method effectively complements the uncertainty assessment in order to reduce the influence of the correlated pixels. All in all, for the future studies, the thermal bands are recommended to be integrated with the VIS/NIR data for the land cover classification. And when the resampled thermal images are used, the polygon-based CV method would be more appropriate for the accuracy assessment.

Besides the spatially distributed land cover information, as well as the spatio-temporal information of vegetation dynamics need to be quantified in understanding the landscape. The

importance of vegetation canopies could never be neglected when studying the hydrological, atmospheric, or ecological systems. Changes in vegetation cover occurring at the spatial or temporal scales interact with the local, regional or global climate. The vegetation dynamics influence the atmospheric carbon storage or release and crucially affect the fundamental hydrological process such as the evapotranspiration and rainfall interception. Leaf area index (LAI) serving as the representative proxy of the vegetation attributes have been frequently used in vegetation dynamics modelling. Especially, the LAI product provided by the MODIS satellite program has the pronounced potential in observing the terrestrial vegetation dynamics with high-temporal frequency. The temporal LAI data from satellite products after preprocessing could be used as the reference data for the vegetation dynamics modelling.

The seasonality of photosynthesis of the vegetation canopy varies according to the year-to-year weather variability. Considerable vegetation dynamics models take the climate variability into account, whereas most of the models are developed solely relying on the temperature variability. Current studies have reported that the shifts in precipitation may modify the vegetation phenology and C exchange. However, the precipitation interaction with the vegetation phenology has rarely been investigated. By integrating the two climate variables, a new temperature-precipitation vegetation dynamic model (TPVM) was set up in this work for the temporal LAI prediction.

The fundamental assumption of the new model follows the general characteristic of deciduous canopies as summer active and winter dormant in nature. The model derives the time series of LAI based on the logistic functions with the cumulative daily temperature and precipitation as input. The capability of TPVM was evaluated by comparing with two typical temperature-dependent models, the Double Logistic Model (DLM) and the Canopy Structure Dynamic Model (CSDM). Using the field measured LAI data as reference, TPVM retrieved the best LAI values compared to the original MODIS LAI product and the modelled LAI data from DLM and CSDM. Besides, TPVM performed comparably well as the DLM for the deciduous forest

and surpassed the two models for the agricultural land covers. Further phenological metrics analysis about the feedbacks of the climate variability on the vegetation dynamics demonstrate that the dominance of the temperature on deciduous forest and the coherent influence of temperature and precipitation on the agricultural croplands. Consequently, the simple TPVM model is qualified to predict the temporal LAI profiles and could be further incorporated into the eco-hydrological models.

ACKNOWLEDGMENTS

who has been helping and encouraging me since I was an undergraduate student. He is always so kind for everything and cares us like a father.

I wish to thank the brilliant colleagues in LMU and BOKU for all the happy time we spent. I am very grateful to Dr. Matthias Bernhardt, Dr. Mathew Herrnegger, Dr. Bano Mehdi, Dr. Tobias Hank, and Dr. Monika Prasch for sharing ideas, providing datasets and field measurement experiences with me. My deepest thanks also go to the loveliest and my dearest PhD fellow students from the working group, Christina Elisabeth Thiem, Claire Brenner, Stefan Härer, Benjamin Müller, Lu Gao, Lu Dong, Benjamin Apperl, Johannes Fischer, Daniel Klotz, the dinner-girls and all the nice colleagues in the department. No matter for work or life, you guys have been unconditionally helping me and sharing fantastic ideas with me. It is my great honor to work with you and have so much fun in the past years.

Last but not least, I want to thank my husband, Senmao, with all my heart. I could never go through this without your persistent encouragement, tolerance and love. I am indebted to you for all your contribution to our little family. I deeply appreciate that you took the challenge of coming here by giving up the job in Beijing. You and our lovely boy have been the happiness source for me to continue my work. And my infinite thanks go to my parents for their unlimited love and trust. Thank you for giving me life, raising me up and uncomplainingly supporting me for everything. To you, this work is dedicated.

TABLE OF CONTENTS

LIST OF FIGURES

LIST OF TABLES

1   INTRODUCTION

1.1   Background and Motivation

1.1.1   Land Surface Process

The land surface plays an important role within the hydrological, atmospheric, meteorological, climatological, and remote sensing communities (Bonan, 1998; Coudert, Ottlé, & Briottet, 2008; Sabater et al., 2008). In the last decades, various Land Surface Models (LSM), Soil–Vegetation–Atmosphere-Transfer (SVAT) or Surface Energy Balance (SEB) models have been designed to simulate the interactions between plant canopy processes and the environment. These models are very useful for the quantification and understanding of energy and water fluxes between the different parts of the ecosystem (F. Chen & Dudhia, 2001; P. J. Sellers et al., 1996; Piers J. Sellers et al., 1996). In land surface modelling (Figure 1.1), characteristics of land cover govern many eco-hydrological variables, such as the surface roughness for energy transfer, albedo for solar absorption, moisture from canopies and soils, and mechanisms for water runoff (Dickinson, 1995). Land cover categorization and property representation of distinct land cover types such as the leaf area index (LAI) of plants are of vital importance for depicting the energy or water balance process. Traditional field measurement of the land cover types is very time-consuming and sophisticate modelling of vegetation LAI is too complicated to retrieve the effective process parameters for the eco-hydrological models (Schulz et al., 2008). Therefore, this work aims at improving the land cover classification by fully exploiting the thermal infrared (TIR) and visible/near-infrared (VIS/NIR) information of the remote sensing data (RS) and developing a simple parsimonious vegetation dynamic model based on the meteorological data by utilizing the time series of RS data.
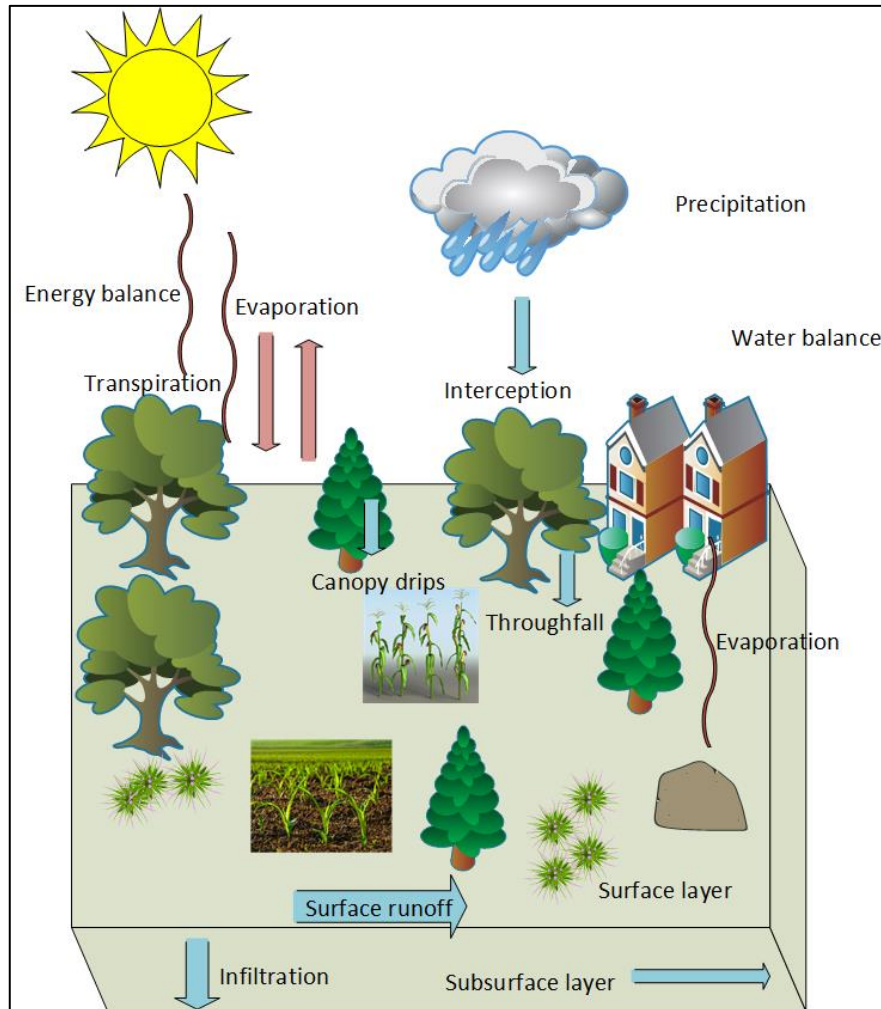
Figure 1.1 The generalized land surface processes with various land cover types, inspired by the land surface model Noah (Chen et al., 1996).

1.1.2 Land Cover Categorization

In the land surface system, land cover and land use have different definitions. Land use indicates the human activity on the land influenced by various human-related arrangement such as the economic or cultural factors (Rozenstein and Karnieli, 2011). Whereas, land cover refers to the observed biophysical cover of the terrestrial surface, of which the specific types can be identified by using the remotely sensed imagery including vegetation, water courses, bare soil or settlement (Gómez et al., 2016). Land cover serves as one of the basic variables in ecological

modelling, climate system research, as well as in hydrological process studies (Carlson and Traci Arthur, 2000; Herold et al., 2006).

For example, land cover data provide valuable information to predict the distribution of both individual species and species assemblages, or the detailed habitat heterogeneity data for the ecosystem (Kerr and Ostrovsky, 2003). Land cover information affects the climate system in a various ways and has the direct interaction with the surface solar and longwave radiation and the fluxes changes of the atmospheric turbulence or the carbon uptake (Mahmood et al., 2010; Pielke et al., 2011). In addition, the land cover information can be used to determine runoff coefficients and to characterize infiltration, erosion, and evapotranspiration for distributed hydrological models (Dubayah et al., 2000; Hansen and Goetz, 2006; Liang et al., 1999). In the ecological modelling, Moreover, global and small-scale annual changes of land cover types, vegetation cover, the degree of imperviousness (Carlson and Traci Arthur, 2000), all have major effects on the behavior and response of hydrological systems from the plot, via the hill slope to the catchment and basins scale (Houghton et al., 2012; Running et al., 1999). Processes altered include the infiltration of rainfall, overland flow and the amount of evapotranspiration that are controlled - besides atmospheric conditions – by the physiology of the underlying vegetation (Figure 1.1). Especially at the meso-scale, spatial pattern of land (sub)surface conditions have shown to strongly effect hydrological response and eco-hydrological system behavior (Cihlar et al., 2000). In this sense, reliable categorization of land cover types has notable meanings for the land surface process study.

1.1.3 Vegetation Dynamics Modelling

Vegetation canopies have a number of prominent functions in the biosphere and affect the ecosystem in various spatial and temporal scales (Goward and Prince, 1995). The vegetation dynamics are regarded as indicators for evaluating the interactions between the water cycle, climate and terrestrial systems (Sitch et al., 2003). Intrinsically coupled with the water cycle,

the distribution and productivity of terrestrial vegetation interact strongly with the water balance (Churkina et al., 1999; Stephenson, 1990). Many SVAT models explicitly consider the role of vegetation in affecting water and energy balance by taking into account its physiological properties (Arora, 2002). Researchers summarized three dominant physiological and structural characteristics affecting the evapotranspiration that include the leaf area, photosynthetic rate and the rooting depth (Eamus, 2003; Zhang et al., 2001). However, most of the eco-hydrological models usually include the vegetation as a static parameter in spite of the key role of vegetation in the water balance. In particularly, as one of the important state variables, many eco-hydrological applications (e.g. SVAT, SEB) still use the constant monthly value of one specific vegetation type instead of the dynamic LAI values from year to year (Su, 2000). The easily-derivable and physically-reasonable vegetation dynamics model in the sense of LAI values is strongly required.

1.1.4 Remote Sensing Techniques

With low-cost, fast and repeated monitoring of land surface, satellite images have been long utilized in the land cover mapping and change detection for more than 40 years (Byrne et al., 1980). Figure 1.2 lists the historical and planned satellite sensors relating to the vegetation dynamics and land cover monitoring (Houborg et al., 2015). Since 1970s, Landsat 1 was launched with the Multispectral Scanner System (MSS) sensors onboard and started the Landsat legacy at the forefront of space-based Earth observation. Landsat missions have been developed from only four spectral bands (green, red, and two NIR bands) in Landsat 1, to seven bands (with VIS/NIR and TIR bands) in Landsat 4/5, and to the 11 spectral bands of the nowadays Landsat 8 with two instruments of the Operational Land Imager (OLI) and the Thermal Infrared Sensor (TIRS) recording in. Following the Landsat mission, a number of medium resolution and high spatial resolution satellite sensors have been launched to provide large-scale images for the global, continental, or regional scale land cover mapping, as well as

ocean or atmosphere studies (Giri et al., 2013). Frequently-used products comprise the 1km Advanced Very High Resolution Radiometer (AVHRR) with five spectral bands, 250m-1km Moderate Resolution Imaging Spectroradiometer (MODIS) aboard Terra and Aqua platforms recording in 36 spectral bands, 1km SPOT-VGT with four spectral bands and the 300m -1.2km and MEdium Resolution Imaging Spectrometer (MERIS) with 15 VIS/NIR bands on Envisat. Among all these earth observation programs, because of the high-quality multiple VIS/NIR and TIR spectral datasets, Landsat and MODIS products freely distributed by NASA have attracted numerous researchers for the land cover mapping (Friedl et al., 2002; Oetter et al., 2001; Steele et al., 1998), change detection (Maximov, 2003; Muttitanon and Tripathi, 2005; Shalaby and Tateishi, 2007), vegetation mapping and seasonal variation analysis (Chandola et al., 2010; Feng et al., 2008; Reed et al., 1994; Xie et al., 2008).
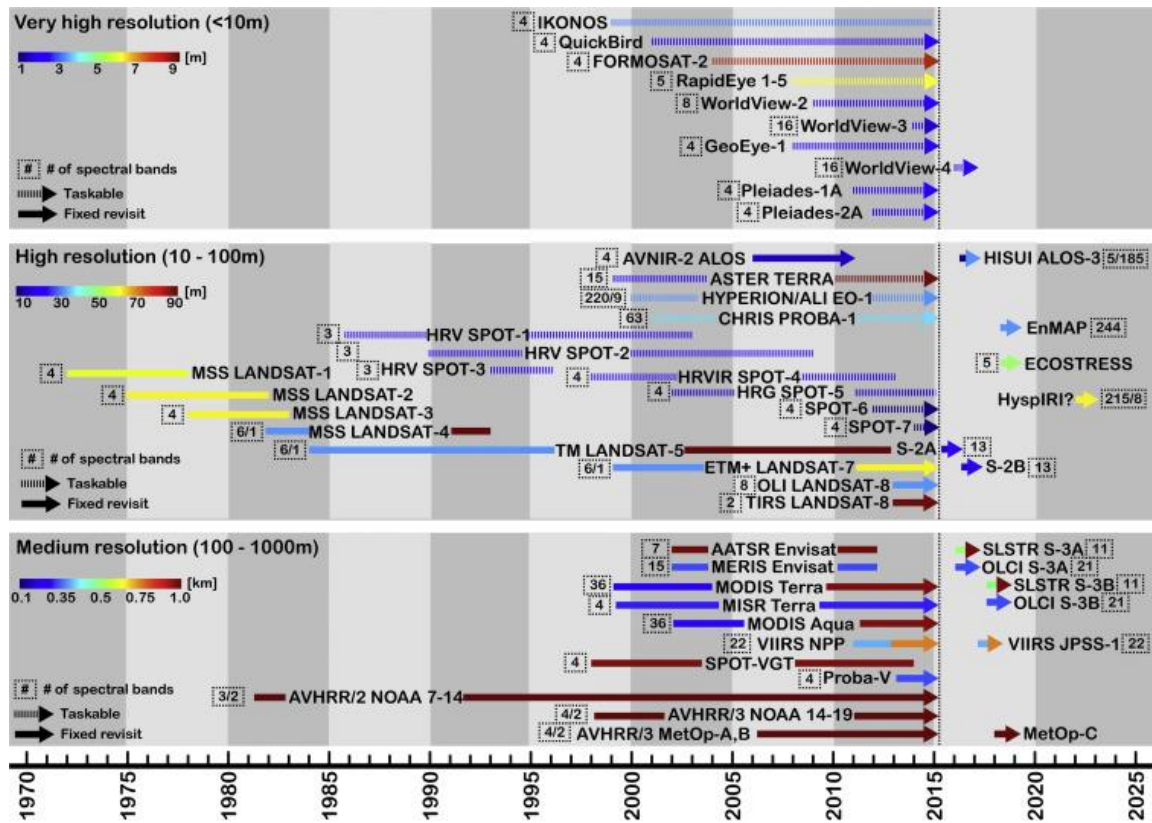
Figure 1.2 Timelines of historical and planned multi- and hyperspectral optical and thermal satellite sensors relevant for remote sensing of vegetation at medium to very high spatial resolution, cited from (Houborg et al., 2015).

1.2   State of the Art in Land Cover Classification

1.2.1 Development of Land Cover Classification Methods

The spatially explicit land cover information recorded by the satellite sensors can be recognized through the classification of the RS images. The increasing emergence of the remote sensing techniques also accelerated the development of classification methods in the land cover mapping. Diverse classification approaches have been proposed including the supervised or unsupervised, parametric or nonparametric, and hard or fuzzy classification methods (Lu and Weng, 2007). Specifically, the numerous classification algorithms range from the simple

unsupervised cluster analysis to the advanced classification algorithms, such as the expert systems (Lucas et al., 2007; Zhang and Zhu, 2011), random forest trees (Gislason et al., 2006; Rodriguez-Galiano et al., 2012a; Rodriguez-Galiano et al., 2012b), artificial neural networks (Bischof et al., 1992; Brown et al., 2008), support vector machines (Huang et al., 2002; Vuolo and Atzberger, 2012), or fuzzy sets (Foody, 1996; Pérez-Hoyos et al., 2012).

However, despite the intensive achievement of classification algorithms in the land cover mapping with remotely sensed images, Wilkinson (2005) quantitatively investigated over 500 classification experiments and reported that the classification performance has shown no significant improvement over the 15-year period. He pointed out that one possible reason could be that the improvements in the classification algorithms are too small to have any appreciable effect on the field. Manandhar et al. (2009) concluded that it is of minor value to further continue developing the classification algorithms. Instead, research should be more concerned about the essence of the geographic datasets (Stefanov et al., 2001). This includes the exploration of the multiple features of RS data using the image transformation methods (e.g. principle component analysis (Linders, 2000); the use of various spatial texture information (Clausi, 2002); the integration of RS with geographic information system techniques (GIS), data fusion of VIS/NIR bands with radar data or aerial photographs (Ban, 2003; Geneletti and Gorte, 2003) or with pan band (Shi et al., 2003); or the combination of multi-temporal data (Amorós-López et al., 2013; Claverie et al., 2012; Yuan et al., 2005). In accordance with these conclusions, this work pays more attention on investigating the potential of Landsat VIS/NIR and TIR datasets within the classification process. Just two supervised classification methods are selected here for the land cover classification, the simple k-fold Nearest Neighborhood (k-NN) and the advanced Random Forest (RF) algorithm.

1.2.2 TIR for Land Cover Classification

The traditional supervised classification procedure follows the way of choosing the appropriate data sources, constructing the suitable classification definition set, image preprocessing, selection of representative training samples, feature extraction, performing the classification algorithms, post-classification processing, and accuracy assessment (Anderson, 2005; Lu and Weng, 2007). An appropriate dataset is significantly important and needs to be determined in the first place.

Most of the previous studies using the single or multi-temporal Landsat images mainly investigated the effectiveness of the 30m VIS/NIR bands for land cover classification. For example, Byrne et al. (1980) performed the principle component analysis (PCA) on two Landsat scenes of four-channel VIS/NIR bands on different dates to monitor the land cover change. Guerschman et al. (2003) explored the use of multi-temporal Landsat TM data from the same growing season for the classification of land cover types in the south-western portion of the Argentine Pampas and investigated about the necessary dates for an accurate classification. Several researchers detected the LUCC using the multi-temporal satellite images or transformed VIS/NIR band indices for the study areas all over the world (Lambin et al., 2003; Lunetta et al., 2006; Muttitanon and Tripathi, 2005; Shalaby and Tateishi, 2007; Yuan et al., 2005). They either worked to improve or set up new classification algorithms, or transform the VIS/NIR bands to the representative spectral components, or combine multi-temporal Landsat VIS/NIR images. But very limited researches have been conducted in evaluating the TIR efficiency in the land cover classification.

TIR remote sensing provides continuous representation of the land-surface temperatures (LST) (Kustas and Anderson, 2009), which are directly linked with the eco-hydrological processes. The thermal information characterizing the energy balance at the land surface can be applied in a variety of fields, such as the identification of catchment functional units (Müller et al.,

2014), urban heat islands pattern monitoring (Li et al., 2013), land surface energy fluxes and evapotranspiration estimation (Kustas and Anderson, 2009). However, only very few researchers have investigated the effectiveness of the Landsat thermal band for improving the land cover classification (French et al., 2008; Southworth, 2004). Southworth (2004) investigated the Landsat TM thermal band in the land cover analysis of tropical dry forest regions and reported that the thermal band contains considerable information for the discrimination of land cover classes and the thermal band also outperformed many of the individual bands of information. Eisavi et al. (2015) evaluated the multi-temporal Landsat 8 data for the land cover mapping and demonstrated that the multi-temporal thermal and spectral information can be complementary rather than redundant. However, to what extent or how the thermal information can be fully exploited in order to further improve the land cover classification still needs further investigation and is a focus of this research..

1.3 Vegetation Dynamics and Remote Sensing Techniques

1.3.1 Vegetation Dynamics Modelling

Previous studies have shown that the vegetation dynamics can be simulated in various ways by modelling the bidirectional interactions between climate and vegetation. Moreover, the studies of vegetation dynamics could be addressed at different spatial scales such as the species distribution, shifts or size (deforestation), structural and physiological characteristics, and at temporal scales from millennia to decades with the shifts of reproduction age, succession stage, and, most importantly, phenology (Thuiller, 2007). For example, the process-based simulation of the vegetation dynamics such as the dynamic global vegetation model (DGVM) follows the ecophysiological principles by exploring the influencing factors during the past, current and future on the distribution of plant functional types at the regional or global scales (Prentice et al., 2007; Scheiter et al., 2013). However, such dynamic vegetation models are quite complex and have high parametrical requirements. In operational applications the DGVM may be

limited by the "data-hungry" phenomenon and need large amount of direct observations for the model parameters (Hartig et al., 2012). Therefore, this work aims at developing a simple parsimonious vegetation dynamic model for a mesoscale catchment, with spatially-explicit and varying seasonal LAI values by integrating the remotely sensed data with the meteorological observations.

1.3.2 Climate Controls on the Vegetation Dynamics

Before assuming the structure of the vegetation dynamic model, the relationship between the vegetation LAI and the climate controls needs to be reviewed. In spatially distributed eco-hydrological modelling, seasonal and inter-annual vegetation dynamics are considered to be directly linked to the phenology patterns of the ecosystem (Evrendilek and Gulbeyaz, 2008). Phenology of plants has been altered by climate warming over the past 50 years and may be an important mechanism behind ecosystem response to global change in the future (Morisette et al., 2008). Moreover, scientists evaluated the climate change in local, regional or global scales and conclude that the species ranges of plants, phenology, primary productivity, biomass and the vegetation-climate relationships have been significantly altered (Chen et al., 2010; Cleland et al., 2007; D'Arrigo et al., 2004; Krishnaswamy et al., 2014; Nemani et al., 2003; Parmesan and Yohe, 2003). For example, the spring green-up or autumn senescence time of different vegetation types, or the amplitude and length of growing season vary year from year affected by the climate change. Correspondingly climate controls can influence the LAI values then affect the canopy interception of precipitation and surface energy balance in the distributed hydrological models (Bastiaanssen et al., 1998; Cleland et al., 2007; Schwartz et al., 2006; Su, 2000).

The temperature control has been intensively studied in the phenology model indicated by the cumulative temperature or growing degree days (Leith, 1974). However, very limited studies have explicitly investigated the precipitation controls on the LAI variation during the plant

growth stages. Grier and Running (1977) proposed that the precipitation input, soil water storage and atmospheric evaporative demand appears to be the dominant control of the leaf area index (LAI) and net primary production (NPP) in forests of the northern-western United States. Richardson et al. (2013) reviewed the studies on the interactions between the climate change and phenology in a climate system and provided a valuable qualitative understanding for other researchers. He summarized that the shifts in temperature and precipitation driven by climate change will likely cause shifts in the phenology of carbon budgets in many ecosystems. The magnitude of interactions and feedbacks between temperature-precipitation and the vegetation dynamics of LAI values still need to be precisely quantified. In this work, a vegetation dynamic model is developed to predict the spatially distributed LAI dynamics in a mesoscale catchment by simulating from a phenological perspective using cumulative temperature and precipitation data.

The phenology of vegetation normally refers to the timing of the recurring plant growth stages, such as the start time of leaf emergence, the time of maximum leaf areas or the time of leaf senescence. Therefore, in this sense, the seasonal variations of LAI could be used as indicators of vegetation phenology and could possibly be expressed following the philosophy of the phenology model to present the relationship between the LAI and climate controls. Plant phenology models generally include three main types: theoretical, statistical and mechanistic models. Theoretical models are designed to understand the evolution of leaf lifespan strategies rather than the annual variation, e.g. defining the phenology based on the prescribed leaf onset and offset dates (Chuine et al., 2003). Statistical phenology models use the simple or complex relationship between the timing of phenological events (e.g. the leaf-on, leaf-off) and the climatic controls (Emberlin et al., 1997; Schwartz, 1998; Schwartz and Karl, 1990). Mechanistic phenology models have a long ongoing development and normally assume the cause-effect relationships between the biological process and the driving factors, which describe the plant development responses to the temperature with various functions

representing the forcing or chilling process (Chuine, 2000; Chuine et al., 1999; Liang and Schwartz, 2009; Richardson et al., 2006; Schwartz et al., 2006). However, these models are mainly developed based on the field measurements or for one specific vegetation type and are limited in the application for larger regions.

Nowadays, compared to the traditional modelling ways based on the climate controls and the time-consuming phenological observation data, satellite data has been more and more applied to detect the vegetation phenological change within the grid pixel scale (White et al., 1997). Despite the advanced development of phenology models by using the RS data (Baret and Vintila, 2003; Schwartz et al., 2002; White and Nemani, 2006), comprehensive investigation by integrating satellite products and the meteorological observation still require further efforts in retrieving the dynamic vegetation properties for the spatially-distributed eco-hydrological model. To this intent, our work takes the MODIS LAI products to investigate the LAI variations of different vegetation types using the climate data.

1.3.3 LAI Prediction Integrating the Meteorological Data and Satellite Data

LAI is defined as the total one-sided area of leaf tissue per unit ground surface area (Watson, 1947). As one of the representative characteristics of vegetation dynamics, LAI serves as an important component in many climate or hydrological models and closely links to key ecological processes such as photosynthesis, transpiration, and evapotranspiration, and can be used to estimate net primary productivity (NPP) and other quantities (Jiang et al., 2010). Continuous and long-term monitoring of LAI contribute significantly for the vegetation dynamics analysis in productivity or climate change study in the ecosystem (Zheng and Moskal, 2009). With non-destructive, cheap and large spatial scale observation, RS techniques provide repetitive observations of the land surface and can well capture the vegetation status from space.

The retrieval methods of LAI values from the optical RS data can generally be conducted by several methodologies. Frequently used methods include: the empirical relationship between LAI and VIs; inversion of physically based canopy radiative transfer models (RTM); the use of look-up tables (LUT) or other algorithms such as neural networks. The VIs derived from the satellite images mainly depend on the contrast vegetation reflectance characteristics in the solar spectrum that with the increase of vegetation LAI, visible reflectance declines and simultaneous NIR reflectance increases (Verstraete et al., 1996). The robust feature of plants also promotes the fast development of vegetation indices (VIs) application with the satellite images. VIs minimize the disturbing influences of soil background or differences in atmospheric conditions, or the terrain related illumination differences (Atzberger et al., 2011). Satellite-derived VIs can be used as proxies for vegetation parameters such as the fractional vegetation cover (fc) and LAI (Glenn et al., 2008). For example, theoretical and field studies have shown that the normalized difference vegetation index (NDVI) is near-linearly related to photosynthetically active radiation (fPAR) absorbed by the plant canopy and non-linearly related to the LAI values (Pettorelli et al., 2005). But the empirical relationship between LAI and VIs have difficulties in accounting for the complex vegetation processes and the relationship may not be stable for the large area. On the other hand, the RTM can explicitly exploit the physical process of radiation interaction within the vegetation but has been limited by the expensive computational requirements and optimal inversion solutions (Fang et al., 2003). LUT or NN methods are promising and simple to use but not generalized to handle the arbitrary directional and spectral combinations (Kimes et al., 2000). Initializing from the perspective of the canopy structure dynamics model, the temporal changes of vegetation LAI are mainly governed by the plant growth and closely influenced by the environmental factors. The generalized expression between the climate factors and the leaf area could be explored for the LAI prediction. Therefore, this work takes this vegetation growth feature into account and aims to set up a simple parsimonious model using the climate data and primarily simulate the LAI results using the satellite LAI products as reference datasets.

Considering the choice of the satellite data, MODIS products provide the various land, atmosphere or ocean products. Actually, the empirical study between LAI and NDVI started since 1981 when AVHRR by National Oceanic and Atmospheric Administration (NOAA) started to provide the long-term NDVI data sets at coarse spatial scales (8-16 km resolution). But with better quality, NASA scientific teams generate the most abundant VI products using the MODIS data in diverse spatial and temporal scales, which offers great opportunity for the vegetation dynamics studies in meso-scale catchment. As one of the variables directly-related to the eco-hydrological process among the MODIS VIs products, time series of LAI products with 500m or 1000m spatial resolution could offer the great potential in the vegetation dynamics modelling. The MOD15A2H LAI products are retrieved using the main LUT method using 3D radiative transfer equation and a back-up empirical relationship of NDVI and LAI data. MOD15A2H LAI products have been improved by using the higher-quality surface reflectance input data. However even when considered as "good quality", the data can still hardly avoid the deficiency of noises resulting from the atmospheric conditions or the system errors. Therefore, the satellite data must be preprocessed to ensure the constituency of the LAI products before application in the vegetation dynamic model.

1.4   Research Objectives

As two important variables of the land surface characteristics, the land cover types and vegetation dynamics play a predominant role in the in the eco-hydrological processes. Remotely sensed images can provide valuable land surface information and could be continuously used in the spatial-distributed terrestrial system modelling. Especially the thermal information can give a better understanding of the land surface energy distribution which closely related to the land cover types. However, only few investigation have been done in this area. As one of the main objectives, this research is dedicated to exploit the effectiveness of the TIR band from the Landsat images in land cover classification.

The second objective is concerned with the improved representation of vegetation dynamics. As one of the most important proxy of vegetation dynamics, vegetation LAI values need to be accurately predicted. Previous LAI retrieval suffers from the deficiencies of being too simple when based on empirical relationship between VIs and LAI, or too complex and computation-consuming when based on RTM. Therefore, this work aims to develop a simple parsimonious vegetation dynamic model to predict the LAI values by integrating the climate data and the satellite products.

1.5 Structure of the Thesis

The primary idea of this thesis is to improve the RS data utilization in the land surface processes by improving the land cover categorization and better prediction of vegetation dynamics. This work is conducted in a meso-scale catchment in Luxembourg and is closely embedded in the CAOS project (http://www.caos-project.de/). The thesis consists of six main chapters and structured as Figure 1.3. Besides the introduction in Chapter 1, Chapter 2 mainly presents the preprocessing and analysis of the satellite data. As mentioned in the section above, the satellite data usually contain noises due to the atmospheric conditions or sensor view angle differences and other system errors. Therefore, no matter for which objective of this work, the satellite data should be preprocessed and analyzed before the further application.

Chapter2: Preprocessing of Satellite Images:
1) Landsat images preprocessing
2) Land cover change analysis over the past decades
3) Smoothing for MODIS data

Chapter 3: Publication 1- Improvement of land cover classification by thermal remote sensing:
1) Results by the single-date Landsat 8 image
2) Results by the multi-temporal Landsat 4/5 images
3) Accuracy assessment

Chapter 4: Publication 2- Comparison between the pixel-based and polygon-based cross validation methods:
1) Accuracy assessment by the pixel-based cross validation method
2) Accuracy assessment by the polygon-based cross validation method

Chapter 5: Publication 3- Vegetation dynamic modeling:
1) MOD15A2H LAI data smoothing
2) LAI prediction of different vegetation types
3) Evaluation with field measurement and phenological metrics analysis

Figure 1.3 Structure of the thesis

Chapter 2 contains two main parts: the preprocessing of Landsat images and the smoothing methods comparison of MODIS products. For the preprocessing of the Landsat images, the research work attempts to investigate the effectiveness of thermal data in land cover classification using the single-date Landsat 8 image and time series of Landsat 4/5 images. The beforehand land cover change detection could be complementary for the time series of land

cover classification using satellite images from different years. Therefore, besides the general atmospheric correction and geometric correction for all the Landsat images, the LUCC maps for the study periods require to be analyzed: to what extent the changes happen during the past decades, which land cover types may have the largest influences. Secondly, for vegetation dynamics prediction, MODIS data should be filtered before utilization as the reference data for the LAI model. This work compares four smoothing methods for the MODIS VIs data and intends to give an overall performance analysis of the different methods before the further development of vegetation dynamics modeling.

Chapter 3 and Chapter 4 engage in the detailed land cover classification research work and moreover investigate the different accuracy assessment procedure. In order to test the effectiveness of the TIR information, Chapter 3 compares the classification results by using VIS/NIR and TIR information from single-date and time series of Landsat images. Representative variants of channel combinations are derived in order to demonstrate the accuracy differences when adding the thermal band and without the thermal band. When using the resampled thermal band images, the sampling way of the cross validation evaluation could be easily affected. Thus, the evaluation of the different sampling ways (pixel-based or polygon-based) needs investigation for the thermal remote sensing. Chapter 4 follows the same classification procedure while mainly focus on the sampling differences of the training and validation ways in the accuracy assessment.

Chapter 5 aims at developing a new parsimonious vegetation dynamic model, which can easily derive the LAI data with the observed climate data. Following the canopy growth feature that the LAI values are strongly related to the climate factors. As representative examples, temperature and precipitation exert great influence on the vegetation dynamics. Therefore, the proposed model, not solely use the temperature data but also takes the precipitation data into account. Before using the MODIS data in the vegetation dynamic modeling, MODIS LAI products generally need to be smoothed. The smoothing principle is to filter out the sudden

spike points in the time series of LAI data while keep other data points as original as possible. The smoothing method with good performance evaluated in Chapter 2 could fulfill this requirement. Besides, distinct vegetation types respond differently to the climate change and normally could be illustrated by the vegetation dynamics model. Therefore, after the prediction of temporal LAI values, uncertainties evaluation with the field measurement and the frequently-used phenological metrics could serve as the direct indicators and be capable to reveal the responses of vegetation to the temperature or precipitation changes in different years.

Finally, Chapter 6 provides a synthesis and an overall discussion of the land cover classification and vegetation dynamics modelling by the remote sensing techniques. Moreover, Chapter 6 gives specific suggestions for the future researches.

2 Satellite Data Preprocessing and Land Cover Change Analysis

2.1 Introduction

The quality of satellite data determines their effectiveness in characterizing the land surface processes. Remotely sensed data provide valuable sources of information for the land surface monitoring or modelling, however the satellite images are often affected by the atmospheric effects, cloud contamination or physical system limitations (Hadjimitsis et al., 2004; Hilker et al., 2012; Tyagi and Bhosle, 2011).The atmosphere constituents modify the electromagnetic radiation by absorption or scattering when the signals travel through the solar spectrum from the Earth surface to the sensor (Tyagi and Bhosle, 2011). The haze, dust and the adjacency effects can mask the real changes or make similar land cover appear differently for the images at different times. Satellite sensors like the Landsat MSS, TM or ETM are able to detect large parts of the visible/near infrared spectrums. Song et al. (2001) performed land cover classification and change detection using the Landsat TM data by evaluating the various atmospheric correction algorithms and concluded that atmospheric correction is not always necessary for the single image classification. Whereas, it is mandatary for the multi-temporal or multi-sensor images to remove or reduce the atmosphere influence (Lu and Weng, 2007; Wang and De Liberty, 2005).

Besides the atmospheric effects, snow or cloud cover, viewing or illumination geometry effects can also bring noise to the satellite data. The vegetation index products from MODIS are representative examples, even after the Maximum Value Compositing (MVC) within the specific time window (Holben, 1986). The noise often shows at the sudden-fall in the time series of LAI or NDVI data from MODIS with anomalous low values during the vegetation growth stages. The noise in the satellite data should be reduced before further application in the land surface eco-hydrological systems. Numerous smoothing methods have been

investigated using the remotely sensed data, ranging from the famous MVC (Holben, 1986), Best Index Slope Extraction (BISE) (Viovy et al., 1992), modified BISE (mBISE) (Lovell and Graetz, 2001), Asymmetric Gaussian function (AG), Double Logistic function (DL), and Savitzky-Golay (SG) filter embedded in the TIMESAT software (Jönsson and Eklundh, 2004), curve fitting procedure (Beck et al., 2006; Bradley et al., 2007), or the wavelet transform algorithms (Martínez and Gilabert, 2009).

This chapter presents the preprocessing and smoothing of the satellite data, aiming to find a suitable preprocessing way for the Landsat and MODIS data before directly addressing the land cover classification and vegetation dynamics modelling. The following sections introduce the detailed processing and analysis for Landsat images, and the comparison of four smoothing methods for MODIS vegetation products.

2.2 Study Area

The Attert catchment as the main test site of German DFG research project CAOS ("Catchments as Organized Systems") is located in the Midwestern part of the Grand Duchy of Luxembourg and partially in Belgium (Figure 2.1). The catchment covers a total area of 288 km^2. The main land cover types consist of dense deciduous and coniferous forests, spacious pasture and croplands, and a sparse residential area. As shown in Figure 2.1, the catchment has very distinct geologies with a large area of marls, schists and small proportions of sandstones. Correspondingly, most of the dense deciduous and coniferous forests distribute at the northwest part of the schist area and the southeast sandstone areas. The spacious pasture and croplands locate at the middle of the marls area and sparse residential areas spread along the alluvium.
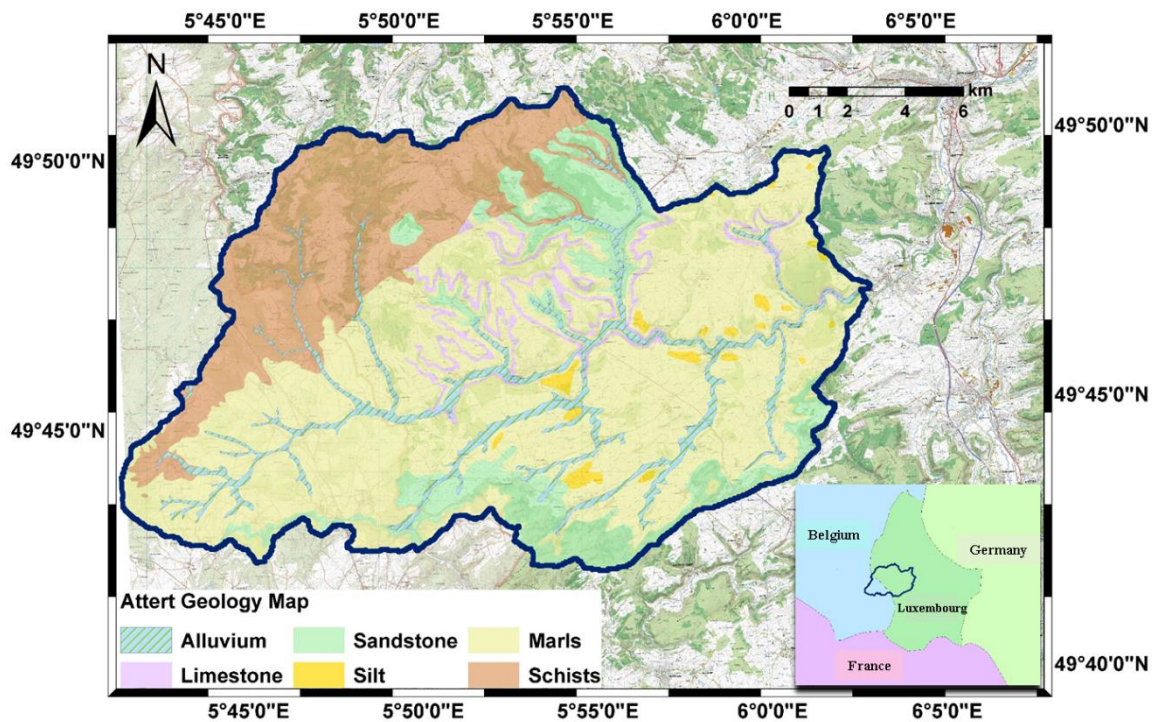
Figure 2.1 The geology and topography map of Attert Catchment from the CAOS project (CAOS, 2012); the right-bottom overview map indicates the location of the Attert Catchment across Belgium and Luxembourg.

According to the CORINE land cover map in 2006, the agricultural area takes up 65% and forest accounts for about 30% of the catchment. The elevation of the Attert basin ranges from 238 m to 539 m. With a temperate climate, the mean monthly temperatures reaches a maximum of about 18 °C in July and a minimum of 0 °C in January. The high summer evapotranspiration from July to September and high flows from December to February is characterized by the mean annual precipitation of 850 mm and the mean annual actual evapotranspiration of 570 mm (1971–2000). Figure 2.2 illustrates the daily mean temperature and cumulative daily sum precipitation variations from 2004 to 2011 in a meteorological station in Attert Catchment around Hovelange, Luxembourg.
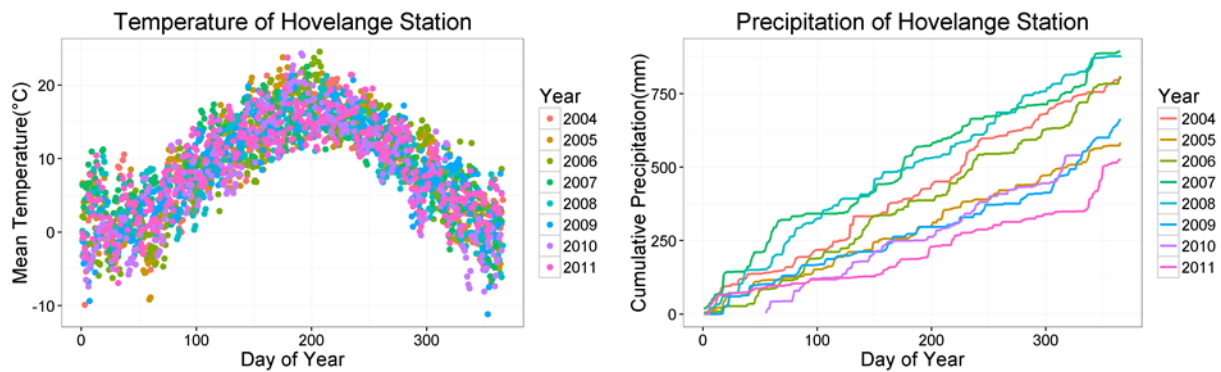
Figure 2.2 Mean temperature and cumulative precipitation variations from year 2004 to 2011 of one example meteorological station in Attert Catchment around Hovelange, Luxembourg.

2.3 Preprocessing and Analysis of Landsat Images

2.3.1 Classification Process

In the beginning of our research project, we were interested to evaluate the possible impacts of land use changes in the catchment on the hydrological responses. Therefore, one research question concerning the land surface characteristics was, how did the land cover and land use change during the past 40 years in the study area. We initially designed our research work to have a general overview of the land cover changes for the Attert Catchment. Figure 2.3 gives the flowchart of the land cover change detection in the Attert Catchment. The change detection procedure includes firstly to collect the Landsat images, then to define the land cover classification scheme, to perform the atmospheric correction, to select the training samples, to classify the Landsat images, to use the majority filter method to derive contiguous neighboring cells, and finally to detect the land cover changes between different years. Here the Level 1 classification scheme was defined with four main land cover classes: artificial area, agricultural area, forest, and water bodies. The Landsat TM images were collected and atmospherically

corrected before classification using the maximum likelihood algorithm (ML). The atmospheric correction was performed by the MOTRAN algorithm in the ATCOR toolbox in ERDAS software (Geosystems, 2013). Afterwards, the training samples were edited by using the clustering method based on the referred Google-Earth maps and the observation map in 2007 provided by the CAOS project. Based on the assumption of normal distributions of the input bands, the ML classifier decides whether a pixel belongs to a particular class based on the Bayesian probability decision rule. The equation uses the covariance matrix to present the variability of classes shown as the Equation 2.1:

$$D = \ln(a_c) - [0.5\ln(|Cov_c|)] - [0.5\,(X - M_c)^T (Cov_c^{-1})(X - M_c)] \qquad (2.1)$$

Where, D is the weighted distance (likelihood) and c indicates a particular class. X gives the measurement vector of the candidate pixel and M_c represents the mean vector of the sample of class c. a_c is the percent probability that any candidate pixel is a member of class c (defaults to 1.0). Cov_c and $|Cov_c|$ are the covariance matrix of the pixels in the sample of class c and determinant of Cov_c respectively. Cov_c^{-1} is the inverse of Cov_c (matrix algebra) (Hord, 1982).
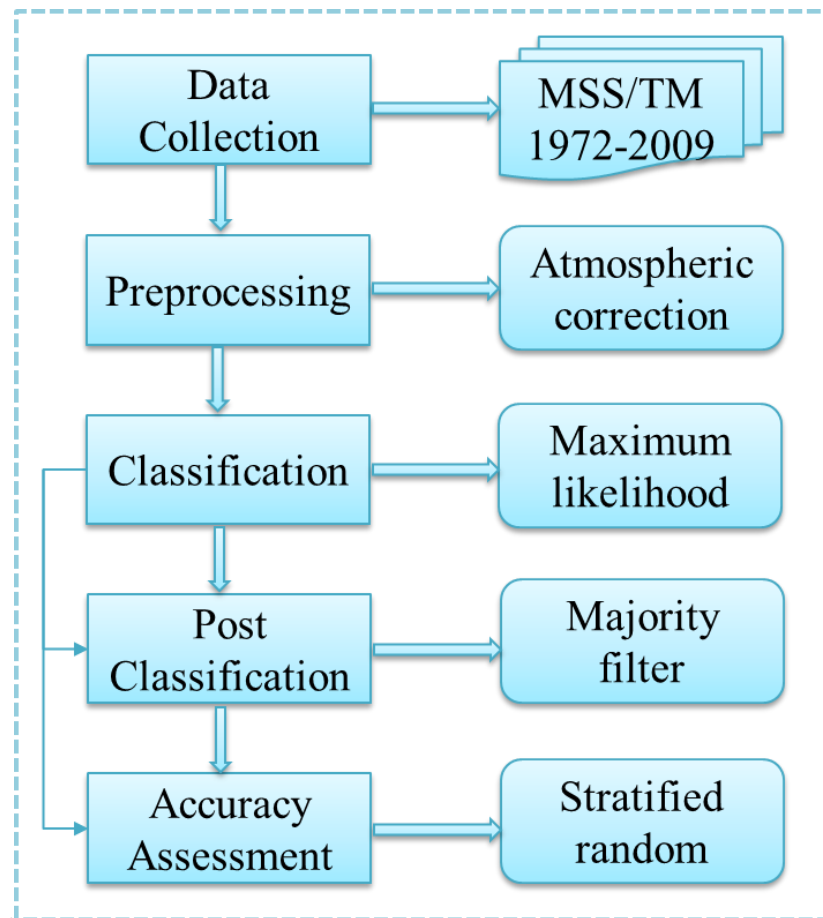
Figure 2.3 Land cover classification flowchart

2.3.2 Land Cover Change Mapping

In this chapter, the land cover change detection uses three Landsat images from the years 1972, 1990 and 2009. The three images were classified into four land cover types by the ML classification method. Besides, the pixels in the classification maps were filtered with the 2.5 hectares clumping size by the majority filter, therefore the distinct or "sandy" pixels can be effectively removed out. The change maps from 1974 to 1990 and from 1990 to 2009 were derived based on the three post-classified maps (Figure 2.4). Table 2-1 presents the change areas of the different types of land cover changes from 1972 to 1990 and 1990 to 2009. The largest change type from 1972 to 1990 and also from 1990 to 2009 is from forest to agriculture.

The major changes also include the changes from agriculture to artificial areas and the artificial to agriculture. However, the changes from artificial area to agriculture or forest area are probably caused by the bare soil which has quite similar spectral characteristics or from the classification errors. Actually, among all the land cover changes, even the largest change area of 16 km^2 is very small. Therefore, we conclude that the changes are too small to be considered respectively during the two periods.

Table 2-1 Land cover change areas from 1972 to 1990 and 1990 to 2009 respectively.

Change Type	1972-1990 (km^2)	1990-2009 (km^2)
Agriculture to Artificial	4.23	0.38
Forest to Artificial	1.14	0.00
Artificial to Agriculture	4.47	2.26
Forest to Agriculture	15.85	2.55
Agriculture to Forest	0.31	1.71
Artificial to Forest	0.17	0.00
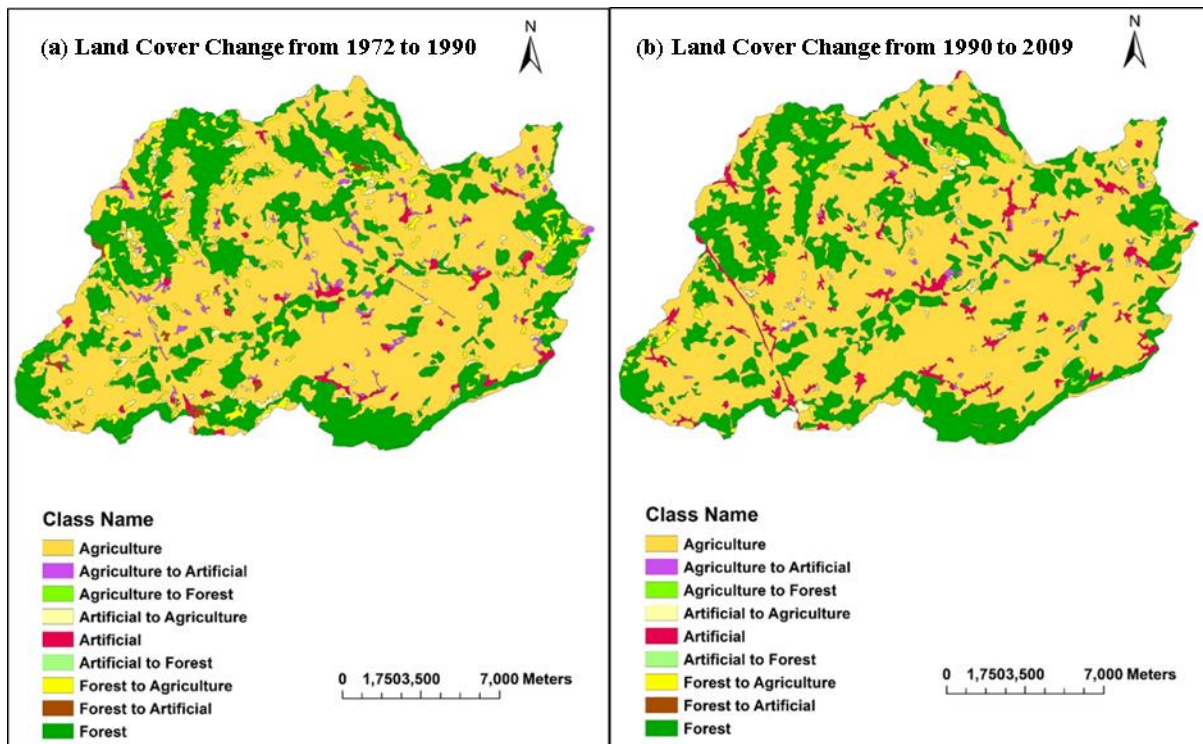
Figure 2.4 Land cover change maps from 1972 to 1990 and from 1990 to 2006 based on Landsat images of Level 1 category.

2.3.3   Change Comparison with CORINE Data

CORINE provides three-year land cover maps and two land cover change maps in two periods from 1990 to 2000 and from 2000 to 2006. CORINE land cover maps were generated by computer assisted visual interpretation based on the high resolution satellite images and the in-situ or ancillary data (EEA, 2012). One main difference between the CORINE products and our land cover or LUCC maps lies in the minimum mapping unit (MMU). The MMU of CORINE land cover map is 25 hectares and our land cover maps are derived with the MMU of 2.5 hectares. And as a separate product, land cover change maps from CORINE with the MMU of 2.5 hectares are produced directly by means of computer-aided visual image interpretation not based on the land cover maps in the different years. In this chapter the MMU of our land cover change maps is also 2.5 hectares. Figure 2.5(a) and (b) demonstrate more clearly land

cover changes of CORINE from 1990 to 2006 and of Landsat images from 1990 to 2009, respectively. It is obvious to see that the main change areas are consistent between CORINE and Landsat, but the Landsat provides more small-scale changes. The main change areas are located at the east forest and the north artificial area, which is a new mineral extraction site and also the middle part of newly developed artificial area. But all in all, no matter based on the CORINE or the Landsat images, it can be seen that the Attert Catchment shows very small changes during a 10-years period. This also serves as the primary background information for our further land cover investigation using thermal remote sensing in this area (see Chapter 3).
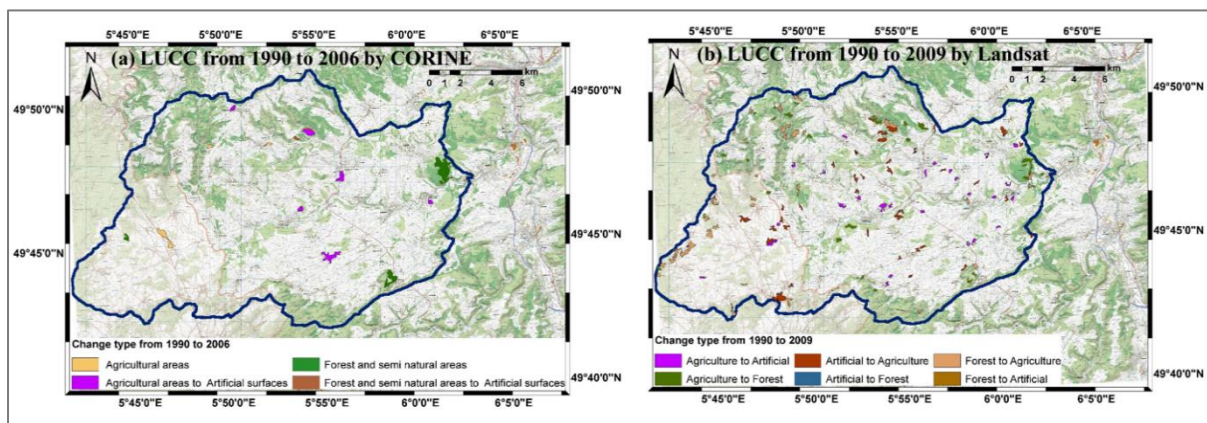
Figure 2.5 Land cover change maps of CORINE.

2.4   Comparison of Four Smoothing Methods for MODIS Data

Apart from the land cover change analysis of the Attert Catchment, the other focus of this chapter is the comparison of different smoothing methods for the MODIS datasets. As described in the introduction, the smoothing of MODIS VI products plays an important role in providing continuous and good-quality vegetation dynamic data. In this work, four smoothing methods were selected including the mBISE, AG function, DL function and the adaptive SG filter from the TIMESAT software. The main idea is to smooth the MODIS products using the four methods, to compare the smoothed data with the high-quality Landsat data, and then

finally to evaluate the performance of the four methods by the root mean square error (RMSE), mean absolute error (MAE), Person's correlation coefficient (CC) and the coefficient of determination (R^2).

2.4.1 MODIS Data Sources

In order to fully exploit the effectiveness of the different smoothing methods, diverse products from MODIS and Landsat were selected. Table 2-2 gives a brief description of the used satellite products. MOD09GQ provides the daily surface reflectance data of band 1-2 (red, NIR) at 250 m resolution. The MOD09GQ Level 2 spectral reflectance data has been atmospherically corrected and then directly used to calculate the daily NDVI data following Equation 2.2. All the 365 images of NDVI data in 2013 were estimated from the MOD09GQ products. Besides, the MOD13Q1 NDVI data are provided every 16 day at 250 m spatial resolution and designed to offer consistent spatial and temporal comparison of vegetation conditions (Didan, 2015). Moreover, the NDVI datasets calculated from the atmospherically corrected Landsat TM/ETM reflectance data were used as the reference data for error assessment. We collected all the cloud-free Landsat images since 1984 to 2011 of TM and 2000 to 2011 of ETM. In this work, the resampled cloud-free and corrected Landsat images are assumed to have higher quality and can be used as the average reference data for the MODIS NDVI datasets. Furthermore, MOD15A2 LAI product was utilized to evaluate the smoothing methods in this work. MOD15A2 data offers the composite level-4 MODIS global LAI product every 8 days at 1 km resolution and the accuracy of this version 5 dataset has been assessed over a widely distributed set of locations and time periods (DAAC, 2012).

Table 2-2 The characteristics of the used satellite data in this work.

Satellite Data	Product Type	Spatial Resolution	Temporal Resolution	Used time period in this work
MOD09GQ	Surface reflectance	250 m	daily	2013
MOD13Q1	NDVI	250 m	16-day composite	2013
MOD15A2	LAI	1 km	8-day composite	2013
Landsat TM/ETM	Atmospherically corrected reflectance data, NDVI	30 m	16 days revisit interval	TM: 1984-2011; ETM:2000-2011

2.4.2 Smoothing Methods

In the past decades, a large amount of noise filtering methods have been developed for the satellite data ranging from the early Maximum Value Composite (MVC) technique (Holben, 1986), to the Fourier analysis (Roerink et al., 2000) and function fitting (Jonsson and Eklundh, 2002). In this work, our objective is not to propose a new smoothing method but to find a suitable and robust method to filter the noise of the MODIS products in order to offer the reliable datasets for the further vegetation dynamics modelling. Therefore, four representative smoothing methods were utilized in this work and the following section gives a brief description of each method.

The BISE method was proposed based on the predictability of vegetation change which is distinct from the high frequency changes (Viovy et al., 1992). The general idea of BISE is that the sudden rises or falls in NDVI are a feature of changing cloud conditions or viewing angles but are not compatible with the gradual process of plant growth. The BISE algorithm is

originally designed for the daily NDVI data and assumes that cloud and poor atmospheric conditions will usually depress the NDVI values. Besides that, the NDVI data will increase with abnormally high values due to the data transmission errors. Meanwhile, the method assumes that the decreases in NDVI relating to changes (possibly sudden decrease) in vegetation status will persist for several days. The algorithm searches forward and accepts the following point if it has a higher value than the first. If the NDVI value decreases and there is no point greater than 20 percent of the difference between the first low value and the previous high value during a pre-defined period (also called sliding period), then the decrease can be accepted. Otherwise, the low point will be ignored. However, BISE may perform poorly when there is a long-term, gradual decrease in NDVI. Therefore, by developing the BISE from daily NDVI data to the 10-day composite products, the mBISE algorithm is adjusted to look for the spikes of time series of VI data by taking the local gradient of the data within the sliding window into account (Lovell and Graetz, 2001). The main advantage of the BISE or mBISE is that it will not reduce the potentially valuable data during the sliding period and it can effectively alleviate the cloud and viewing conditions influences. In this work, BISE was performed for the daily MOD09GQ NDVI data and mBISE was applied for the MOD13Q1 NDIV and MOD15A2 LAI products.

Besides the BISE/mBISE method, the other three smoothing methods embedded in the TIMESAT software were utilized. TIMESAT is a FORTRAN90 based program and can be used to smooth the time series of NDVI data and to extract the seasonality parameters by three methods including the AG function, DL function and the adaptive SG filter method. In TIMESAT, the time series of NDVI data can be assigned with different weights for quality control. Here, to solely evaluate the performance of the smoothing methods, we leave all the weights the same as 1. The adaptive SG filter uses the local polynomial function for the fitting process, and the AG and DL are fitted with the least-squares methods.

The basic Gaussian function is formulated as described in Equation 2.2.

$$g(t; x_1, x_2, \ldots, x_5) = \begin{cases} exp\left[-\left(\frac{t-x_1}{x_2}\right)^{x_3}\right] & if\ t > x_1 \\ exp\left[-\left(\frac{x_1-t}{x_4}\right)^{x_5}\right] & if\ t < x_1 \end{cases} \qquad (2.2)$$

where, in the Gaussian function, x_1 determines the position of the maximum or minimum with respect to the time variable t. x_2, x_3, x_4, x_5 determine the width and flatness of the right and left half function respectively.

The DL function in TIMESAT uses the function in Equation 2.3. The parameters were used to restrict the NDVI shape to be physically reasonable for the plant growth. In the function, x_1 and x_2 represent the inflection position and rate of change during the leaf-on stage, while x_3 and x_4 indicate the inflection position and rate of change during the leaf-off stage respectively.

$$g(t; x_1, \ldots, x_4) = \frac{1}{1+exp\left(\frac{x_1-t}{x_2}\right)} - \frac{1}{1+exp\left(\frac{x_3-t}{x_4}\right)} \qquad (2.3)$$

The SG filter is proposed to detect the large increase or decrease in an interval with locally adapted window iteratively. The basic idea is to replace the disturbed data with the value by a polynomial (Press et al., 1996) . Therefore, for each data y_i, $i = 1, 2, \ldots, N$, a quadratic polynomial as Equation 2.4 will be fitted to all $2n+1$ points in the moving window n and y_i will be replaced with the polynomial value at position t_i.

$$f(t) = c_1 + c_2 t + c_3 t^2 \qquad (2.4)$$

2.4.3 Smoothing Results and Uncertainties Evaluation

In this work, we selected 12 representative sites of beech forests in Attert Catchment for the performance evaluation. The forest sites distribute all over the catchment with different geological characteristics. The locations of the sites are labelled with numbers in Figure 2.6. For the 250 m pixels in MOD09GQ and MOD13Q1, the number of selected pixels is 12 while for the 1 km resolution MOD15A2 the pixels are aggregated and the number becomes five.
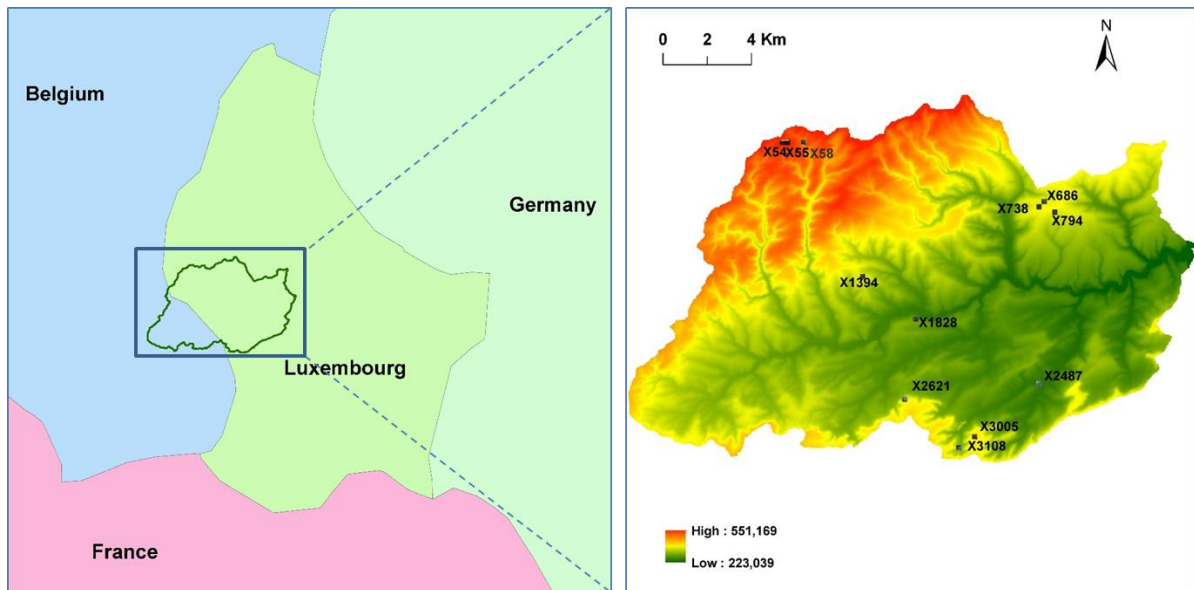
Figure 2.6 Location of the representative beech forest sites in the Attert Catchment.

The filtering results for the daily NDVI data calculated from the MOD09GQ products (Figure 2.7) demonstrate that the original NDVI data contain large amount of noises. From the distribution of the daily MOD09 NDVI data, it seems that the true features of the beech forest have been almost disguised by the noises (Figure 2.7). Solely depending on the appearance of the smoothing results, the BISE and SG methods provide very fluctuant NDVI data compared to the AG and DL functions. While for the 16-day composite MOD13Q1products (Figure 2.8), the methods produced more consistent and smoothed NDVI data. Besides that, the noises of the LAI data from MOD15A2 products were also nicely filtered (Figure 2.9). Due to the resolution differences between MOD15A2 LAI with the MODIS NDVI products, the LAI values of the 1 km pixel corresponding to the aggregation of several 250 m pixels may be affected by the mixture of different land cover types. From the MOD13Q1 NDVI profiles in Figure 2.8, it is clear to see that the pixels labelled as the beech forest in the CORINE land cover map have relatively similar and high NDVI values. Whereas, the 1 km MOD15A2 LAI values of different pixels vary differently during the year. Solely depending on the visual interpretation, the results indicate that the performances of the BISE and SG methods tend to

be very sensitive to the abrupt changes of the annual cycle. While in the other hand, the AG and DL provided relatively continuous and stable results because of the inherit characteristics of these two functions.
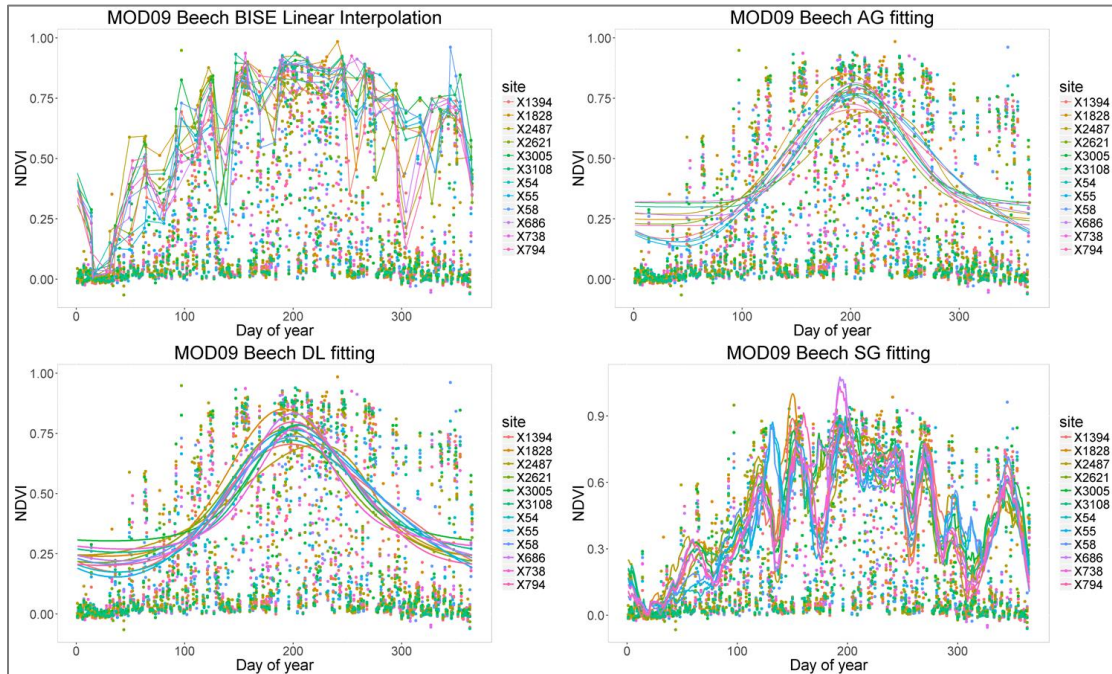
Figure 2.7 The 12 pixels smoothing results of MOD09GQ NDVI data in 2013 by the four smoothing methods: linearly interpolated BISE method, AG, DL and SG functions.
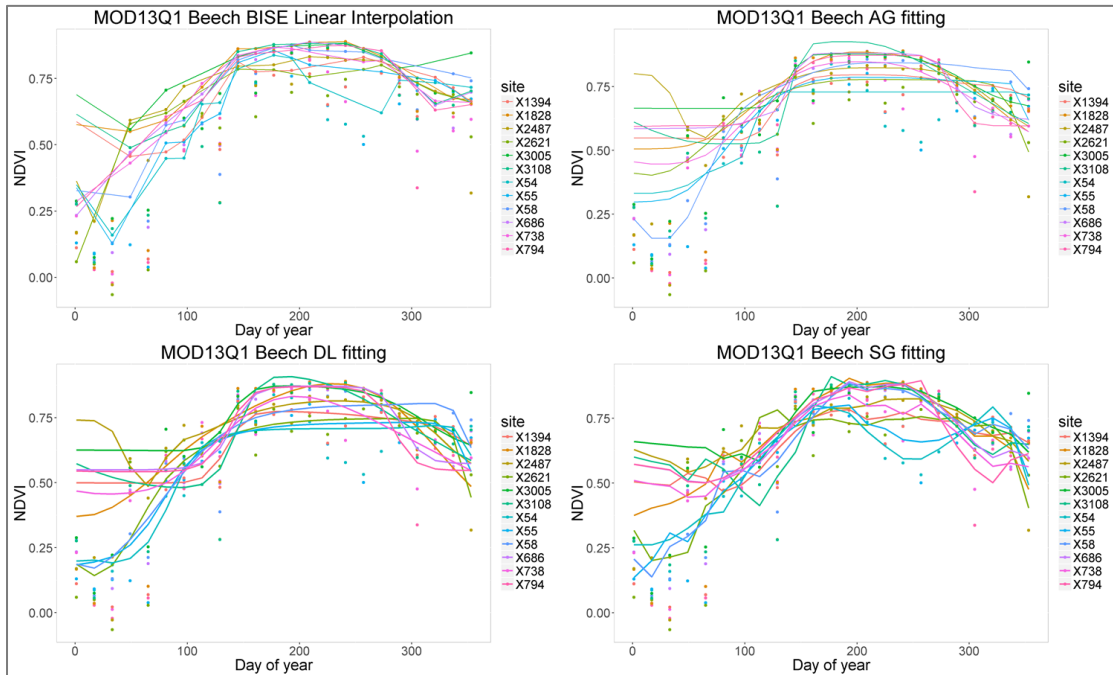
Figure 2.8 The 12 pixels smoothing results of MOD13Q1 NDVI data in 2013 by the four smoothing methods: linearly interpolated BISE method, AG, DL and SG functions.
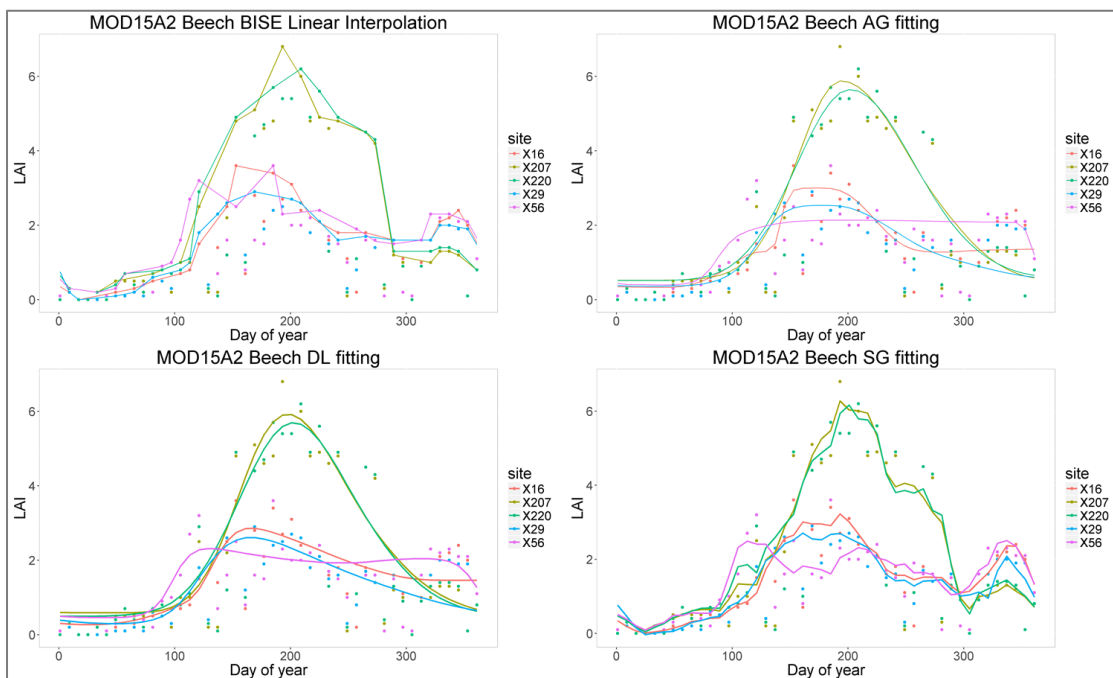
Figure 2.9 The five pixels smoothing results of MOD15A2 LAI data in 2013 by the four smoothing methods: linearly interpolated BISE method, AG, DL and SG functions.

2.4.4 Uncertainties Evaluation

Concerning the briefness of the uncertainties evaluation, in this work we only assess the performance of the four smoothing methods for the NDVI products. As mentioned above, we estimated the NDVI data from the 25 atmospherically corrected Landsat images from 1984 to 2011 to serve as the reference data for the smoothed NDVI data. Table 2-3 lists all the dates and sensor information of the 25 cloud-free Landsat images. Before directly comparing the Landsat NDVI data with MODIS NDVI data, two steps should be done. Firstly, the Landsat images were resampled from 30 m to 250 m resolution in order to be consistent with the MODIS NDVI products. The resampled 250m reference NDVI values were calculated by averaging the 30m NDVI values of the corresponding pixels from each Landsat image. Secondly, all the resampled Landsat images were ordered according to the Julian day of year (DOY) data. To be consistent with the maximum value composite method used in the MODIS NDVI data produced for each 16-day interval counting from the first day of each year (e.g. 001, 017,…, 353), the maximum values of the Landsat images falling into the 16-day interval were kept for comparison. Therefore, in the end, 12 beech sites with resampled 250m Landsat NDVI data on 15 different dates were utilized for evaluating the MODIS NDVI products. Figure 2.10 displays the comparison between Landsat NDVI with the original MOD09GQ and MOD13Q1 NDVI data. It is clear to see that the MOD09GQ NDVI data contain large noises and have nearly no correlation with the Landsat NDVI data. MOD13Q1 NDVI data have MOD09GQ NDVI data.

Table 2-3 The cloud-free Landsat TM/ETM images collected as the reference datasets for MODIS.

Date	Year	Day of Year	Sensor	Date	Year	Day of Year	Sensor
2011-03-02	2011	61	ETM	**2006-07-02**	2006	183	TM
2004-03-30	2004	90	ETM	**1990-07-14**	1990	195	TM
2001-04-11	2001	101	TM	**2006-07-18**	2006	199	TM

1988-04-11	1988	102	TM	**2003-08-03**	2003	215	ETM
2011-04-19	2011	109	ETM	**1985-08-09**	1985	221	TM
2011-05-05	2011	125	ETM	**2003-08-11**	2003	223	TM
1988-05-13	1988	134	TM	**1984-08-22**	1984	235	TM
1989-05-16	1989	136	TM	**2011-09-02**	2011	245	TM
2004-05-17	2004	138	ETM	**2004-09-06**	2004	250	ETM
2010-06-03	2010	154	ETM	**2003-09-20**	2003	263	ETM
2009-06-24	2009	175	TM	**1987-10-02**	1987	275	TM
2001-06-26	2001	177	ETM	**2003-11-07**	2003	311	ETM
2010-06-27	2010	178	TM	**In Total**	25	61-311	Landsat
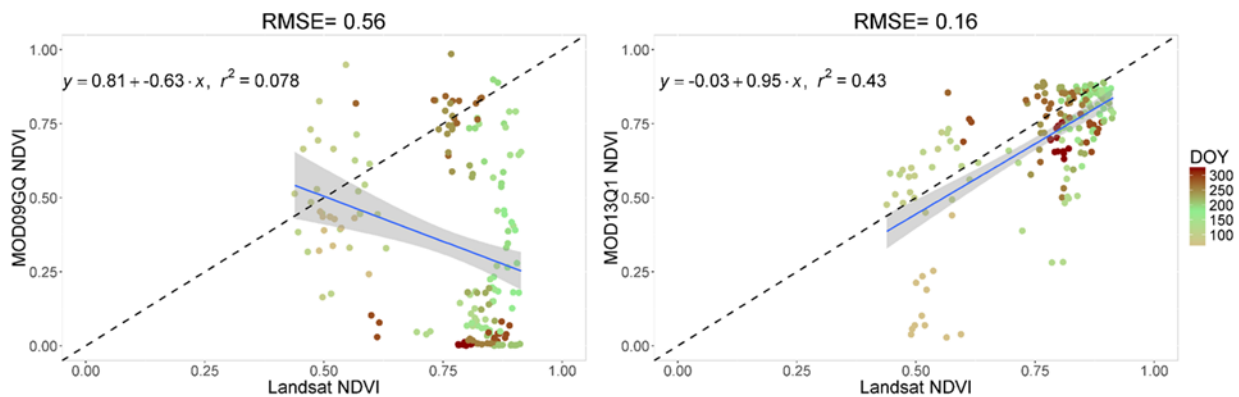
Figure 2.10 Comparison between Landsat NDVI with MOD09GQ and MOD13Q1NDVI data.

For the uncertainty evaluation, the filtered NDVI data using the four smoothing methods were compared with the Landsat NDVI data in 2013. The scatterplots in Figure 2.11 and Figure 2.12 reveal the relationship between the Landsat NDVI and the smoothed data from MOD09GQ and MOD13Q1 respectively. Moreover, Table 2-4 presents the statistical data calculated between the Landsat NDVI and the data from MOD09GQ or MOD13Q1 NDVI data. CC, RMSE and MAE were calculated for each dataset. Compared to the original MOD09GQ NDVI data, the smoothed data show significantly improved characteristics. The DL method retrieves the highest CC data for MOD09GQ data whereas the BISE method obtains the CC of 0.54 with

the lowest RMSE and MAE data of 0.15 and 0.11 respectively, which is about 0.15 lower than SG. In respect to the MOD13Q1NDVI products, mBISE method provides the best statistical data regardless of the CC, RMSE, MAE or the R^2. The CC between the mBISE smoothed NDVI and Landsat NDVI is 0.76 and the mean RMSE and MAE are 0.09 and 0.07 respectively. Actually, the smoothing results of the MOD09GQ vary greatly by using the different methods, whereas the differences between the smoothed MOD13Q1 results are relatively small. For example, SG method provides the lowest CC data for the noisy MOD09GQ data but retrieves similar results as the DL method for the composite MOD13Q1 NDVI data. In summary, from the overall comparison of both MOD09GQ and MOD13Q1 NDVI data, the mBISE method derives the acceptable NDVI data with good quality, which could be very useful for filtering the noises of the satellite products before application into the vegetation dynamics modelling. However, although the mBISE method obtained the best CC of 0.76, there are still large discrepancies between the smoothed MOD13Q1 and resampled Landsat NDVI data. This problem may be caused by the resampling procedure when we averaged the Landsat NDVI data, which possibly could be improved by more appropriate reference NDVI data.

Table 2-4 The statistics estimated between the MOD09GQ and MOD13Q1 NDVI data and the Landsat NDVI data

	MOD09GQ	BISE	AG	DL	SG
CC	-0.28	0.54	0.68	**0.70**	0.44
RMSE	0.56	**0.15**	0.28	0.28	0.30
MAE	0.46	**0.11**	0.24	0.25	0.25
	MOD13Q1	mBISE	AG	DL	SG
CC	0.65	**0.76**	0.74	0.72	0.72
RMSE	0.16	**0.09**	0.09	0.10	0.11
MAE	0.11	**0.07**	0.07	0.08	0.09
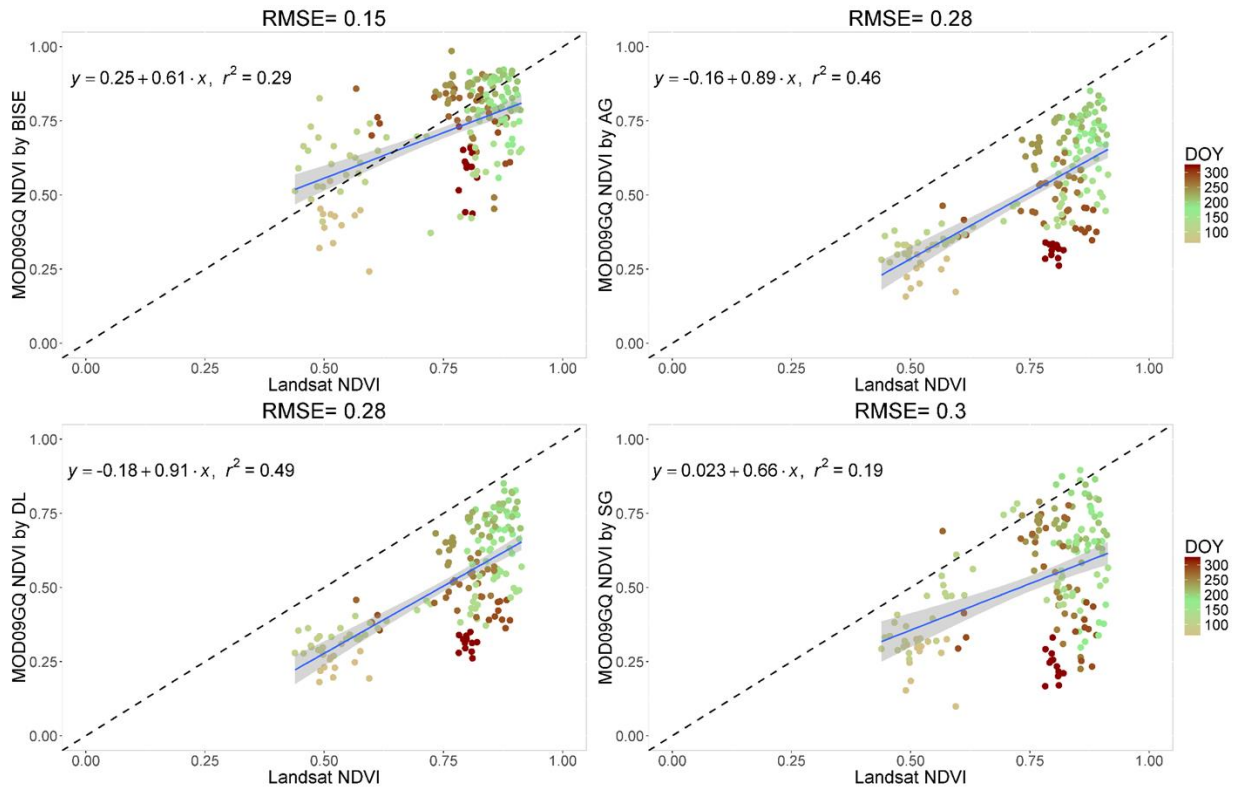
Figure 2.11 The comparison between Landsat NDVI and the smoothed NDVI datasets of MOD09GQ by BISE, AG, DL, and SG respectively.
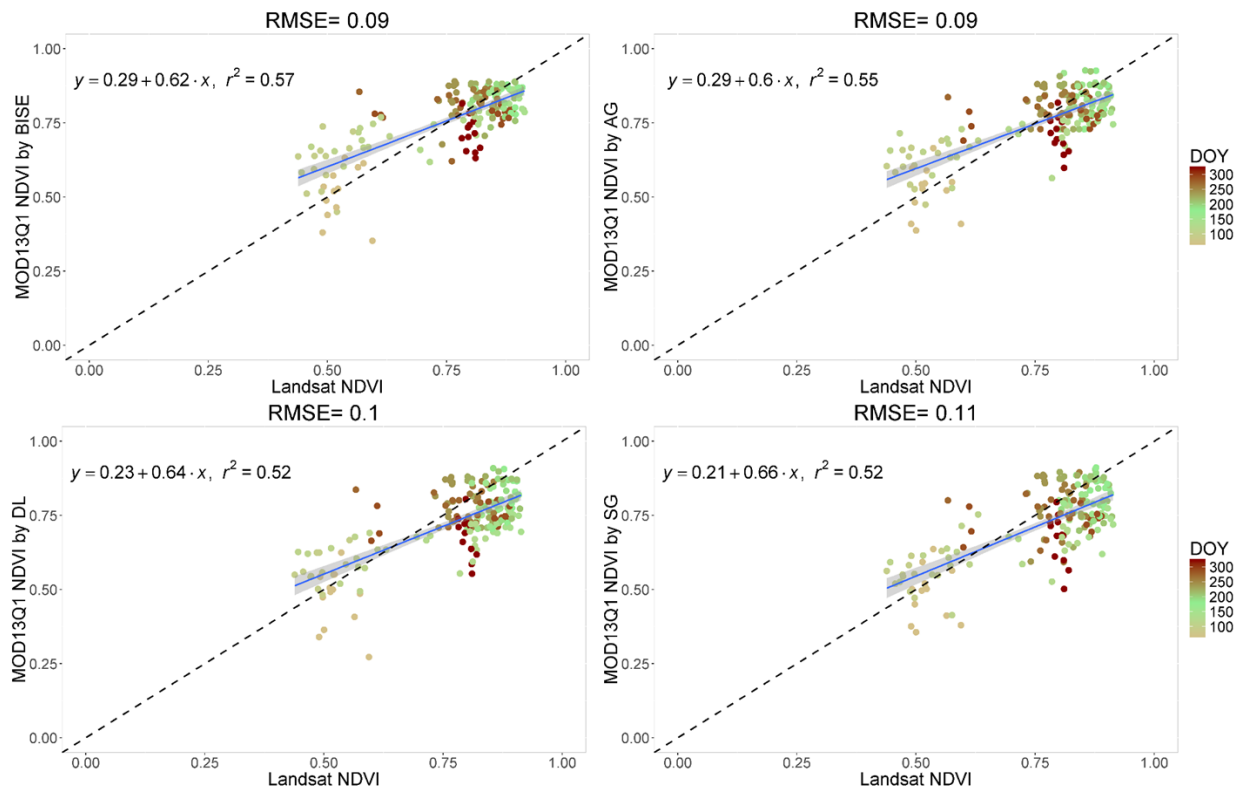
Figure 2.12 The comparison between Landsat NDVI and the smoothed NDVI datasets of MOD13Q1 by BISE, AG, DL, and SG respectively.

2.5   Conclusion and Summary

In this chapter, the Landsat images for land cover classification and MODIS products for the vegetation dynamics modelling were preprocessed. The preprocessing of Landsat images took the data in 1972, 1990 and 2009 as an example and the atmospheric correction were performed for each image. Then, in order to assess the land cover changes of Attert Catchment during the past 40 years, the Landsat images were classified into four land cover types and post-processed for the land cover change detection. The results reveal that the largest land cover type changes between 1972 and 2009 are the changes from forest to agriculture. Moreover, the change areas are very small in the separate periods from 1972 to 1990 and from 1990 to 2009. The relatively

constant conditions in Attert Catchment serve as the valuable prior knowledge for the further investigation.

Besides that, the preprocessing of the MODIS products demonstrates the superiority of BISE/mBISE method in filtering the noises of satellite data. Compared to AG, DL and SG methods, BISE/mBISE method retrieves the smoothed vegetation status data in terms of NDVI with higher CC and lower RMSE and MAE data evaluated by the Landsat NDVI data. Due to lack of the field measured NDVI data and resampling uncertainties of the Landsat NDVI data, there are still discrepancies between the resampled Landsat and the MODIS NDVI data. This work mainly provided an overview of the performances of different smoothing methods. In particular, the mBISE method performs best for the 16-day composite MOD13Q1 NDVI data with the advantage of keeping the original good-quality data while omit the anomalous values affected by the atmospheric conditions or system errors. Nevertheless, the future work probably could be greatly improved when using more suitable resampling method for the Landsat images. Moreover, in the following study of vegetation dynamics modelling, the preprocessing by the mBISE method could be helpful in deriving more accurate reference data from the satellite products.

3 The Improvement of Land Cover Classification by Thermal Remote Sensing

This chapter has been published as Sun, L., and K. Schulz, 2015, The Improvement of Land Cover Classification by Thermal Remote Sensing: Remote Sensing, v. 7, p. 8368.

3.1 Abstract

Land cover classification has been widely investigated in remote sensing for agricultural, ecological and hydrological applications. Landsat images with multispectral bands are commonly used to study the numerous classification methods in order to improve the classification accuracy. Thermal remote sensing provides valuable information to investigate the effectiveness of the thermal bands in extracting land cover patterns. *k*-NN and Random Forest algorithms were applied to both the single Landsat 8 image and the time series Landsat 4/5 images for the Attert catchment in the Grand Duchy of Luxembourg, trained and validated by the ground-truth reference data considering the three level classification scheme from COoRdination of INformation on the Environment (CORINE) using the 10-fold cross validation method. The accuracy assessment showed that compared to the visible and near infrared (VIS/NIR) bands, the time series of thermal images alone can produce comparatively reliable land cover maps with the best overall accuracy of 98.7% to 99.1% for Level 1 classification and 93.9% to 96.3% for the Level 2 classification. In addition, the combination with the thermal band improves the overall accuracy by 5% and 6% for the single Landsat 8 image in Level 2 and Level 3 category and provides the best classified results with all seven bands for the time series of Landsat TM images.

3.2 Introduction

Land cover is defined as the observed biophysical state of the earth's surface, and is largely described by the presence or absence of various vegetation types(Anderson, 2005). In contrast, land use normally refers to the arrangements, activities and inputs people engage in a certain land cover type to produce, change or maintain it (Liang, 2008). As previous studies reported, land cover information is a fundamental variable for many hydrological and climate studies. Land cover characteristics have close links to the human and physical environments, also govern and affect many environmental variables (Bounoua et al., 2002), including surface roughness, albedo, moisture availability, mechanisms for runoff generation (Dickinson, 1995), and water quality (Nilsson et al., 2003). Therefore, accurate land-cover mapping becomes essential for modeling and understanding these biogeophysical properties of the land surfaces.

Remote sensing provides an effective way to depict land cover as it produces a map-like representation of the Earth's surface that is spatially continuous and highly consistent, as well as available at a range of spatial and temporal scales (Anderson, 2005). The Landsat satellites have monitored Earth's terrestrial surfaces for about 40 years (Sexton et al., 2013), from which the long, consistent and free record allows scientists to study the current and also the past land surface patterns. Because of that, Landsat data are widely applied in land cover classification and monitoring on a regional or global scale. Numerous studies have proved the usefulness of Landsat imagery in agricultural land cover classification (Samaniego and Schulz, 2009), forest dynamics monitoring (Salovaara et al., 2005), urban land use classification (Lu and Weng, 2006), other land cover dynamics or land use land cover (LULC) change detection (Gong et al., 2012; Sexton et al., 2013; Sobrino and Raissouni, 2000). Other satellite products such as the Advanced Spaceborne Thermal Emission and Reflection Radiometer (ASTER) sensor imagery have also been widely used for regional scale land cover classification (Crocetto and Tarantino, 2009; Jianwen and Bagan, 2005; Zhu and Blumberg, 2002) or land cover change detection(French et al., 2008; Marçal et al., 2005).

In most cases, the LULC classification is based on the multispectral characteristics and/or the multi-temporal biological properties of the Earth surface. In previous studies, numerous efforts have been made to improve the classification accuracy by constructing different spectral features, developing new methods, or integrating multi-source data for the single or time series of images. Lunetta and Balogh (LUNETTA et al., 1999) for example evaluated the identification of wetlands with the bands 2 to 5 of the single-date and multi-temporal Landsat 5 images. The overall accuracy (OA) was 69% of the single-date image compared to 88% from the two-date images with a significant increase in the Kappa test statistics. Murai and Omatu (Murai and Omatu, 1997) proposed a pattern classification method which integrates the advantages of both the neural network and knowledge-based system. The single Landsat 5 TM image with the bands 3 to 5 was used and they found that the misclassification can be revised more easily because of introducing the geographical knowledge into the system. Maxwell et al. (Maxwell et al., 2004) introduced an automated approach to classify four land cover types using only the bands 2 and 4 from Landsat MSS with 92.2% OA.

Langley et al. (Langley et al., 2001) compared the single-date imagery and multi-temporal images for land cover classification with the bands 3 to 5 of TM image. They concluded that the multi-temporal images have improved the accuracies of some landscapes but the single-date image may provide a reliable vegetation cover map in semi-arid environments. Saadat et al. (Saadat et al., 2011) utilized two single-date Landsat ETM+ image without the thermal bands for LULC classification in Iran with OA of 95% and 82% respectively for the late summer image and the spring image. He recommended that when the satellite image is limited the late summer image would be most suitable for the LULC classification. Guerschman et al. (Guerschman et al., 2003) also suggested that, if possible, three images (spring, early summer, late summer) be used in the identification of agricultural types. Yuan et al. (Yuan et al., 2005) used multi-temporal TM images from 1986 to 2002 to monitor the LULC dynamic with the average OA of 94% and proved the potential of multi-temporal Landsat data for accurate and

economic land cover change analysis. Besides the different band combinations, the normalized difference vegetation index is also commonly used for the LULC change detection with the multi-temporal images (Brown et al., 2013; Carrão et al., 2008; Ozdogan and Gutman, 2008; Sexton et al., 2013; Wilson and Sader, 2002). For both single-date image and multi-temporal images, several studies focus on the algorithm development such as nearest neighbor (NN) (Collins et al., 2004) and modified NN (Samaniego et al., 2008; Samaniego and Schulz, 2009), random forest classifier (Corcoran et al., 2013; Deng and Wu, 2013; Gislason et al., 2006), rule-based classification (Lucas et al., 2007; Rodriguez-Galiano et al., 2012a), which all provide accurate land cover classification maps.

However surprisingly, the thermal information provided by many of the satellite platforms has rarely been used for land cover classification (Southworth, 2004). Thermal remote sensing allows for the continuous representation of land surface temperature (Li et al., 2013), which is widely used for the monitoring of urban climate (Liu and Zhang, 2011), the modeling of the hydrological cycle (Su, 2002), vegetation monitoring (Kogan, 2001) and mapping land surface energy and water vapor fluxes (Kustas and Anderson, 2009). Although the spatial resolution of the thermal band is coarser when compared to the visible bands of the same satellite, the thermal information may contain valuable information related to the spatial variations of land surface and therefore vegetation properties (Defries et al., 2000; Foody, 1996), which has so far not been explored to its full extent.

The objective of this study therefore is to investigate the value and effectiveness of the thermal remote sensing data for improving land cover classification. The test region is the Attert catchment in Luxemburg/Belgium providing a landscape with a variety of land cover types, mainly including forest, agriculture land, pasture and residential area. Based on the land cover change maps from 1990 to 2006 provided by CORINE and the change maps from 1972 to 1990 and 2006 to 2011 from CAOS project (not present in this paper), the land cover changes in quite small extent in 5 to 8 years especially in the early 1990s. In this study, the variation among

different land covers is ignored and the land cover types of Level 1 and Level 2 are assumed to be constant during the periods from 1984 to 1990 and 2006 to 2011. Two of the most often and successfully applied standard methods, the k-NN(Cover and Hart, 1967), as well as the Random Forest method (Breiman, 2001), will be applied to Landsat 4/5 and Landsat 8 images. Three groups of the single-date Landsat 8 images with different visible and thermal bands combination will be classified into three levels of land use land cover categories in order to evaluate the effectiveness of the thermal band in single image classification. The combination of band 3 and band 4, principal components, 6 bands combination without thermal band, the thermal band and 7 bands combination including thermal band from time series Landsat 4/5 images listed in two groups will be classified into two levels for comparison and performance analysis. 10-fold cross validation will be applied for the accuracy assessment with the overall accuracy.

3.3   Data Source

3.3.1 Satellite Data

The Landsat Thematic Mapper (TM) sensor was carried onboard of Landsat 4 and 5 from July 1982 to May 2012 with a 16-day repeat cycle, and began decommissioning in January 2013. TM images consist of seven spectral bands (Table 3-1) with a spatial resolution of 30m for Bands 1 to 5 and 7. The spatial resolution for Band 6 (thermal infrared) is 120m, but is resampled to 30m pixels in the provided L1T products after February 25, 2010. A total of 13 cloud-free TM images between 1982 and 2012 were collected for the Attert catchment (path 197, row 25). The newly launched (on February 11, 2013) Landsat 8 Operational Land Imager (OLI) and Thermal Infrared Sensor (TIRS) provide nine spectral bands and two thermal bands as listed in Table 3-1. All spectral bands are collected at 30m, except for the thermal bands that are acquired at 100m resolution and resampled to 30m in the delivered product and the panchromatic band 8 providing 15m data. One cloud-free Landsat 8 image was acquired for

July 21, 2013 (at the same time the ground-truth field campaign was conducted). The Landsat images available for this study have been divided into three groups (Table 3-2). Group 1 (TS1) and Group 2 each contain time series of images covering spring, summer and autumn (TS1 covers the Landsat 4/5 images from 1984 to 1990 and TS2 includes the Landsat 5 images from 2003 to 2011). Both groups were used to investigate the land cover classification performance when based on time series of images. The third group (S1) with only one Landsat 8 image from July 21, 2013 was tested to explore the effectiveness of single image land cover classification based on thermal data.

Table 3-1 Spectral Characteristics of the 7 bands from Landsat 4/5 TM image and the 11 bands from Landsat 8 image.

Bands	Landsat 4/5 Wavelength (micrometers)	Landsat 8 Wavelength (micrometers)
Band 1	0.45-0.52	0.43 - 0.45 (Coastal aerosol)
Band 2	0.52-0.60	0.45 - 0.51 (Blue)
Band 3	0.63-0.69	0.53 - 0.59 (Green)
Band 4	0.76-0.90	0.64 - 0.67 (Red)
Band 5	1.55-1.75	0.85 - 0.88 (Near Infrared (NIR))
Band 6	10.40-12.50	1.57 - 1.65 (SWIR 1)
Band 7	2.08-2.35	2.11 - 2.29 (SWIR 2)
Band 8		0.50 - 0.68 (Panchromatic)
Band 9		1.36 - 1.38 (Cirrus)
Band 10		10.60 - 11.19 (Thermal Infrared (TIRS) 1)
Band 11		11.50 - 12.51 (Thermal Infrared (TIRS) 2)

Table 3-2 All Landsat images used for the land cover classification including two groups (TS1 and TS2) of time series of Landsat 4/5 images from 1984 to 2011 and the single-date Landsat 8 image (S1) in July, 2013.

Group	Date	Day of Year	Sensor	Season
TS1	1984-08-22	235	Landsat 5	Summer
	1985-08-09	221	Landsat 5	Summer
	1987-10-02	275	Landsat 5	Fall
	1988-04-11	102	Landsat 5	Spring
	1988-05-13	134	Landsat 5	Spring
	1989-05-16	136	Landsat 5	Spring
	1990-07-14	195	Landsat 4	Summer
TS2	2003-08-11	223	Landsat 5	Summer
	2006-07-02	183	Landsat 5	Summer
	2006-07-18	199	Landsat 5	Summer
	2009-06-24	175	Landsat 5	Spring
	2011-04-11	101	Landsat 5	Spring
	2011-09-02	245	Landsat 5	Fall
S1	2013-07-21	202	Landsat 8	Summer

3.4   Land Cover Classification Scheme and Reference Data

In this study, the three-level land cover classification system of CORINE established by European Union (EEA, 2012) was utilized to represent the major land cover types (Table 3-3). Due to the lack of in situ ground truth data of the agricultural area and crop variations in the

same area for the images in the different years, only the Level 1 (4 land cover classes) and Level 2 (7 land cover classes) were considered for the time series classification of Landsat images. While for the single image classification in 2013, combined with the ground truth data all the three levels were classified and tested for the study area.

Table 3-3 Land use and land cover categories for the three-level classification scheme including the 4 classes of Level 1,7 classes of Level 2, 14 classes of Level 3 and the brief description of the Level 3 classes.

Level 1	Level 2	Level 3	Description of Level 3
Agricultural land	Bare soil	Bare soil	Fallow agricultural land or harvested land
	Cropland	Barley	Arable land for different crops, including the non-irrigated arable and permanently irrigated land, heterogeneous agricultural areas
		Corn	
		Wheat	
		Triticale	
		Rapeseeds	
		Oat and other crops	
	Grassland	Intensive grassland	Dense grass cover, includes areas with hedges
		Extensive grassland	Sparse grass cover, includes areas with hedges
Artificial land	Artificial land	Artificial land	Urban fabric, industrial, commercial and transport units, mine, dump and construction sites, artificial non-agricultural vegetated areas
Forest	Deciduous forest	Deciduous forest	Broad-leaved forest species, predominated by beech, oak, including shrub and bush understories
	Coniferous forest	Coniferous forest	Coniferous forest species, predominated by pine, larch, including shrub and bush understories
	Mixed forest	Mixed forest	Mixed broad-leaved and coniferous forest, neither species predominate, including shrub and bush understories
Water bodies	Water bodies	Water bodies	Water courses and water bodies
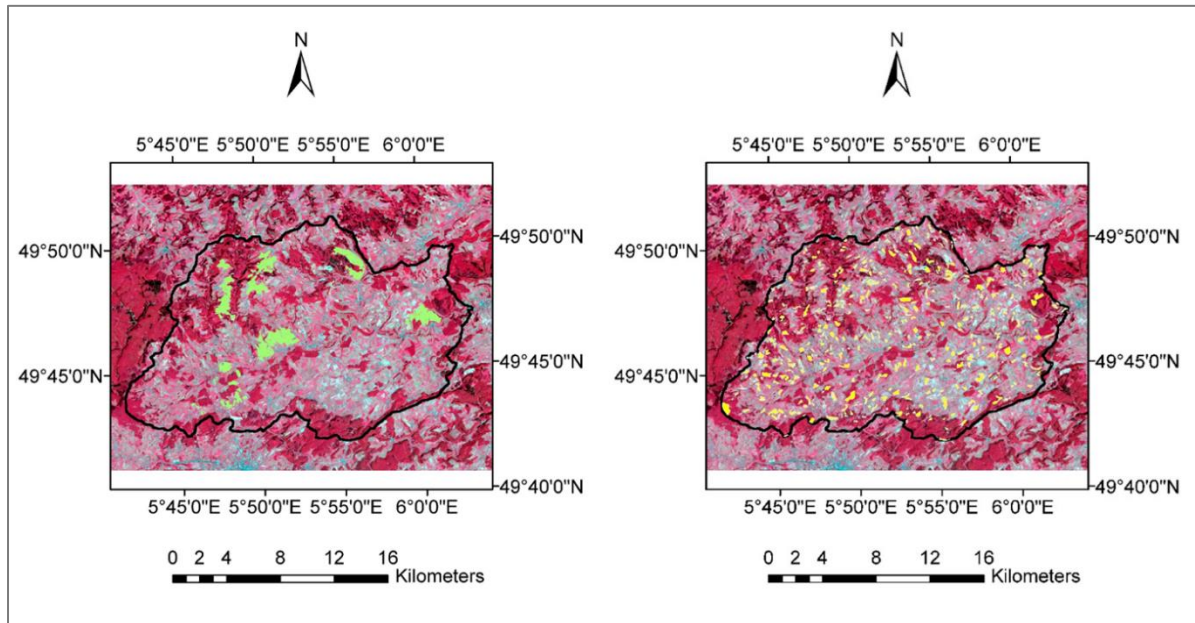
Figure 3.1The agricultural ground truth area labelled in green during the field campaign in July, 2013 (left) and all the training and validating pixels in yellow for the 7 classes of the Level 2 category based on the historical land cover maps of 2007(right); the background image of Attert Catchment (outlined in black) is the composite Landsat 8 image of July, 2013 in RGB combination of band 4, band 3 and band 2.

Training and validating samples were collected from the ground truth data and the reference maps (Figure 3.1). Firstly, the available historical land cover maps were collected including the finer land cover maps in 2007 provided by the collaborators in the CAOS project, CORINE land cover datasets of 1990, 2000 and 2006. Based on these reference maps and visual interpretation, areas of interest were created for the Level 1 and Level 2 category (the right image in Figure 3.1). Secondly, the various agricultural lands (550 sites) in Level 3 were labelled through the fieldwork campaign conducted in the Attert catchment from July 8 to July 13, 2013 (the left image in Figure 3.1). For the single Landsat 8 image, samples for all the three categories were used, whereas due to the impossibility of gaining historical ground truth data, only samples for the Level 1 and Level 2 categories were taken into account. The sample screening was performed for each land cover type in the ERDAS software and only the pure

pixels of the relatively larger site were kept. The principle is to obtain the evenly distributed samples over the catchment and to keep the size as similar as possible for both the single-date Landsat 8 image and the two time series of images.

The training set size has a great impact on the classification accuracy and appropriate training samples are prerequisites for a successful classification (Foody et al., 2006; Mather and Koch, 2010). Following the recommendations of Foody [32], van Genderen [45] and Congalton [46], the size of the training set should not be fewer than 10-30 observations per spectral band and per class. In this paper, the size of the samples for Level 1 and Level 2 category was set greater than 300 pixels. However only 40 pixels for the water bodies were selected in this catchment because the river courses are normally too small to be distinguished in the Landsat image.

3.5   Classification Schemes

3.5.1 Preprocessing

As reported by Song et al. (Song et al., 2001), atmospheric correction of images might not be necessary in case only a single image is used for the classification procedure. However, when multi-temporal or multi-sensor data are used, atmospheric correction is mandatory (Lu and Weng, 2007). Existing studies have tested the importance of different procedures for obtaining the stable and accurate images(Vicente-Serrano et al., 2008). 13 images used for the land cover classification were corrected by the MODTRAN 4 algorithm (Berk et al., 1998) embedded in the ATCOR3 module (Geosystems, 2013) in ERDAS software (Geosystem, 2013) to remove atmospheric and topographic effects within the resampled 30m ASTER GDEM product of METI and NASA (DAAC, 2009). All the corrected images were normally rescaled to the 8-bit raster images by the scale factor4 for both the reflectance and temperature data, i.e. a digital number value of 20 from the temperature image corresponds to a ground temperature of 5 ℃.

For the evaluation of the land cover classification based on the single Landsat 8 image (from July 21, 2013), three variants of spectral band combinations were considered: i) only the bands 2-5 from Landsat 8 (Bands4); ii) bands 2-5 plus the 2 thermal bands 10 & 11 (Bands6T); and iii) all bands except the panchromatic band (Bands10T).

For the assessment of the land cover classification based on time series of images (Groups TS1 and TS2), five variants of time series were classified and compared. The five variants include time series of the combinations of band 3 and band 4 of Landsat TM images (B3B4), time series of three (PC3) principal components of all the VIS/NIR bands in the TM image, time series of 6 bands except the thermal band (6bands), time series of only the single thermal bands and time series of all the 7bands from the TM images. Band 3 and band 4 of Landsat TM image refer to the red and near infrared spectrum, of which the combination (e.g. as NDVI) is useful for distinguishing the vegetation, soil, water and land interface. Principal Component Analysis (PCA) was applied to the atmospheric corrected images with 6 bands (excluding the thermal band 6) for dimension reduction. The effectiveness of PCA for the identification of land cover changes has been reported in previous studies (Almeida-Filho and Shimabukuro, 2002; Singh, 1989). The three components of the 6 Landsat/TM bands are mainly related to the information of the land cover and land use, which explains approximately 98% of the data variability of all bands. Figure 3.2 shows the general classification procedure of all the time series Landsat images.
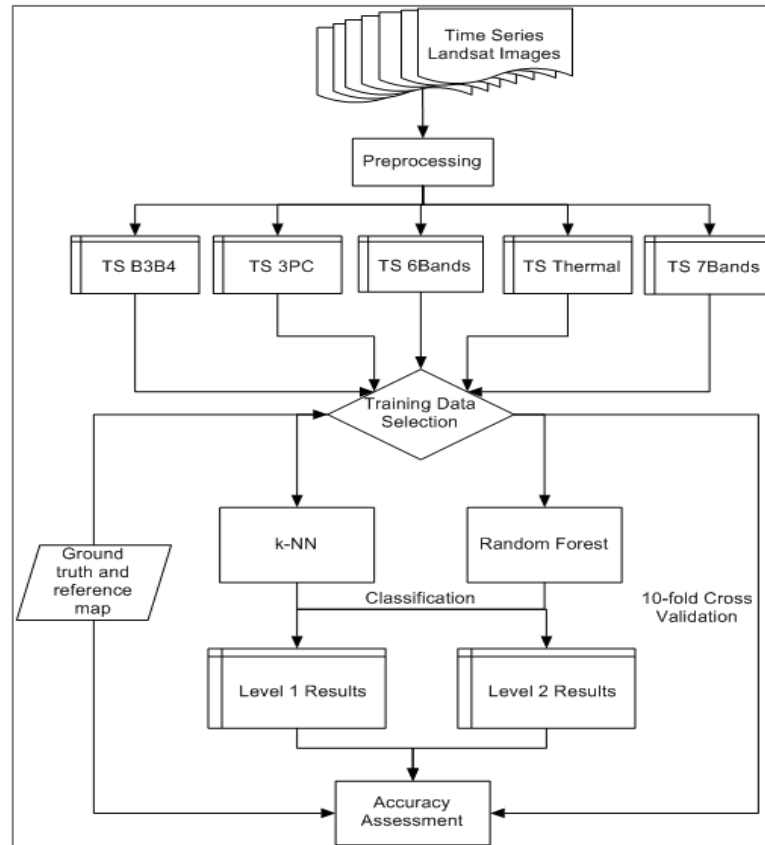
Figure 3.2 Flowchart of the land cover classification and accuracy assessment process: the time series images were derived from the Landsat 4/5 TM images by preprocessing including: the Band3 and Band4 combination (TS B3B4), first three principal components (TS 3PC) of the VIS/NIR bands from TM images, six bands combination except the thermal band (TS 6Bands), the thermal band (TS Thermal) and all the bands combination (TS 7Bands); then based on the ground truth and reference maps training data were selected and used for the k-nearest neighbor and Random Forest algorithms for Level 1 and Level 2 classification; 10-fold cross validation was applied to the both classification methods and then calculated for the accuracy statistics.

3.5.2 Classification Algorithms

In the field of land-cover classification based on satellite images, numerous machine learning methods are available and have been investigated and reviewed (Li et al., 2014; Lu and Weng, 2007). Since the general intercomparison of classification methods was not the focus of this

study, experience from previous investigations was used (Samaniego et al., 2008; Samaniego and Schulz, 2009), and two widely applied methods, the simplest k-NN and the more complex Random Forest algorithms were chosen for the land-cover classification given their good performance.

The k-NN method is one of the particularly simple classifier in concept, which is easy to apply but can be time consuming (Richards and Jia, 2006). Given an object, it examines the training samples in the multispectral feature space and chooses the closest class among the pre-specified number k of nearest neighbors. k is an integer value specified by the user and is highly data-dependent. In general a larger k suppresses the effects of noise, but makes the classification boundaries less distinct. Normally, k-NN needs a priori definition of a metric in the predictor space (Samaniego et al., 2008). There are several studies focusing on finding a reasonable distance to improve the performance of the classification algorithm (Collins et al., 2004; Samaniego and Schulz, 2009), such as the Manhattan distance, Euclidean distance, Chebychev distance, the similarity measures or the Modified Nearest Neighbor which searched for a metric in a lower dimensional space for separating a given class (Samaniego et al., 2008). Here, based on the previous study (Collins et al., 2004; Samaniego and Schulz, 2009) and comparison of the classification performance with different k values and metrics, the optimal number of nearest neighbors is defined as 5 and the distance metric is determined by the standard Euclidean metric.

Another ensemble learning algorithm called Random Forest (RF) is also applied in this study. RF is an ensemble of classification trees and each tree contributes with a single vote for the assignment of the most frequent class to the input data (Breiman, 2001). Breiman (Breiman, 2001) introduced RF by using bagging or bootstrap aggregating with a random subset of input features in the division of every node to make the trees grow from different training data subsets. The RF algorithm can handle high dimensional data and uses a large number of trees in the ensemble without variable deletion and estimates the importance of variables in the

classification (Rodriguez-Galiano et al., 2012b). The RF method has increasingly been applied in the land-cover classification given its higher accuracy and more robust capability to noise and outliners than other machine learning algorithms (Gislason et al., 2006; Rodriguez-Galiano et al., 2012a).

3.5.3 Validation and Accuracy Assessment

The *k*-fold cross validation, also called rotation estimation (Kohavi, 1995), is a model validation method for estimating generalization error. In *k*-fold cross-validation, the training set is split into *k* smaller sets and the classification model is trained using the *k*-1 of the folds as training data, then the resulting model is validated on the remaining part of the data. The accuracy of cross-validation is the average of value in the loop. In this study, 10-fold cross validation was performed with the samples obtained in the Section 2.3. The water body category was not considered in the accuracy assessment due to its small proportion based on the recommendation of the minimum of 50 samples for each category validation by Congalton (Congalton, 1991).

Error metrics were calculated to assess the classification accuracy, from which the OA, user's accuracy (UA) and producer's accuracy (PA) were derived (Congalton and Green, 2009). The OA present in this paper is the averaged value from 10-fold validation for each *k*-NN and Random Forest classification. User's accuracy refers to the fraction of correctly classified pixels with regard to all pixels classified as this class in the classified image and is also known as the reliability or commission error. Producer's accuracy means the fraction of correctly classified pixels with regard to all pixels of that ground truth class and can also be referred to the accuracy or omission error.

3.6 Results and Discussion

3.6.1 Classification Based on a Single Image (S1)

The land cover classification based on a single image was carried out with the Landsat 8 image from July 21, 2013. As detailed in section 3.1, three variants with different bands combination were considered and classified into the three land cover levels using the k-NN and Random Forest algorithm. The classification results and the accuracy statistics are summarized in Figure 3.3 and Table 3-4 and Table 3-5. Figure 3.3 (b)-(d) illustrate the land cover maps with the best OA among all the variants for each category. The consistent patterns can be visually observed in the forest and artificial areas, meanwhile the road in the west part of the catchment is clearly distinguished. For level 2 and level 3, the agricultural areas were classified in more detail based on the ground truth data. The major cropland and grassland areas have been well recognized but misclassification still exist especially between the different crops in Figure 3.3(d) with the low accuracy data in Table 3-5.
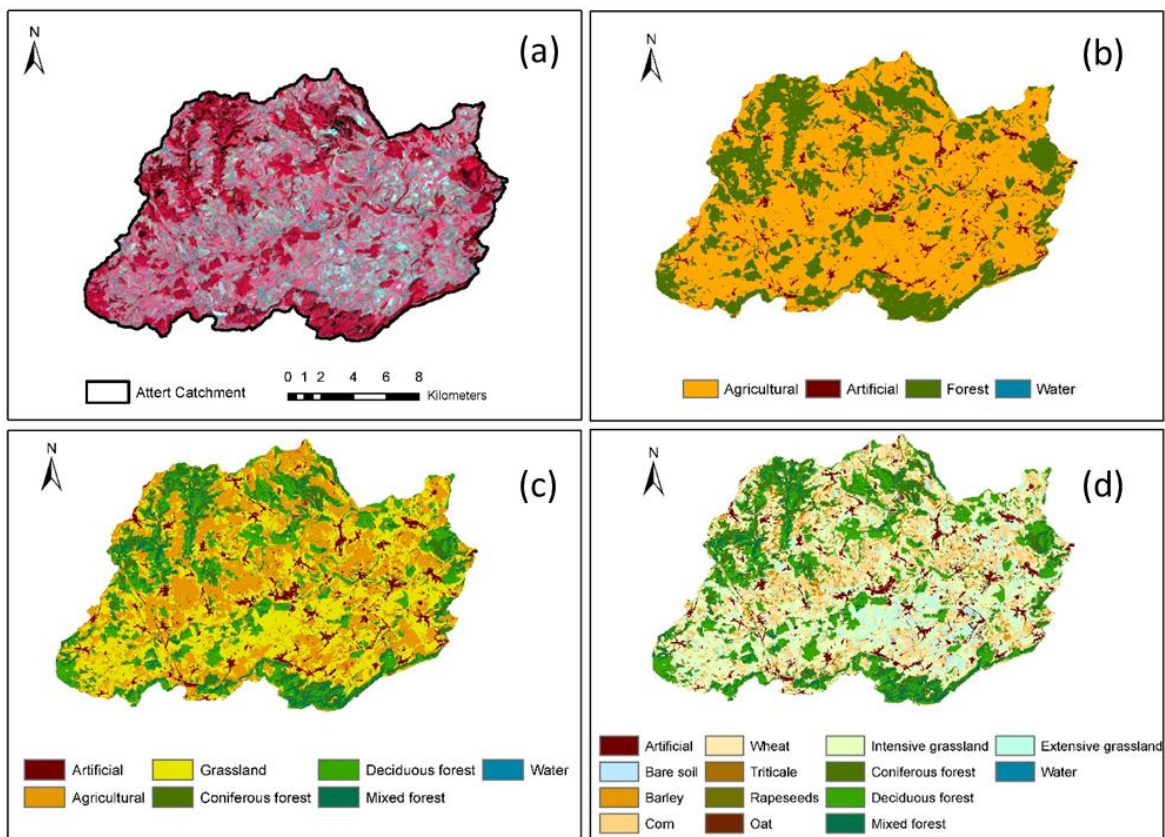
Figure 3.3 Four land cover maps from Landsat 8 of July, 2013: (a) False color composite image in RGB combination of bands 5, 4, 3; (b) Level 1 classification image with 4 classes by k-NN based on the 10 bands combination of the Landsat image; (c)-(d) Level 2 and Level 3 classification images with 7 and 14 classes by Random Forest based on the 10 bands combination.

Table 3-4 The mean value calculated by 10-fold cross validation method for the OA of the three images from Landsat 8 in 2013 with different band combination classified by k-NN and Random Forest: Bands4 represents the image with bands 2 to 5; Bands6T represents the image with bands 2 to 5 and the thermal bands 10 and 11; Bands10T indicates the image with all the 10 bands from Landsat 8 except the panchromatic band; k-NN5 and RF represents the nearest neighbor method with k =5 and Random Forest respectively.

Image classificatio n accuracy in 2013	Level 1 (%)		Level 2 (%)		Level 3 (%)	
	k-NN5	RF	*k*-NN5	RF	*k*-NN5	RF
Bands4 OA	97.6	97.6	83.9	84.7	68.7	69.9
Bands6T OA	98.1	98.1	87.0	87.9	74.1	74.7
Bands10T OA	**98.3**	98.2	91.9	**92.3**	79.6	**80.7**

It is clear that the variant Bands10T always achieved the best OA by making use of the available maximum spectral information with 10 bands (Table 3-4). The high overall accuracies around 98% for the Level 1 classification indicates that the Bands4 variant has sufficient information to classify the Level 1 category. The classification accuracy drops down strongly with the 80.7% OA value for Level 3 category, which is much lower than the commonly recommended 85% target for planning and management purposes (Anderson, 1976). However, it is worth noting that the additional information from the short wave infrared and the thermal spectrum provide more information and better accuracy especially for the Level 2 and Level 3 classification, which improve the OA of Bands10T about 5% to 8% for the Level 2 category and 6% to 12% for the Level 3 category than the Bands6T and Bands4.

Table 3-5 The best classification accuracy statistics from the 10-fold validation by Random Forest chosen for the data analysis of the single Landsat 8 image with 10 bands combination in 2013. PA refers to the Producer's accuracy, UA refers to the User's accuracy, -- represents no validation pixel available.

Level 1	PA	UA	Level 2	PA	UA	Level 3	PA	UA
Agriculture	99.3%	98.7%	Artificial	94.2%	94.3%	Artificial	89.1%	91.8%
Artificial	89.4%	93.1%	Cropland	91.8%	92.0%	Bare soil	80.4%	86.5%
Forest	98.8%	99.3%	Grassland	92.5%	91.9%	Barley	56.7%	59.7%
Water	--	--	Conifer	98.8%	94.6%	Corn	72.3%	64.9%
			Deciduous	97.3%	95.5%	Wheat	62.7%	60.2%
OA	98.7%		Mixed forest	79.5%	92.1%	Triticale	30.4%	47.1%
			Water	--	--	Rapeseeds	47.8%	66%
						Oat	48.4%	68.2%
			OA	92.7%		Intensive Grassland	93.1%	90.7%
						Conifer	99.0%	98.1%
						Deciduous	97.9%	94.9%
						Mixed forest	81.9%	92.6%
						Extensive grassland	88.2%	90.9%
						Water	--	--
						OA	81.2%	

Table 3-6 Confusion matrix for the Level 3 category of single Landsat 8 image in July, 2013 with 10 bands combination. The column indicates the referred data points for the 14 classes from field campaign and the row represents the classified data by Random Forest.

Classified \ Referred	Artificial	Bare Soil	Barley	Corn	Wheat	Triticale	Rapeseeds	Oat	Dense Grassland	Conifer	Deciduous	Mixed Forest	Sparse Grassland	Water	Sum
Artificial	156	6	0	9	1	0	0	0	2	0	0	0	1	0	175
Bare Soil	5	45	2	4	0	0	0	0	0	0	0	0	0	0	56
Barley	0	0	102	20	39	4	7	0	2	0	0	0	6	0	180
Corn	4	1	17	310	56	4	5	0	17	0	2	1	12	0	429
Wheat	1	0	30	85	274	15	2	5	21	0	1	0	3	0	437
Triticale	0	0	4	13	31	24	3	1	3	0	0	0	0	0	79
Rapeseeds	0	0	7	6	18	4	33	0	0	0	0	0	1	0	69
Oat	0	0	2	2	8	0	0	15	3	0	1	0	0	0	31
Dense Grassland	2	0	2	23	13	0	0	1	674	0	0	0	9	0	724
Conifer	0	0	0	0	1	0	0	0	0	205	0	1	0	0	207
Deciduous	0	0	0	1	0	0	0	0	1	0	428	7	0	0	437
Mixed Forest	0	0	0	1	0	0	0	0	2	3	19	113	0	0	138
Sparse Grassland	2	0	5	4	14	0	0	0	18	0	0	0	321	0	364
Water	0	0	0	0	0	0	0	0	0	1	0	0	0	0	1
Sum	170	52	171	478	455	51	50	22	743	209	451	122	353	0	3327

Table 3-5 lists the UA and PA for all the three classification levels considering the best OA value between the k-NN and Random Forest algorithm in the classification procedure. For the various land covers among the three levels, forest category is one of the best classified with high PA and UA above 95%. For instance, the conifer got highest accuracy in Level 2 and Level 3, followed by the deciduous and the mixed forest. At the aquired date of image, the cropland including wheat, barley, rapeseeds, corn and other types show various maturity, i.e. a few corn fields were newly planted whereas several wheat or barley grew mature enough for harvest. Therefore, compared to the classification between cropland and grassland in Level 2, serious misclassification existed in Level 3 category among the different crop fields. The confusion matrix in Table 3-6 shows the validation data for the 14 classes of Level 3. Because of limited reference pixels from the field campaign, the validation pixels of oat did not exceed the recommended number of 50. Here it was kept for the comparison need. The matrix provides detail information about the mixture of different crops with similar growing characteristics, such as barley and wheat, triticale and wheat. All in all, this single-date Landsat 8 image did not provide sufficient information for the detailled croplands distinguishment and at least one other image at spring or autumn will be needed to supplement the classification. However, such an (cloudfree) image was not available for this year.

3.6.2 Level 1 Classification Based on Time Series of Images (TS1 and TS2)
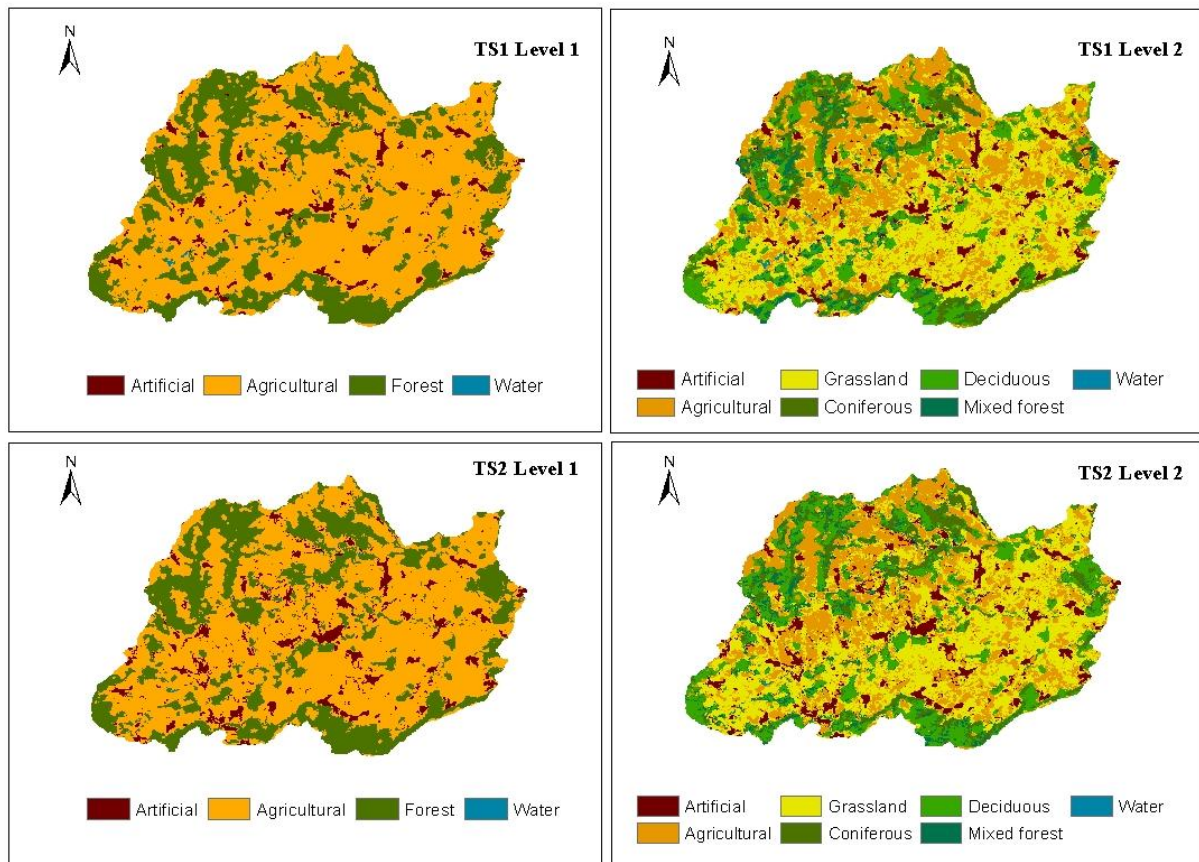
Figure 3.4 Level 1 and Level 2 land cover maps classified by the k-NN algorithm with time series of thermal images from Landsat 4/5 TM for TS1 and TS2.

Besides the evaluation of the single-date Landsat 8 image, the land cover classification with the time series of images for the Level 1 and Level 2 categories (Figure 3.4) was carried out via 5 different variants of spectral bands combination as described in section 3.1.

Table 3-7 list the OA for the times series TS1 and TS2 images with regard to the Level 1 land cover category by k-NN and Random Forest. The accuracy data are given for both classification methods with the image from the earliest time and then successively adding the images up to each time step. As expected, the OA improves with the increase of the images for all the variants. Taking the full set of images in TS1 into account, the B3B4 provides the lowest OA

compared to the results of the 3PC, 6Bands and 7Bands images. The OA from 3PC is very close to the data from the 6Bands starting from the image number of 4. The overall accuracies of the thermal images classified by k-NN varies greatly in the first three time steps. In comparison, the Random Forest demonstrated more stable performance illustrated in Figure 3.5. When the image number is greater than 5, the thermal bands began to show their superiority with higher OA than the B3B4, 3PC and 6Bands combination. Both the thermal and the 7Bands images obtained the best OA of 99.1% by the k-NN algorithm.

The classification results from group TS2 indicate the same tendency that the 3PC and 6Bands show higher OA than the data of the B3B4 and the thermal band. In contrast to the results of the group TS1, the thermal images of TS2 with the maximum 6 images did not exceed the corresponding results of the 3PC and 6Bands. The thermal band (the right plot in Figure 3.5) varies when image number is small and the OA increases to the same level as the B3B4 classification at the image number of 6. From Table 3-7, it is to note that the time series of 7Bands classification performed by k-NN get the best OA at each time step compared to the other group data. The 3PC images provide nearly similar OA data as the 6Bands when the image number is greater than 3.The best OA among all the data is 99.2% from the 7Bands classification calculated by the k-NN. The best OA of the thermal images is 98.7% by k-NN and 98.5% by Random Forest, which is slightly lower than the best OA of 7Bands.
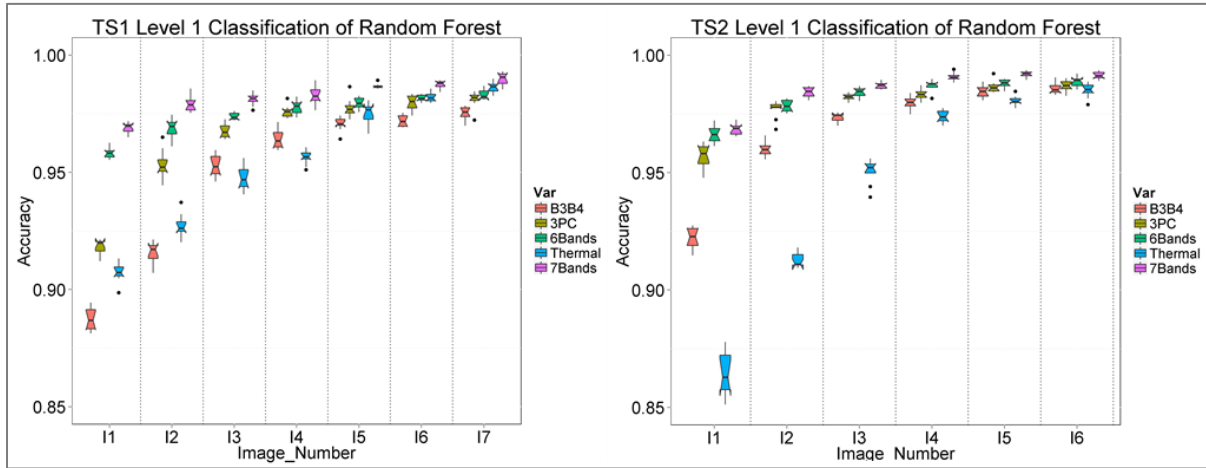
Figure 3.5 TS1 and TS2 boxplot of the 10-fold Level 1 classification overall accuracy variation by Random Forest for the time series images of the combination of band 3 and band 4 (B3B4), the first three principal components (3PC), the combination of 6 bands (6Bands), the thermal bands and the combination of 7 bands (7Bands).

Table 3-7 Overall Accuracy of Level 1 classification by k-NN and Random Forest based on the time series images of the combination of band 3 and band 4 (B3B4), the first three principal components (3PC), the combination of 6 bands (6Bands), the thermal bands and the combination of 7 bands (7Bands).

Image Number	B3B4 (%)		3PC (%)		6Bands (%)		Thermal (%)		7Bands (%)	
	k-NN	RF	k-NN	RF	k-NN	RF	k-NN	RF	k-NN	RF
TS1-1	78.0	88.7	91.9	91.8	95.9	95.8	70.1	91.0	**96.9**	**96.9**
TS1-2	92.3	91.6	95.5	95.3	96.9	96.9	79.1	92.8	97.6	**97.9**
TS1-3	95.6	95.3	97.1	96.8	97.4	97.4	88.3	94.8	**98.3**	98.1
TS1-4	96.3	96.4	98.0	97.6	98.0	97.8	94.0	95.7	**98.5**	98.3
TS1-5	97.2	97.1	98.2	97.8	98.4	98.0	97.6	97.5	**98.7**	**98.7**
TS1-6	97.4	97.2	98.4	98.0	98.3	98.2	98.6	98.1	**98.9**	98.7
TS1-7	97.5	97.5	98.6	98.1	98.7	98.3	**99.1**	98.6	**99.1**	99.0
TS2-1	83.7	90.2	95.6	93.5	96.2	95.3	54.8	84.8	**97.1**	96.9
TS2-2	96.1	95.7	97.9	97.0	97.9	97.7	85.6	91.5	**98.5**	98.4
TS2-3	97.5	97.2	98.4	98.1	98.5	98.2	93.5	95.0	**98.9**	98.7
TS2-4	98.2	98.0	98.6	98.2	98.7	98.7	96.5	97.0	**99.1**	**99.1**
TS2-5	98.6	98.3	99.0	98.5	98.9	98.7	97.9	98.0	**99.2**	**99.2**
TS2-6	98.7	98.6	99.0	98.7	99.0	98.8	98.7	98.5	**99.2**	99.1

3.6.3 Level 2 Classification Based on Time Series of Images (TS1 and TS2)

The boxplot in Figure 3.6 shows the variation of the OA data with regard to the Level 2 land cover classification performed by the Random Forest. Similar to the Level 1 classification, the k-NN algorithm has larger variations compared to the Random Forest method when only using the thermal information with an image number smaller than 4. The OA data by Random Forest varies relatively stable for both TS1 and TS2 data.

The best OA of TS1 Level 2 classification is 96.6% achieved by the time series of 7Bands images (Table 3-8). The largest OA from the thermal images is obtained by k-NN as 96.3%, which is about 0.9% to 3.6% higher than the accuracies of B3B4, 3PC and 6Bands. Starting from 5 images, the time series of 3PC and 6Bands in TS1 obtain OA. The classification results using the thermal information by the Random Forest algorithm start to exceed the accuracy of time series of B3B4, 3PC and 6Bands with image number 6. The bold data in Table 3-7 and Table 3-8 imply the best accuracy data among all the OA at each time step. The best OA of 96.9% from the Level 2 classification results of TS2 (Table 3-8) comes from the 7Bands image classified by the k-NN algorithm, followed by the 6Bands (96.5%), 3PC (96.1%), B3B4 (94.8%) and the thermal band (93.9%). By contrast to the TS1 Level 2 classification results, the time series of thermal images obtain the lowest OA at each time step for the TS2. The best value from the thermal band is 93.9% and the OA starts to exceed 85% when the images are more than 4. The 3PC and 6Bands also achieve the similar accuracy from the image number of 4. The TS2 boxplot in Figure 3.6 illustrates that the OA increases with the image number for all the time series images, whereas the performance of Level 2 classification based on the TS2 thermal images is not as good as that of the TS1 thermal images.
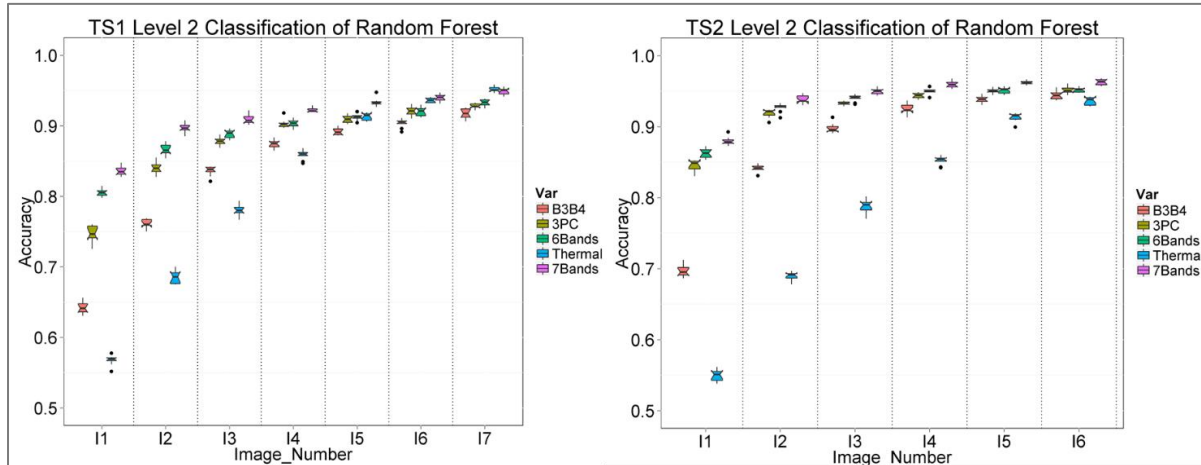
Figure 3.6 TS1 and TS2 boxplot of the 10-fold Level 2 classification overall accuracy variation by Random Forest for time series images of the combination of band 3 and band 4 (B3B4), the first three principal components (3PC), the combination of 6 bands (6Bands), the thermal bands and the combination of 7 bands (7Bands).

Table 3-8 Overall Accuracy of Level 2 classification by k-NN and Random Forest based on the time series images of the five variants.

Image Number	B3B4 (%)		3PC (%)		6Bands (%)		Thermal (%)		7Bands (%)	
	k-NN	RF	k-NN	RF	k-NN	RF	k-NN	RF	k-NN	RF
TS1-1	51.0	64.3	74.6	74.6	81.0	80.6	37.0	56.6	82.9	**83.6**
TS1-2	76.3	76.1	85.7	84.0	87.1	86.6	52.1	68.0	**90.3**	89.7
TS1-3	83.7	83.6	89.8	87.8	90.1	88.8	65.4	77.8	**92.5**	90.9
TS1-4	87.7	87.4	92.2	90.3	92.8	90.3	81.0	85.8	**94.0**	92.3
TS1-5	89.7	89.2	93.5	90.9	93.7	91.2	89.7	91.3	**95.2**	93.3
TS1-6	91.2	90.4	94.5	92.1	94.6	92.0	93.9	93.9	**95.9**	94.0
TS1-7	92.7	91.7	95.3	92.8	95.4	93.3	**96.3**	95.3	**96.6**	94.9

Image Number	B3B4 (%)	3PC (%)	6Bands (%)	Thermal (%)	7Bands (%)	Image Number	B3B4 (%)	3PC (%)	6Bands (%)	Thermal (%)
	k-NN	RF	*k*-NN	RF	*k*-NN		*k*-NN	RF	*k*-NN	RF
TS2-1	55.9	65.6	81.4	80.7	84.5	84.3	37.8	56.5	**88.4**	88.0
TS2-2	80.9	80.6	91.0	90.5	91.5	91.0	51.4	66.9	**94.6**	93.8
TS2-3	89.8	88.9	93.9	93.3	94.6	93.9	65.7	76.5	**95.6**	95.0
TS2-4	92.8	91.6	95.2	94.2	95.1	94.7	81.0	84.6	**96.4**	96.0
TS2-5	93.8	93.4	95.8	94.6	96.1	95.2	88.0	89.1	**96.8**	96.2
TS2-6	94.8	94.2	96.1	95.1	96.5	95.3	93.9	93.3	**96.9**	96.3

The results of sections 4.1 to 4.3 can be summarized as follows: For the single image classification: i) Bands4 (97.6%), Bands6T (98.1%) and Bands10T (98.3%) achieved similar OA value of 98% ± 0.4% for the Level 1 classification; ii) Bands6T and Bands10T including the two thermal bands got about 5% and 8% higher OA value than that of the Bands4 for the Level 2 classification; iii) Bands6T and Bands10T obtained 6% and 12% higher accuracy than the Bands4 for the Level 3 classification.

For the Level 1 classification by the time series of images: i) the thermal images provide comparatively similar OA for both the TS1 and TS2 Level 1 classification, with the best OA of 99.1% for the TS1 and 98.7% for the TS2; ii) When the image number is greater than 5, the thermal band shows better OA compared to the B3B4, 3PC and 6Bands for the TS1; iii) the 7Bands combination achieved the best OA at each time step mostly classified by the *k*-NN, with the OA of 99.1% for the TS1 and 99.2% for the TS2; iv) starting from 4 images, the 3PC and 6Bands provided comparable accuracy data.

For the Level 2 classification by the time series of images: i) the best accuracy data of TS1 and TS2 are derived from the 7Bands among all the other images by *k*-NN with the OA of 96.6%

and 96.9% respectively; ii) the thermal images get the largest OA at the image number of 6 with 96.3% for TS1 at the image number of 7, which is higher than B3B4, 3PC and 6Bands; iii) the TS2 obtained the lowest OA at each time step compared to the other variants and the best OA of 93.9% at the image number of 6; iv) the same feature also exists in the Level 2 classification for the 3PC and 6Bands with the similar accuracy data when the image number is greater than 4.

3.7 Conclusions

The effectiveness of the thermal information/bands with regard to land cover classification using a single Landsat 8 image (including two thermal bands) and time series of Landsat 4/5 images (including one thermal band) was investigated for the Attert Catchment in Luxemburg. The single image was classified into three levels with 4, 7 and 14 LULC classes respectively and the time series of images were classified into the first two levels (level 3 could not be analyzed due to the lack of ground truth data during the time frame of available images). The k-NN and the Random Forest algorithm were applied and assessed within a 10-fold cross-validation framework.

Firstly, the accuracy results from three variants of the single-date Landsat 8 image indicate that adding the thermal bands has clearly improved the accuracy of the Level 2 and Level 3 classification. The three variants achieved similar high OA of 98% ± 0.4% for the Level 1 classification. For the Level 2 and Level 3, Bands10T performed well with the best accuracy data, followed by the Bands6T and Bands4, which is 6% and 12% higher for the Level 3 classification. The OA from Bands6T including the two thermal bands are 3% and 6% higher respectively for the Level 2 and Level 3 category than the data of Bands4 without thermal bands. The results indicate that for the single Landsat 8 image classification, adding the thermal band to the VIR/NIR bands could improve the accuracy by 3% to 6% for Level 2 and Level 3 classification. As thermal bands are routinely available from different sensor platforms, their

incorporation as input into the classification should also be done on a routine base, thereby significantly increasing classification accuracy.

Secondly, the results from time series of thermal images also demonstrate that the inclusion of thermal band significantly improves the LULC classification, compared to using standard VIS/NIR bands. The classification based on time series of thermal images provided comparably high OA when compared to the B3B4, 3PC, 6Bands and 7Bands images. TS1 thermal images obatined the best OA of 99.1% for Level 1 classification and 96.3% for the Level 2 classification. The time series of TS2 thermal images achieved the OA of 98.2% for the Level 1 and 93.9% for the Level 2. It is interesting to observe that the time series of thermal images could provide OA that are as good or even better than using the visible and near-infrared bands in the land cover classification, especially when the combination number of images used is higher than 5.

Time series of TS2 thermal images also achieved comparatively high accuracy at the image number of 6, although the value is not higher than other images. Based on our results, a time-series of at least 5 or 6 thermal images is recommended as being almost optimal for situations that are similar to our study area. If the images from different years are obtained in the area with varying land cover and land use, the classification catalog and the selection of training set should be paid more attention with more land cover catalogs or taking the land cover change as the new class to ensure the consistence of the images in different years. In this study, the cloud free Landsat images were received mainly in the spring and summer time. They demonstrate the temperature discrepancies between various types of land cover especially for the agriculture areas, which is very effective for the Level 2 classification with the high OA from 93.9% to 96.3%. For the classification with the time series of images in the same year, at least two images from spring or summer time are recommended as the complementary sources.

Our study is not aiming at replacing the existed profound classification ways, but trying to add the thermal bands to improve the land cover classification based on the single image or the time series of images. The incorporation of thermal information improved the land cover classification indicated by better OA and Kappa statistics. But also, thermal information alone provides similar or even better results when compared to the other time series of visible and near- infrared bands combination and/or principal components. Therefore, in case of failures or non-availability of VIS/NIR band data (as has been the case e.g. for the ASTER NIR bands), the thermal information could serve as a good substitute input in land cover classification experiments.

So far, the study area is limited to the Attert catchment in Luxembourg and the detailed land cover catalog is only classified to Level 2 (7 classes) when using time series of images, due to the lack of images in the same year for the agricultural area and therefore missing ground truth information. Because of the complicated atmosphere conditions, the preprocessing of the time series images probably could further benefit from other novel correction procedures, such as the relative radiometric normalization(Vicente-Serrano et al., 2008). Further investigation of the time series of thermal remote sensing will be extended to the more specific classification for higher level with more specific land covers (such as Level 3 CORINE classes and/or application in agricultural and hydrological land cover types). The thermal bands in Landsat satellites have the limitation of a coarser spatial resolution when compared to the VIS/NIR bands, but the developed data fusion methods (such as e.g. wavelet fusion method (Bagan et al., 2003) or the Spatial and Temporal Adaptive Reflectance Fusion Model (STARFM) (Feng et al., 2006; Zhu et al., 2010)). Other thermal sensors with wider spectral range such as ASTER or the sensor installed on the drone with finer spatial resolution and hyperspectral data (Segl et al., 2003) should also be explored to aggregate the information for the regional land cover classification, but this is subject of ongoing and future research.

4   Accuracy Assessment of Land Cover Maps Using the Polygon-based Cross Validation Method

This chapter has been edited and published as Sun, L., and K. Schulz, 2015, Response to Johnson B.A. Scale Issues Related to the Accuracy Assessment of Land Use/Land Cover Maps Produced Using Multi-Resolution Data: Comments on "The Improvement of Land Cover Classification by Thermal Remote Sensing". Remote Sens. 2015, 7, 8368–8390: Remote Sensing, v. 7, p. 13440.

4.1   Abstract

As a complement to the pixel-based cross validation (CV) method, a polygon-based CV method is utilized in this section to classify different levels of land cover categories using a single-date Landsat 8 image and time series of Landsat TM images. Also, different variants of band combinations, with and without the thermal bands, were considered. The results demonstrate that the inclusion of thermal information into the classification process will improve the classification performance, as was already shown in the Chapter 3. However, it is also demonstrated that the polygon-based CV method produced lower overall accuracy values when compared to the pixel-based CV method. This confirms the argument made by Johnson that a correlation of calibration and validation data due to random sampling of multi-scale data will overestimate the performance of the classifier, and independent polygon-based CV methods have to be applied instead.

4.2   Introduction

In Chapter 3, we made use of single-date Landsat 8 and time series of Landsat 4/5 images to investigate the potential of thermal information for an improved land cover classification in

the Attert Catchment in the Grand Duchy of Luxembourg (Sun and Schulz, 2015). The classification results were assessed by a 10-fold pixel based cross-validation (CV) method where pixel were randomly selected and the overall accuracy (OA) taken as an evaluation measure. We found that the inclusion of thermal bands can improve the accuracy of the land cover classification when added to the multispectral bands. Based on the accuracy assessment, it demonstrated that the time series of thermal images alone produced similar classification results when compared to all other VIS/NIR and TIR band combinations.

Whereas, a flaw was found in the pixel-based CV method. Johnson pointed out that the high accuracy data produced by the thermal images were likely caused by the overestimation of the pixel-based CV method (Johnson, 2015). In this case, additional evaluation method would be very helpful for the evaluation of land cover maps. Therefore, in this study,. we proposed the new CV method based on the region-of-interest (ROI) / polygon level, aiming to investigate for the effectiveness of avoiding the spatial autocorrelation between training and validation pixels given multi-resolution data.

It is well-known that various arguments and numerous data fusion methods exist around the accuracy assessment of the multi-scale remotely sensed images (Congalton, 1991; Congalton and Green, 2009; Foody, 2002) (Colditz et al., 2006; Zhu et al., 2010). With more focus on the evaluation of the thermal bands compared to the other multispectral variables, the accuracy assessment problems should be noted when the land cover classification is related to the scale issues of the resampled thermal images were neglected.

In the following sections, we briefly introduce the new assessment procedure and present the classification results for both the single-date and time series of image applications and compare the accuracy data with the pixel-based CV method. The data sources and classification methods are the same as described in Chapter 3.

4.3 Polygon-based Cross Validation Method

The polygon-based CV method assumes the polygons as the indpendant sample unit, and samples the training and validataion polygons based on the 10-fold CV method. Here, the training and validation samples were collected using the area of interest tool of the drawing toolbox in the ERDAS software; the polygons here are the same as in the Chapter 3. However, in order to make sure the pixels from the polygon as pure as possible, here the pixels were kept only when their central points are inside the polygon; the polygons were then refined. This leads to the slightly smaller sample sizes compared to Chapter 3. As we are not aiming at evaluating the effects of the training size on the classification accuracy, here the comparison between the pixel-based CV method and the polygon-based CV method was conducted using the same size of samples (pixels with central point inside the polygon).

For all land cover categories (except for water bodies) more than 10 polygons of ground truth data exists and there is little difference among the size of each polygon. For the 10-fold polygon-based cross validation, all polygons were split into 10 smaller sets and reorganized into 10 groups of data. The classification model was trained using pixels from nine groups of polygons (training data); the resulting model is then validated on the remaining group (validation data), and this procedure is repeated 10-times so that each group is used for validation once. In this way the correlation of multi-resolutions calibration and validation is avoided.

4.4 Results and Discussion

In this section, the accuracy statistics for a land cover classification applying both the original pixel based CV method and the polygon-based CV method are compared. Input data (a single-date Landsat 8 image on 21 July 2013, as well as time series of images from Landsat 4/5) and classification methods (Random Forest and the k-NN algorithms) are utilized.

4.4.1 Three-Level Classification Based on the Single-date Landsat 8 Image (S1)

In a first part, three variants of spectral band combinations of the single Landsat 8 image are used as input data and include: i) *Bands4,* only considering bands 2 to 5 in the VIS/NIR spectral region, without thermal bands; ii) *Bands6T*, as *Bands4,* but adding the two thermal bands 10 and 11, and (iii) *Bands10T*, including all bands, except the panchromatic band.

Table 4-1 summarizes the accuracy evaluation results for both the polygon-based and the pixel-based CV methods. The OA values for the classification of Level 1 land cover category obtained by the polygon-based CV are almost identical to the pixel-based evaluation for the three variants (97% to 98%). The OA values of Level 2 and Level 3 categories decreased about 5% and 9%, respectively, when switching to the polygon-based CV method. However, the increase in performance when adding the thermal bands into the classification is still pronounced and our conclusions drawn in the original paper still hold.

Table 4-1 The mean values of overall accuracy (OA) calculated by a polygon-based 10-fold CV method for the three variants from Landsat 8 in 2013 classified by k-NN and Random Forest: *Bands4,* only considering bands 2 to 5 in the VIS/NIR spectral region without thermal bands; *Bands6T*, as *Bands4,* but adding the two thermal bands 10 and 11, and *Bands10T*, including all bands, except the panchromatic band (see (Sun and Schulz, 2015) for a detailed channel/band description); *k*-NN5 and RF represents the nearest neighbor method with $k = 5$ and Random Forest, respectively.

Image classification accuracy in 2013	Level 1 (%)		Level 2 (%)		Level 3 (%)	
Assessed by Polygon-based CV	k-NN5	RF	k-NN5	RF	k-NN5	RF
Bands4	97.0	97.5	83.3	82.5	67.5	67.7
Bands6T	96.5	96.7	88.7	88.8	79.1	79.2
Bands10T	96.9	97.6	88.0	87.5	80.8	78.0
Assessed by Pixel-based CV	*k*-NN5	RF	*k*-NN5	RF	*k*-NN5	RF
Bands4	98.4	98.5	86.2	87.2	76.5	78.2
Bands6T	98.2	98.4	92.1	92.9	87.7	88.1
Bands10T	98.7	98.6	93.5	93.5	89.3	89.2

4.4.2 Two-Level Classification Based on Time Series of Images (TS1 and TS2)

The second part of the analysis focus on the differences between polygon-based and pixel-based CV methods when using time series of Landsat 4/5 images as input in the land cover classification system. The time series of images consist of two groups: *TS1*, including 7 images between 1984 and 1990, and *TS2*, including 6 images from 2006 to 2011. Five variants of the times series were analyzed including the following different band combinations: *B3B4*, the combinations of band 3 and band 4 of Landsat TM; *PC3,* the first three principal components of all VIS/NIR bands; *6Bands*, all bands except the thermal band; *Thermal* only the single thermal band; and *7Bands*, the combination of all 7 Landsat 4/5 bands.

The best OA value from the polygon-based CV method (Table 4-3Table 4-1) is almost the same as the results from the pixel-based CV(Table 4-2). For simplification, we here only list

the OA values of the polygon-based CV for Level 1 and Level 2 land cover categories classification. Table 4-3 shows OA values of the polygon-based CV for the classification of Level 1 land cover categories, whereby images within each group (*TS1, TS2*) are added subsequently as input. The classification performance increases with increasing numbers of images for all variants, a behavior that is already shown in Chapter 3 using a random pixel-based CV. Also, the *7Bands* variant including the thermal band still achieved the best overall performance, especially for smaller number of images included. Using the full set of available images all variants performed almost equally well, with OA values of 96-98.5%. When only using the thermal band, classification performance is reduced by 4.5 % compared to the pixel-based CV method, nicely demonstrating the overestimation of performance when correlation of multi-resolution calibration and validation data are existent.

Table 4-2 Overall Accuracy of Level 1 classification assessed by the pixel-based CV method using five variants of time series of images.

Image Number	B3B4 (%)		3PC (%)		6Bands (%)		Thermal (%)		7Bands (%)	
	k-NN	RF	k-NN	RF	k-NN	RF	k-NN	RF	k-NN	RF
TS1-1	89.1	89.8	93.0	93.2	97.0	96.9	91.2	91.8	97.6	97.4
TS1-2	93.9	93.6	96.3	96.3	97.5	97.8	92.9	93.6	98.5	98.6
TS1-3	96.8	96.8	97.9	97.7	98.1	98.1	94.9	95.2	98.8	98.6
TS1-4	97.4	97.4	98.5	98.3	98.7	98.5	95.9	96.1	99.0	98.7
TS1-5	98.1	98.0	98.7	98.2	98.9	98.6	98.3	98.0	99.2	99.1
TS1-6	98.3	98.0	99.0	98.5	99.1	98.7	98.8	98.4	99.2	99.1
TS1-7	98.5	98.4	99.2	98.6	99.3	98.8	99.4	98.8	99.5	99.4
TS2-1	93.2	93.0	96.7	96.6	97.4	97.5	85.0	86.4	97.9	97.8
TS2-2	97.5	97.3	98.7	98.6	98.9	98.5	91.8	92.6	99.2	99.0
TS2-3	98.5	98.4	99.2	98.9	99.1	99.0	95.6	95.6	99.3	99.3
TS2-4	98.9	98.8	99.3	99.0	99.2	99.1	98.0	97.9	99.5	99.5
TS2-5	99.4	99.2	99.6	99.2	99.5	99.3	98.4	98.5	99.6	99.5
TS2-6	99.4	99.3	99.6	99.3	99.6	99.4	99.1	98.9	99.7	99.5

Table 4-3 Overall Accuracy of Level 1 classification assessed by the polygon-based CV method using five variants of time series of images.

Image Number	B3B4 (%)		3PC (%)		6Bands (%)		Thermal (%)		7Bands (%)	
	k-NN	RF	*k*-NN	RF	*k*-NN	RF	*k*-NN	RF	*k*-NN	RF
TS1-1	86.6	87.7	91.6	91.2	86.6	87.7	87.8	90.5	96.2	95.5
TS1-2	91.9	90.9	94.8	94.4	95.6	96.2	88.4	88.8	96.5	97.0
TS1-3	94.2	94.9	95.9	95.8	96.4	96.1	88.4	90.9	96.8	96.3
TS1-4	95.6	96.2	96.8	96.7	96.4	97.1	88.7	87.0	96.8	96.7
TS1-5	96.1	96.2	96.8	96.2	97.3	97.0	91.7	91.3	96.8	97.3
TS1-6	96.1	95.9	97.2	96.3	96.8	97.4	91.7	89.3	96.9	97.1
TS1-7	96.0	96.6	97.4	97.2	97.7	97.6	93.2	94.6	97.7	97.0
TS2-1	91.4	91.5	95.6	94.2	95.8	95.5	80.0	86.0	95.9	95.1
TS2-2	95.1	95.9	97.2	96.9	97.5	97.0	84.5	89.3	97.8	97.0
TS2-3	97.1	97.2	98.0	97.6	98.4	97.8	92.6	92.7	98.3	98.2
TS2-4	97.0	97.8	97.8	97.9	97.8	98.2	95.0	92.6	98.7	98.0
TS2-5	98.1	97.9	98.7	98.3	98.0	99.0	94.2	94.4	98.3	98.3
TS2-6	98.5	98.2	98.6	98.1	98.6	98.4	95.4	95.4	98.3	98.4

The differences between the pixel-based based and a polygon-based 10-fold CV method are summarized in Figure 4.1. Here, OA values of all five variants from TS1 are summarized in a single box-plot for each time-step in the left image of Figure 4.1. It is clearly seen that on average the polygon-based CV method produced significant lower OA for both time series (*TS1, TS2*), again supporting the issue raised by Johnson's comment. Two variants of 6Bands and 7Bands were selected to show the detailed variation for the two methods in the right image of Figure 4.1. Besides the lower OA in comparison to the pixel-based CV method, the polygon-based CV still produced higher average OA for the 7Bands compared to the 6Bands without thermal band (the right image in Figure 4.1).
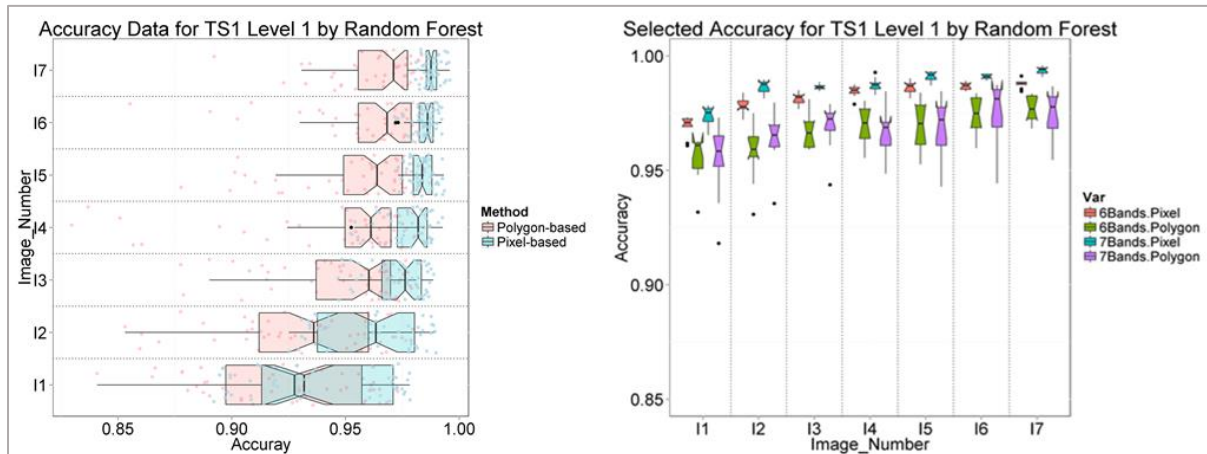
Figure 4.1 The distribution of OA values for the Level 1 land cover category classification using times series TS, the polygon-based and pixel-based 10-fold cross validation methods and the Random Forest methods. Left: all variants (Table 4-3 and Table 4-2) are summarized in a single box-plot; Right: OA comparison of selected variants of 6 bands without thermal band and 7 bands with thermal band.
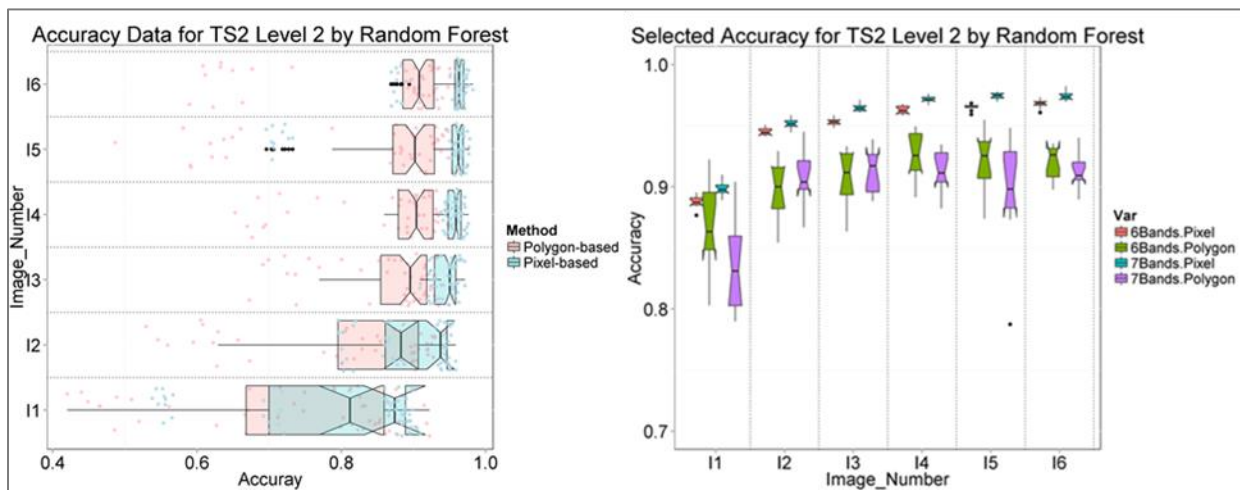
Figure 4.2 The distribution of OA values for the Level 2 land cover category classification using times series TS2, the polygon-based and pixel-based 10-fold cross validation methods and the Random Forest methods. (Left): all variants (Table 3) are summarized in a single box-plot; (Right): OA comparison of selected variants of 6Bands without thermal band and 7Bands with thermal band.

Table 4-4 Overall Accuracy of Level 2 classification assessed by the pixel-based CV method using five variants of time series of images.

Image Number	B3B4 (%)		3PC (%)		6Bands (%)		Thermal (%)		7Bands (%)	
	k-NN	RF	*k*-NN	RF	*k*-NN	RF	*k*-NN	RF	*k*-NN	RF
TS1-1	64.1	65.7	77.4	77.3	83.3	83.5	53.2	57.9	85.1	85.0
TS1-2	79.2	78.7	87.6	86.2	89.5	88.1	66.8	70.4	92.0	90.9
TS1-3	85.7	85.9	91.2	89.3	91.3	90.1	78.2	80.2	93.4	92.6
TS1-4	89.4	89.7	93.2	91.7	93.9	92.4	86.1	87.7	95.3	93.6
TS1-5	91.5	91.5	94.4	92.2	94.8	92.5	92.1	92.5	96.1	93.9
TS1-6	92.4	92.4	95.5	93.6	95.7	93.9	94.9	94.6	96.7	95.0
TS1-7	94.3	93.2	96.1	93.7	96.7	94.5	96.8	95.6	97.5	95.7
TS2-1	70.9	70.7	87.3	87.2	89.1	88.8	48.5	55.3	90.6	89.8
TS2-2	87.4	86.6	94.1	93.8	95.2	94.5	67.6	71.2	96.1	95.2
TS2-3	92.6	92.2	96.0	95.4	96.4	95.3	79.2	80.6	96.9	96.5
TS2-4	95.0	94.7	97.1	96.0	96.9	96.3	87.0	87.9	97.5	97.2
TS2-5	95.9	95.7	97.5	96.3	97.5	96.5	92.9	93.2	98.1	97.4
TS2-6	96.4	95.9	97.3	96.4	97.5	96.8	95.8	94.7	98.2	97.4

Repeating this analysis for the classification of Level 2 land cover categories, the differences in the performance measure (OA) between both CV methods is even more pronounced. Table 4-5 provide the accuracy data from the two CV methods for the Level 2 classification results. The average OA values are in general lower, as we analyze more specific land cover categories. The best OA for TS1 and TS2 are 86.6% and 93.3% when including the full set of images. The *7Bands* variant including the thermal band still achieved the best OA value of 86.6% for TS1, which is 10.9% lower than 97.5% from the pixel-based CV method. The best OA of TS2 from polygon-based CV method is about 5% lower than the corresponding value for the pixel-based CV method. Again, the *Thermal* variant including only the single thermal band, showed only a relatively weak performance with OA values of 72% and 74.5% for the both time series, compared to 96.8% 95.8% for the pixel-based CV method. Figure 4.2 summarizes the

differences between the pixel-based and the polygon-based CV methods in the left image and displays the variation of the selected 6Bands and 7Bands variants.

Table 4-5 Overall Accuracy of Level 2 classification assessed by the polygon-based CV method using five variants of time series of images.

Image Number	B3B4 (%)		3PC (%)		6Bands (%)		Thermal (%)		7Bands (%)	
	k-NN	RF	*k*-NN	RF	*k*-NN	RF	*k*-NN	RF	*k*-NN	RF
TS1-1	63.3	62.0	73.3	72.2	79.4	80.3	39.2	51.6	79.7	79.4
TS1-2	72.6	73.3	78.7	77.9	81.5	82.0	50.4	52.9	80.4	81.8
TS1-3	77.9	76.9	79.3	81.9	83.4	82.8	55.4	57.9	81.9	83.3
TS1-4	80.8	81.5	85.0	85.5	86.1	84.2	62.2	60.7	81.7	83.2
TS1-5	82.7	83.7	84.1	84.5	84.6	86.1	66.3	66.3	83.3	85.2
TS1-6	83.2	83.4	86.0	85.9	85.2	84.7	66.8	68.8	85.1	86.2
TS1-7	82.9	83.0	84.4	85.0	85.1	86.3	69.9	72.0	85.4	86.6
TS2-1	68.8	69.6	83.7	82.4	85.7	86.0	42.0	48.7	83.6	84.5
TS2-2	79.4	80.3	88.4	89.8	90.1	90.9	57.3	58.5	90.6	89.8
TS2-3	86.8	86.2	89.9	92.4	88.7	91.0	60.9	63.9	91.2	91.0
TS2-4	87.8	89.6	90.6	91.6	91.8	91.5	65.7	64.9	92.7	91.6
TS2-5	87.7	90.1	92.0	92.6	91.1	92.3	70.3	71.5	92.2	93.0
TS2-6	89.1	91.3	92.1	92.3	90.2	91.9	74.5	70.4	92.0	93.3

4.5 Conclusions

In this Chapter, a polygon-based CV method was applied to evaluate a land cover classification for three different levels of land cover categories. The classification was based on i) a single-date Landsat 8 image, and ii) time series of Landsat 4/5 images. The performance of classification results using the polygon-based CV were compared to a pixel-based CV method as applied in the Chapter 3.

For the single-date Landsat 8 image, the polygon-based method achieved almost similar accuracy values when compared to the pixel-based method, for all three-levels of land cover categories and for both classification methods used. When using time series of images, five different variants of band combinations with and without thermal information have been considered.

The accuracy of the Level 1 classification decreased but to a very acceptable and still useful level when compared to the commonly recommended standard of 85% (Anderson, 1976) (the best OA of Thermal is 94.6% and the best OA of 7Bands is 98.4%). The most obvious decline in performance is observed in the classification results for the Level 2 category, of which the best OA among the five variants is 93.3% and only 74.5 % when using only the thermal bands.

Consistent with our former findings, the inclusion of the thermal bands still improved the land cover classification in comparison to only using the VIS/NIR bands, also when assessing the classification results with a polygon type of CV approach. This has also been shown by other researcher, Eisavi et al. (Eisavi et al., 2015) applied the random forest classifier to the multi-temporal spectral and thermal features in land cover classification and found that the contribution of multi-temporal thermal information led to a considerable increase in the accuracy data. When using time series of thermal images to classify land cover at the Level 2 category, the performance and OA values were significantly lower for the polygon based CV when compared to the pixel-based evaluation for all band combinations considered. Again, the inclusion of thermal information improved the classification results on various levels.

In summary, a clear effect of correlation in the samples for calibration and validation due to multi-resolution data could be observed here. Classification accuracy (OA) was highly overestimated when ignoring correlation effects in the selection of calibration and validation data using time series of images as input. We therefore strongly recommend for the polygon-based CV method when using the resampled thermal images, or random sampling design could

possibly be helpful to avoid the correlation between the pixels. Nevertheless, the different choice of the CV method could improve the accuracy to a certain level. Even based on different evaluation method, the thermal data still proved its effectiveness, which is constistent with the conclusions in Chapter 3 that the inclusion of thermal data into the classification process, can significantly improve the classification results.

5 Vegetation Dynamics Modelling of Temporal LAI Prediction by Integrating the Climate Variables and MODIS LAI Data in a Mesoscale Catchment

This chapter is the revised version after the first round review of the paper submitted in Remote Sensing as Sun, L., and K. Schulz, 2015, Vegetation Dynamics Modelling of Temporal LAI Prediction by Integrating the Climate Variables and MODIS LAI Data in a Mesoscale Catchment.

5.1 Abstract

The distribution patterns and functions of vegetation dynamics are strongly required in the eco-hydrological models. The leaf area index (LAI) products derived from the remotely sensed data are particularly relevant for vegetation dynamics modelling. In the present study, we proposed a new LAI prediction model (Temperature Precipitation Vegetation Model, TPVM) by integrating two climate variables with the cumulative temperature and precipitation data. Taking the filtered Moderate Resolution Imaging Spectroradiometer (MODIS) LAI products as the optimization observation data, together with the Canopy Structure Dynamic Model (CSDM) and the Double Logistic Model (DLM), we applied the TPVM in the meso-scale Attert Catchment, Luxembourg. Featured phenological metrics from TPVM were also analysed for the interaction of climate and vegetation dynamics. The prediction results of seven land cover types indicated that the DLM and TPVM generally provided more realistic and accurate LAI data, whereas the TPVM performed superiorly for the agricultural land cover types compared to the other two models solely depending on the temperature data. Evaluated with the field measurements, TPVM got the best Person's correlation coefficient (CC) of 0.78. Further investigation of the applicability of TPVM in a larger-scale domain would be strongly recommended.

5.2 Introduction

Vegetation dynamics have been long studied for their functions in the terrestrial ecosystems, including land cover and land use change assessment, land surface process research, hydrological or climate change modelling and prediction (Schwartz et al., 2002; Sitch et al., 2003; White et al., 1997).Vegetation dynamics can reflect many climatic factors, including the temperature, precipitation, length of sun time, humidity and water use (de Beurs and Henebry, 2004; Peñuelas et al., 2004; Zhang et al., 2005). Leaf Area Index (LAI) is a dimensionless canopy indicator, which was defined by Watson (Watson, 1947) as the total one-sided area of leaf tissue per unit ground surface area. It is a key measure for evapotranspiration and photosynthesis models by reflecting the radiation absorption and turbulent transfers between vegetation and the atmosphere (Tesemma et al., 2014). Moreover, the LAI of vegetation serves as an important state parameter in the eco-hydrological models, such as the Soil-Vegetation-Atmosphere Transfer (SVAT), Surface Energy Balance (SEB), and Global Climate Models (GCM) (Glenn et al., 2008). The water interception amount and vegetation storage capacity were found to be directly related with the LAI depending on the vegetation type and the phenological stage (Xiao et al., 1998). The changing LAI modifies the surface water and energy budget which in turn affect the biochemical and hydrological cycles (Running and Coughlan, 1988). Therefore, accurate estimation of continuous LAI for the various land cover types has pronounced significance in the land surface modelling.

The seasonal dynamics of LAI respond differently to the climate changes depending on the land cover types. The seasonality can also be referred to the vegetation phenology (Leith, 1974), which can provide valuable information on the interaction between climate change and the ecosystems to temporal scales (González-Sanpedro et al., 2008; Liang and Schwartz, 2009; Schwartz and Karl, 1990) (intraseasonal and interannual) and are closely linked with the climate variability and the hydrological processs in a varying spatial scales (AghaKouchak et al., 2015; Atzberger et al., 2013; Hwang et al., 2011). The key factors affecting the vegetation

phenology are similar as the above-mentioned vegetation dynamics influences, including the air temperature, soil temperature, and water availability (Chuine et al., 2003; Forrest and Miller-Rushing, 2010; Kramer et al., 1999; Thuiller, 2007).

The traditional in situ observation of phenological events include the national phenological networks, GLOBE student observations (http://www.globe.gov/globe-data) and phenological gardens, which can provide relatively detailed and realistic timing data of the phenological events. However, the ground based observations cannot avoid the shortcoming of the expensive cost, the highly time consuming and operating bias. With the advances of the computer science and the concern of the global warming, more efforts have been made for the phenological models development. For the past decades, these efforts range from examining the controls of environmental factors, biological processes, and intrinsic traits (Migliavacca et al., 2008; Schwartz et al., 2006) on phenology, modelling techniques (Chuine et al., 2000a; Kathuroju et al., 2007; Palacios-Orueta et al., 2012), to ecosystem-level and evolutionary consequences of phenological changes (Chuine et al., 2004; Cleland et al., 2007).

In 1735, Reaumur proposed the most important assumption in the plant phenology modelling (Chuine et al., 2003): differences between years and locations in the date of phenological events could be explained by differences in daily temperatures from an arbitrary date to the date of the phenological event considered. Schwartz et al.(Schwartz et al., 2002) employed a regression model to test the significance and estimate the magnitude of changes in the relationship between thickness-maximum temperatures relative to first leaf date. Chuine et al. (Chuine et al., 1999) proposed several phenological models in the ecosystem research such as the Spring Warming Model, SeqSpar Model, SparSar Model). The onset models which assume that budburst occurs when a critical state of forcing temperature is reached, the state of forcing being the sum of the daily rate of forcing, which is solely a function of temperature. Chuine (Chuine et al., 2000b) also pointed out that the empirical and bioclimatic models should be species specific and calibrated at local scales.

Since 1980s, remote sensing techniques with low-cost and good temporal availability has been frequently used for the repetitive vegetation dynamics monitoring and plant phenology modelling (Justice et al., 1985; Koetz et al., 2005; Reed et al., 1994). Measured by the remote sensors, the characteristics of vegetation dynamics are usually represented by the vegetative indicators (VIs). The most frequently used indices include the normalized difference vegetation index (NDVI), enhanced vegetation index (EVI), the fraction of absorbed photosynthetically active radiation (FPAR) and leaf area index (LAI). These VI variables are normally served as the proxies for the canopy state variables estimation to describe the status of the plant growth (Sakamoto et al., 2005).

Time series of VIs from the satellite images can help the researchers in studying the phenological events across different scales (Beck et al., 2006; Fisher et al., 2006; White et al., 1997; Zhang et al., 2006). Due to the contamination by cloud or snow cover as well as instability in the data processing algorithms, the remotely sensed VI products mainly contain significant discontinuities (Kandasamy et al., 2013; Weiss et al., 2007), which need to be smoothed before application in the modelling process. White et al. (White et al., 1997) utilized the Best Index Slope Extraction (BISE) to smooth the daily Advanced Very High-Resolution Radiometer (AVHRR) NDVI data and to detect the phenological events with the predictive phenology models using the commonly available meteorological and climatological data. They concluded that the models could potentially be applied in large-scale biogeochemical models and monitoring vegetation response to interannual climatic variability. Schwartz et al. (Schwartz et al., 2002) compared the start of season (SOS) dates from the AVHRR data using different models and affirmed that the integrated satellite SOS with other regional phenology models offers considerable capability at the continental-scale monitoring of the spring onset. Zhang et al. (Zhang et al., 2003) proposed a series of piecewise logistic functions to fit the satellite-derived VI data and demonstrated the successful model application with Moderate Resolution Imaging Spectroradiometer (MODIS) data in vegetation phenology monitoring

over the United States. Moreover, other well-known functions include the Savitzky-Golay filter, asymmetric Gaussian, double logistic functions (DL) (Jonsson and Eklundh, 2002), curve-fit methodology (Fisher et al., 2006), as well as the a simple semi-mechanistic canopy structure dynamic model (CSDM) (Koetz et al., 2005).

In addition to the modelling method, the climate controls such as the temperature have been long studied by researchers (Kramer et al., 1999; Riha et al., 1996). However very limited studies have considered the precipitation in the vegetation dynamic modelling. Riha et al. (Riha et al., 1996) reported that the air temperature and precipitation are the major driving variables for crop simulation models and these models implicitly respond to the changes in both average temperature and precipitation. Kramer et al. (Kramer et al., 1999) recommended that the seasonality of climatic drivers affecting the phenological aspects of trees should be developed and carefully tested in the phenological models.

Therefore despite the tremendous development of the vegetation dynamics modelling in remote sensing area, efforts are still urgently needed to provide more reliable vegetation dynamics for the eco-hydrological models. Embedded in the German DFG research project CAOS ("Catchments as Organised Systems") (CAOS, 2012; Zehe et al., 2014), a key research question is to better understand how the different forms of spatial organization affect the storage and release of water and energy. Unlike most dynamics modelling based on the day of year as input but with more focus on the effects of climatic factors on the vegetation growth, this study aims at developing a simple vegetation dynamic model, which integrates the commonly-used climate variables to describe the growing status of different land cover types. Double logistic model (DLM) and CSDM models were also implemented using the cumulative temperature data for comparison in this study. Developed from the logistic functions, a new temperature-precipitation vegetation dynamics model (TPVM) was proposed for the Attert Catchment in accordance with the MODIS data. Four phenological metrics were derived from the time series of modelled LAI data and were analyzed for the seasonal patterns.

5.3   Data Sources

5.3.1 MODIS LAI Product

In MOD15A2H, the LAI of broadleaf canopy is defined as the one-sided green leaf area per unit ground area in broadleaf canopies and as one-half the total needle surface area per unit ground area in coniferous canopy. The MOD15A2H version 6 Level 4 LAI product is provided by the Land Processes Distributed Active Archive Center (LP DAAC) managed by the NASA Earth Science Data and Information System (ESDIS) project (R. Myneni, 2015a). The 8-day composite dataset together with the quality criteria (QC) layer are retrieved from the Terra MODIS platform with 500m pixel size.

The processing algorithm of the MOD15A2H LAI product includes a main Look-up-Table (LUT)and a back-up algorithm. The LUT is generated from the spectral information content of MODIS red and near-infrared surface reflectance by utilizing the 3D radiative transfer equation (Knyazikhin et al., 1998). The back-up algorithm that uses empirical relationships between NDVI and canopy LAI and FPAR. When the LUT method fails, the back-up method is utilized. Then, according to the data quality, the algorithm chooses the "best" pixel available from all the acquisitions of the Terra sensor from within the 8-day period (R. Myneni, 2015b).

Horn and Schulz (Horn and Schulz, 2010) analyzed and compared the MODIS LAI products with different quality criteria from both Terra and Aqua platform. They suggest that QC filtering should not be applied for the times series of MODIS LAI products and it would be better to take all pixels from the subset into account to achieve error nullification (Horn and Schulz, 2010). Following the recommendation, we kept all the pixel values from the MODIS products to maximize the useful retrievals in this study. However, due to the noise in the data, data filtering must be done before the modelling. The modified best index slope extraction (mBISE) method was utilized for the MOD15A2H data in this study. Lovell and Graetz (Lovell

and Graetz, 2001) modified the best index slope extraction (BISE) method by taking into account the local gradient of the data in the sliding window, which works effectively for the 10-composite NDVI data. Here, we set the sliding window for the MOD15A2H data as 24 days (3 images of 8-day interval from MOD15A2H) and the threshold for spurious spike as 0.1. Linearly interpolate the filtered data points from the mBISE method into continuous LAI datasets, which are considered as the observation data for optimization process in the modelling.

5.3.2 Climate Data

The gridded LAI pixel values for the meso-scale catchment can serve as valuable input sources for the hydrological and eco-climatic process modelling. In the model framework, we aim at providing the daily gridded LAI data with 500m spatial resolution. The input variables of the model include the same extent of cumulated daily mean temperature and daily sum precipitation datasets. The temperature and precipitation datasets were obtained from the metrological stations located at the Attert Catchment. The 2m air temperature data were interpolated from four meteorological stations and the precipitation were interpolated from six meteorological stations. Due to the few number of the available meteorological stations, here we used the simple Thiessen Polygons to interpolate the climate data into the 500m grid dataset in daily accumulative format for each year from 2003 to 2013. Figure 5.1 displays the modelling procedure. The locations of the meteorological stations can be referred to Figure 5.2.
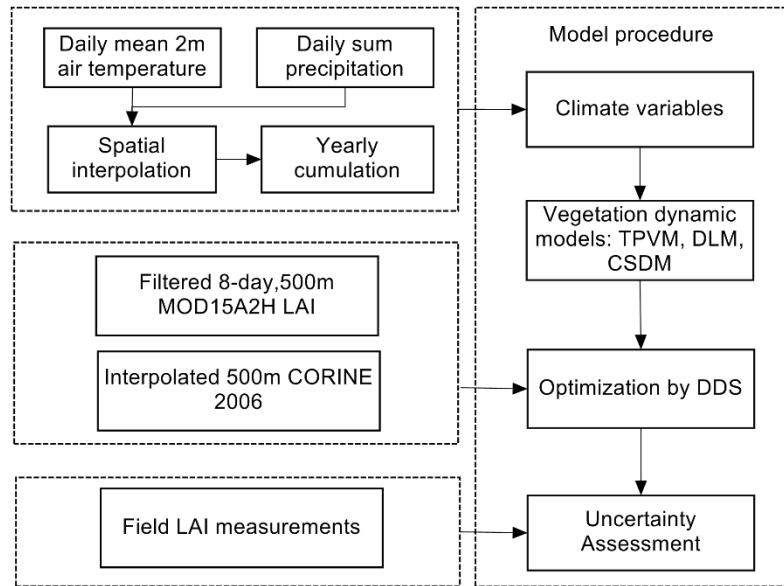
Figure 5.1 The vegetation dynamics modelling procedure include the data preprocessing of climate variable, then implementation of the three vegetation dynamic models, and the uncertainty assessment comparing with the field measured LAI.

5.3.3 Land Cover Maps

The reference land cover map in 2006 was downloaded from the COoRdination of INformation on the Environment (CORINE). CORINE 2006 was created with the joint efforts of about 38 countries in Europe and was published by the European Environment Agency. In this paper, Level-3 of the CORINE map was used for the vegetation dynamics modelling. In the Attert catchment, nine types of land cover exist according to the CORINE 2006, which include broad-leaved forest (BLF), complex cultivation patterns (CCP), coniferous forest (CF), discontinuous urban fabric, land principally occupied by agriculture with significant areas of natural vegetation (hereafter named as natural vegetation, NV), very small area of mineral extraction sites, mixed forest (MF), non-irrigated arable land (NIA) and the pastures (PAS). The artificial areas including the discontinuous urban fabric and mineral extraction sites were ignored in the modelling. Figure 5.2 presents the distribution map of Attert Catchment land cover types.
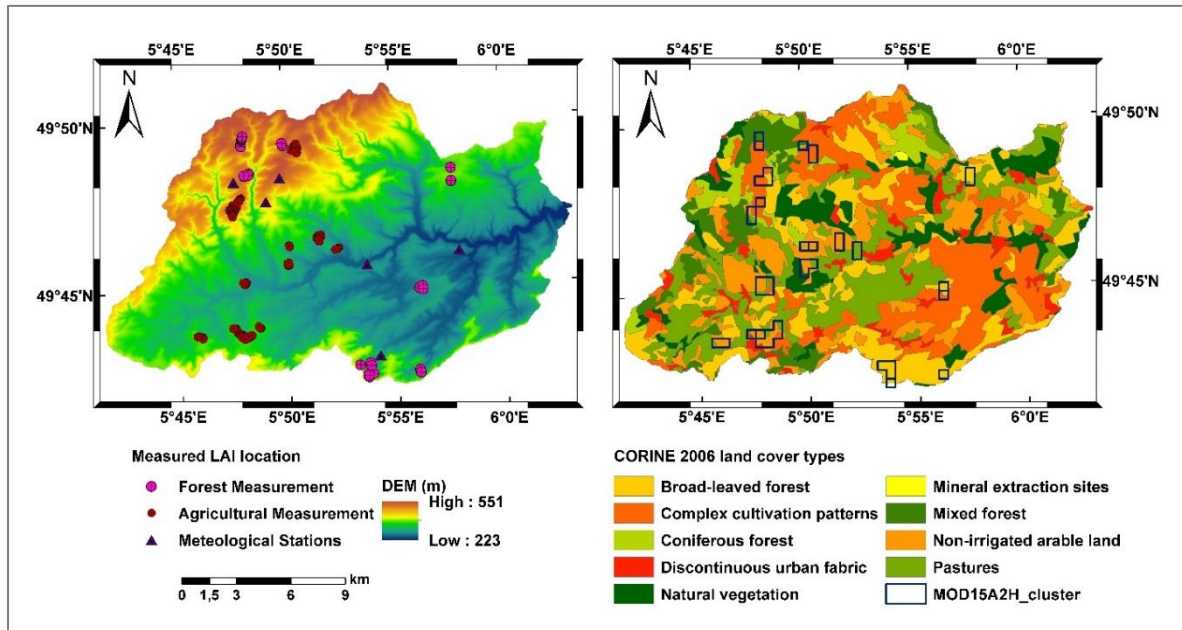
Figure 5.2 (a) DEM data with the measured LAI points in Attert Catchment; (b) CORINE Land cover map overlaid by the blue boxes of MODIS pixels corresponding to the field measurements.

5.3.4 Field LAI Measurement

The ground truth LAI measurements were conducted for two main land cover types, forest and agricultural areas. All the field measurements were conducted using the LAI-2200 Plant Canopy Analyzer from LI-COR Company and analyzed using the FV-2200 software (Inc., 2010). The LAI-2200 equipment calculates the LAI values as well as the apparent clumping factor, mean tilt angle, and other LAI statistics directly from light measurements made with a "fish-eye" optical sensor. Above and below measurements are made to calculate canopy light interception. The measurement can be further calculated in the FV-2200 software for the row crops. The forest plots were mainly measured with 90° view cap at the sunset in two periods including the summer (foliated in August 2012, May 2014 and September 2014) and the winter (defoliated in March 2014). Two LAI-2200 devices were used for measuring the above and below readings of the forest separately. The above reading were automatically measured outside the forest with clear view and the below reading were measured inside the forest with

90°. The measurement plots were 20m x 20m and one below reading was measured every 4m, resulting in a total of 36 measurements for one plot. Afterwards, the mean LAI value was calculated for each plot. For the agricultural area, the measurements were mainly conducted with a 180° view cap in cloudy conditions or sunny conditions with an umbrella to avoid the direct sunlight. In the row crop area, one above and four below readings were measured for one row and normally at least four to six rows were measured in one plot. The distribution of the measurement clusters and the corresponding MOD15A2H pixels can found in Figure 5.2. The agricultural lands were measured in 22-26 July, 2013 and mainly consist of corn, wheat, barley, grassland, rapeseeds, triticale and small areas of oat. Besides, grassland and corn were measured for three times (on 23 July, 11 August and 09 September, 2013 respectively). In this study, in situ LAI measurements are used for comparison with the LAI values derived from the model. Due to spatial resolution mismatch between the plot measurement and the 500m grid of the MODIS data, the measured LAI values were averaged for each corresponding pixel as in the MOD15A2H map. Therefore, 46 plots of forest were aggregated to 22 pixels and 195 plots of agricultural areas were averaged to 42 pixels. Afterwards, all the LAI measurements were directly compared with modelled LAI data on the same date. Due to the lack of climate observation data in 2014 and the relatively stable state of deciduous trees during fully leaf-off or leaf-on stages, we took the modelled data in 2013 to compare with the field LAI measurement in 2014.

5.4 Methodology

5.4.1 Model Development

In the local phenological model, the cumulative thermal summation has been successfully applied in monitoring the onset of greenness or budburst (Chuine et al., 2000a; Chuine et al., 2000b). The net effect of the vegetation growth and senescence can be depicted by the mathematical functions as the temporal profiles of the LAI dynamics (Koetz et al., 2005). The

phenological phases of the plants, such as the budburst, leaf development, flowering and leaf senescence differ according to the climate conditions and the vegetation types. The general structure of the phenological sigmoid model suppose that the probability of the emergence of a single leaf in day of year (DOY) is normally distributed, therefore the total amount of green cover through time is an accumulation, which is similar to the logistic growth curve (Zhang et al., 2003). In this sense, the annual leaf area of deciduous vegetation normally shows an exponential rise when the climate factors are satisfied and then reaches to the maximum during summer time. After the maturity period, the growth rate is modulated and dominated by the senescence. Then the leaf area declines until all the leaves fall down to the end. Whereas, the LAI of coniferous vegetation changes far less over the year.

A novel TPVM model is proposed in this study by integrating the observed daily mean air temperature and daily sum precipitation data (Equation 1). In TPVM, we assume that the annual course of the LAI is collaboratively affected by the temperature and precipitation, not solely by the temperature. Therefore, when the temperature and precipitation data cumulate to a certain level, the plant leaves start to emerge or disappear. The other two models of CSDM and DLM were also conducted for comparison. Instead of using DOY as input variables as most of the studies (Fisher et al., 2006), the cumulative temperature data were implemented in the DLM (Equation 2). In addition, the semi-mechanistic CSDM model defines the canopy growth and senescence using the cumulative air temperature data shown as Equation 3. The slight difference of the CSDM in this study with the original model is that we add an initial background parameter c to consist with the proposed TPVM.

The newly proposed TPVM can be derived by Equation 5.1:

$$LAI(T,P) = LAI_{Amp} \left(\frac{1}{1+e^{\alpha\left(\frac{Ti-T}{ri}\right)+(1-\alpha)\left(\frac{Pi-P}{ri}\right)}} - \frac{1}{1+e^{\alpha\left(\frac{Ts-T}{rs}\right)+(1-\alpha)\left(\frac{Ps-P}{rs}\right)}} \right) + c \qquad (5.1)$$

The DLM model follows the structure in TIMESAT (Jönsson and Eklundh, 2004) by Equation 5.2:

$$LAI(T) = LAI_{Amp} * \left(\frac{1}{1+e^{\left(\frac{Ti-T}{ri}\right)}} - \frac{1}{1+e^{\left(\frac{Ts-T}{rs}\right)}} \right) + c \tag{5.2}$$

The CSDM model can be calculated by Equation 5.3:

$$LAI(T) = LAI_{Amp} \left[\frac{1}{1+e^{-b(T-T_i)}} - e^{-a((T-T_s))} \right] + c \tag{5.3}$$

where, variable T is defined as the accumulated daily mean air temperature above 0°C, P represents the cumulative daily sum precipitation. b is the relative growth rate at the inflexion point expressed as the cumulative temperature Ti and a is the relative growth rate at the senescence point Ts. ri, rs are the rate of change at the flexion points during leaf-on and leaf-off period respectively. LAIAmp indicates the amplitude of maximal leaf area, and c is the initial background LAI value.

5.4.2 Optimization

Dynamically dimensioned search (DDS) proposed by Bryan A. Tolson (Tolson and Shoemaker, 2007) was adopted as the global optimization method in this study for the CSDM, DLM and TPVM models. The simple stochastic DDS algorithm is designed for finding the good global solutions based on heuristic global search algorithm. The only stopping criteria is the user-specified maximum evaluation limit. DDS searches globally from the beginning and becomes a more local search when iteration number approaches the defined maximum number of evaluations. In the DDS algorithm, the calibrating model parameters serve as the decision variables and the varying dimension is the changing number of the model parameter values. The number of dimensions in the neighborhood is dynamically and probabilistically reduced to a new search neighborhood and then the global search is adjusted to the local. The algorithm

randomly selects the dimensions for perturbations and generates the candidate solutions by perturbing the current solutions within the magnitudes randomly sampled from the standard normal distribution. The scalar neighborhood size perturbation parameter (r) in DDS is set to 0.2 in this study as recommended by the author (Tolson and Shoemaker, 2007). The DDS algorithm converges to the region of the global optimum instead of the precise global optimum. In this study, we firstly tested the maximum evaluation number of DDS evaluations for the TPVM model and then chose the parameter set with the minimum objective value from all the evaluation results as the optimal solution. More details about the DDS algorithm can be referred to the literature (Tolson and Shoemaker, 2007).

5.4.3 Objective Function and Error Measures

Root mean squared error (RMSE) and mean absolute error (MAE) were calculated for the model assessment, as followed in Equation 5.4 and Equation 5.5. The objective function in Equation 5.6 combines the RMSE with a weighted parameter *wi* to be minimized in the optimization procedure. The weighted method follows the idea in TIMESAT in order to simulate the results better fitting to the upper envelope of the times series of satellite data. The discontinuities of MODIS product may suffer from the contamination of clouds or failure of algorithm derivation (Kandasamy et al., 2013; Tian et al., 2002), which need to be filtered out firstly in the preprocessing of MODIS LAI data. The data points which suddenly decline during the growth stage, in other words, if the data points fall far below the predicted LAI are assumed to be less important. Besides larger weights are assigned to the points at the start and end time, as well as the higher values during the maturity period. In this study, we optimize the objective function with weight factors in two steps. Firstly, the weight parameter *wi* was set equally as 1 for each data point. Run the DDS for the objective function with the user-specified evaluation times. Secondly, calculate the predicted LAI data with the optimal parameters from the first step and compare the prediction with the remotely observed LAI. If the remotely observed LAI

is below the predicted LAI, the weight parameter value will be adjusted to higher value, which can be defined by the user with consideration of reality. With the new weight value, optimize the model again with DDS and the optimal parameter set will be the returned as the best solution.

$$RMSE = \sqrt[2]{\frac{\sum_{i=1}^{n}(f_i - y_i)^2}{n}} \tag{5.4}$$

$$MAE = \frac{1}{n}\sum_{i=1}^{n}|f_i - y_i| \tag{5.5}$$

$$Obj_{lai} = \sqrt[2]{\frac{\sum_{i=1}^{n}\left(\frac{f_i - y_i}{w_i}\right)^2}{n}} \tag{5.6}$$

Where, n is the size of the dataset, f_i and y_i are the predicted and the observed LAI at the point i of the dataset, respectively. w_i is the weighted parameter. And Obj_{lai} is the objective function for the DDS optimization.

5.5 Model Results and Evaluation

The models were tested in two different ways: LAI prediction based on individual pixels and based on averaged block mean values (BMV). The models and optimization procedures run similarly, except that the pixel-wise processing uses all the individual pixels in the Attert Catchment separately, whereas BMV method splits the whole catchment into several subareas and calculate the mean values of each block based on the land cover category. Here, we set the block number as six according to the maximum number and location of meteorological stations. BMV is designed to eliminate the large variances between the pixels of the same land cover type and to present the overall LAI characteristics of the seven land cover types for each block. The returned optimal parameters from the BMV can also provide useful starting parameter sets when process the catchment in the pixel-wise way. In the following sections, the temporal and

spatial pattern analysis between the original MODIS and the modelled LAI data, and the comparison with field measurements make use of the modelling results from the pixel-wise analysis. Whereas, the test of maximum evaluation number of DDS as well as the variance evaluation between the modelled results and the original MODIS data were conducted based on the BMV.

5.5.1 Maximum Evaluation Number Determination of DDS

As introduced in Section 3, the original MODIS data needs to be preprocessed, therefore firstly we should filter the MODIS LAI products with the mBISE method. Then implement the cumulative temperature and precipitation data into the CSDM, DLM and TPVM models and optimize the results by DDS method. As the important criteria in DDS, the suitable maximum evaluation number should be determined beforehand. This section gives an example of BLF in block 1 based on BMV. The only inputs when optimizing the model using DDS are the parameter range set and the maximum evaluation number. In order to find the optimal evaluation number in balancing the error metrics and the time cost, we tried to predict the LAI values of BLF using the TPVM model and calculated the RMSE and MAE data between the predicted LAI and the original MODIS data. The tested evaluation number ranges from 10 to 10000 with an increment of 90 for each step. For each maximum evaluation number test, the model runs ten times and Figure 5.3 displays the RMSE and MAE variation ranges. The blue points and error bars represent the mean values and variations, respectively. From Figure 5.3 (a) and Figure 5.3 (b), we can see that the RMSE and MAE decrease dramatically with the increase of the maximum evaluation number and shows stable variance ranges starting with a maximum evaluation number around 2000. Therefore, in this study, we set our evaluation number as 2500 for all the DDS runs.
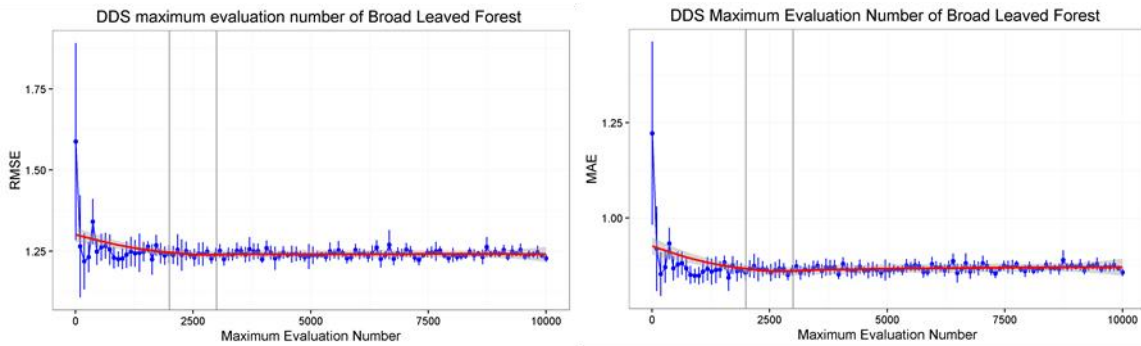
Figure 5.3 RMSE variances calculated from the modelled LAI of TPVM and MODIS LAI data for different evaluation numbers ranging from 10 to 10000.

5.5.2 Model Results

5.5.2.1 Temporal Pattern Analysis

Considering the majority of representative land cover types, we selected four main land cover types for the following evaluation, including the BLF, CCP, NIA and PAS. Figure 5.4 shows the modelling results of selected pixels for each land cover type. The red points indicate the meaningful points identified by the mBISE from the grey lines from the original MOD15A2H data. The cyan, green and red lines represent the modelling results of CSDM, DLM and TPVM respectively.

As shown in the Figure 5.4, MODIS data fluctuates frequently with several sudden falls in the time slices, resulting in confusion for the vegetation dynamics interpretation. It is clear to see that the mBISE method effectively labels the reasonable LAI points in the time series curves. The sudden decrease of data due to the atmospheric conditions or bidirectional reflectance distribution function effects (Atkinson et al., 2012) were avoided in most of the cases and the high value data with more significance over the growth season were well kept. This pre-processing step provided more continuous datasets compared to the original MODIS data and helped significantly in the following modelling process. The modelled LAI datasets are

generally produced with reasonable trajectories and effectively omitted the anomalous extreme values.

Especially for the BLF land cover, accompanied with the increase of cumulative temperature, the deciduous trees grow up with no leaf-on to the fast emergence of leaves during the green-up season. The three models retrieve very similar patterns at the start of the green-up season and then come to slight differences in the maximum amplitude of LAI among the three models during the maturity period. Besides, the model results also outline the small differences of leaf-off status during the senescence season in 2003, 2004, and 2013. The good performance of TPVM proves its good capability in predicting the continuous LAI for the BLF land cover type by combining both the temperature and precipitation data. The similarity of the modelling results of the three models probably reveal the dominance role of temperature on the BLF.

Dynamic patterns of the agricultural land cover types are more complicated than BLF. CCP and NIA in Attert Catchment generally are cultivated with wheat, barley or corn for one or two seasons. PAS includes the dense, predominantly graminoid grass cover for grazing. Some PAS fodder areas could be mechanically harvested several times during the growing season and this makes the PAS more fluctuating than the arable lands. Correspondingly, the identified points of CCP, NIA and PAS by mBISE contain several spurious spike points. The three models provide compatible LAI patterns for the NIA except that TPVM goes closer to the upper envelope. The LAI values of CCP and PAS were retrieved with higher variabilities among the three models and the obvious distinction existed in the wide curves during maturity time from CSDM. When including the precipitation data in TPVM, the modelled LAI values of NIA and PAS tend to respond more closely to the original MODIS data than the results of CSDM and DLM only using the temperature data. Considering the selected pixel of CCP in the present study, all of the three models underestimate the right half part of the leaf-off seasons from 2003 to 2013. The phenomenon may result from the data limitation of in situ cultivation seasons, as well as the mixture of small parcels of diverse annual crops, pasture or permanent crops.

Specification of season numbers for CCP or finer classified remotely sensed images with higher spatial resolution probably could improve the modelling results.
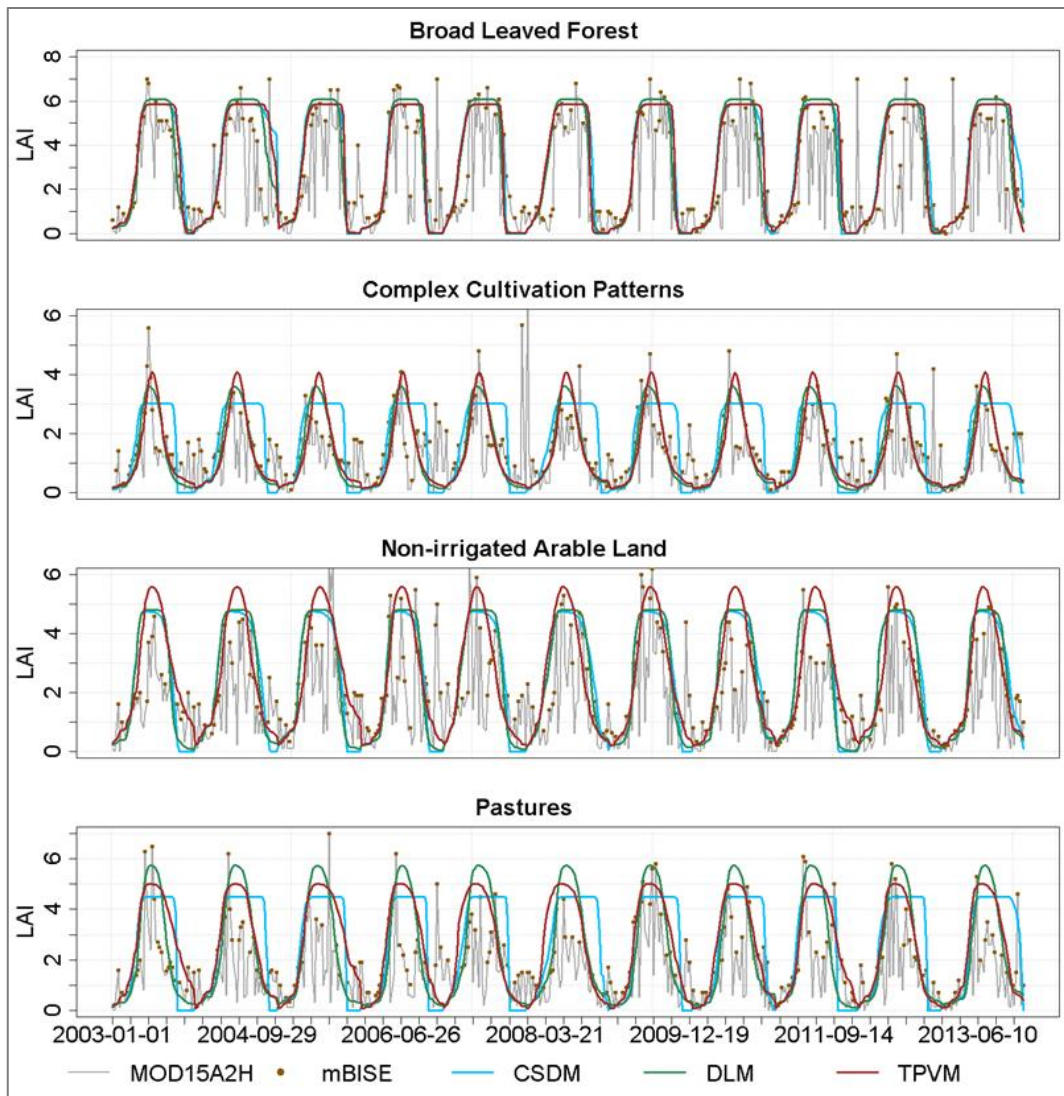
Figure 5.4 The time series of LAI data from 2003 to 2013 for four land covers (BLF, CCP, NIA, PAS) were from the original MOD15A2H (grey lines), mBISE (red points), CSDM (cyan lines), DLM (green lines) and TPVM (red lines) respectively.

5.5.2.2 Spatial Pattern Analysis

As mentioned in Section 3, pixel-wise modelling with the three models were implemented for each pixel from 2003 to 2013. Figure 5.5 presents the time series of LAI data for the Attert

Catchment on 23 July, 2013 from the original MOD15A2H, CSDM, DLM, TPVM respectively. The MODIS LAI data indicated large amounts of low values in the agricultural areas and small proportions of the forest area in the south of Attert Catchment. Based on our field observation, such large amount of low values in the forest and agricultural areas from MODIS data were unreasonable. Consistent with the pixel examples in the above analysis, the three models performed quite well for BLF but produced large variabilities in the agricultural areas. CSDM retrieved similar overall LAI patterns as the MODIS data, with large part of lower LAI values in the agricultural areas. Besides, a few pixels in the agricultural and forest area from TPVM got relatively lower values compared with the DLM. In general, DLM and TPVM obtained comparable manner for the whole catchment. This high uncertainty of the original MODIS data was significantly reduced by the DLM and TPVM.
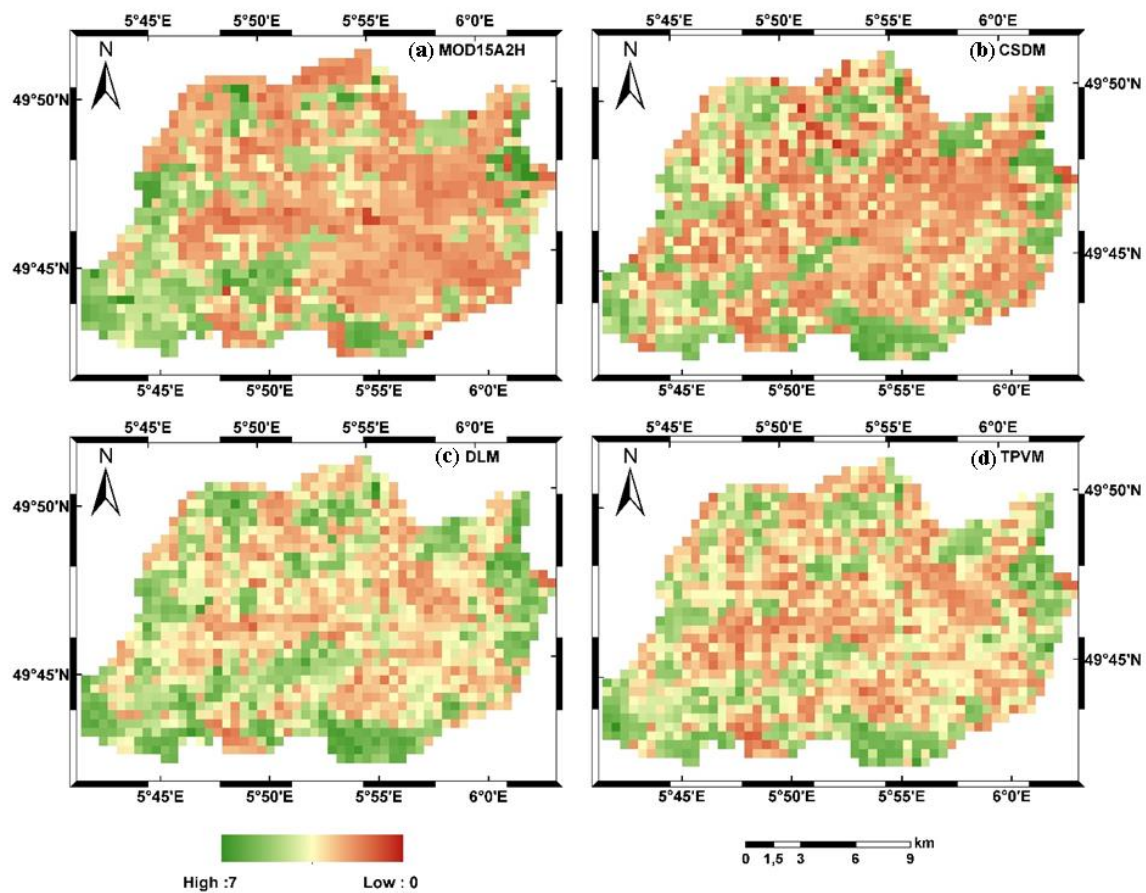
Figure 5.5 The LAI images of Attert Catchment on 28 July, 2013 were respectively derived from (a) MOD15A2H; (b) CSDM; (c) DLM; (d) TPVM.

5.5.3 Uncertainty Assessment

5.5.3.1 Error Metrics Evaluation

In this section, based on the idea of BMV method, the MODIS LAI values were firstly averaged for the seven land cover types in each block and then were used as the original observation data for error evaluation. RMSE and MAE data were calculated between the three modelled results and the MODIS LAI data based on BMV. Figure 5.6 provides the RMSE and MAE ranges of the seven land cover types in the six blocks. Moreover, Table 5-1 lists the mean RMSE and mean MAE of all the blocks. Considering all the land cover types, DLM and TPVM provide

slightly lower RMSE and MAE data compared to the results of CSDM. The average RMSE and MAE of DLM and TPVM is about 0.1 lower than the data of CSDM. This is more obvious for the CCP and NIA with overall lower RMSE and MAE than other land cover types. Whereas, CF always got the worst error data, this may be caused by two reasons. Firstly, the MODIS LAI products are weakly sensitive to the dense canopies such as the needle-leaved coniferous forest because of the reflectance saturation effect. When the LAI is larger than 4, the saturation frequency increases dramatically, that is to say with increasing LAI value, the accuracy of the retrieval decreases (Y. Knyazikhin, 1999). Secondly, the characteristic of coniferous forest determines that their LAI values do not change too much over the year, therefore the logistic model may not be the perfect option for the dynamics modelling. All in all, for most of the land cover types, only comparing the derivation of RMSE and MAE, TPVM incorporating the temperature and precipitation data reconstructed the continuous LAI values with similar or even lower variances compared to the other two models only using the temperature data.
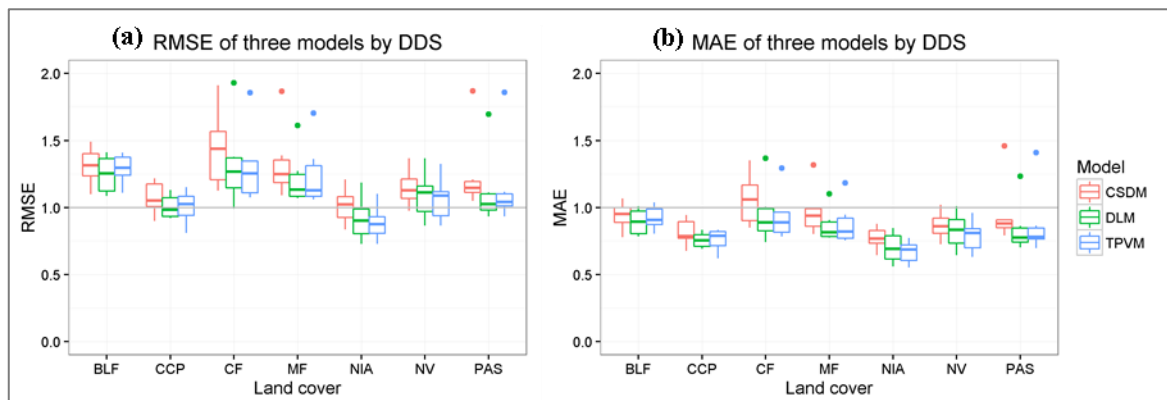
Figure 5.6 The variance data calculated between the MODIS LAI and the modelled LAI data using the three models (CSDM, DLM, TPVM) from an example block: (a) RME for the seven land cover types; (b) MAE for the seven land cover types.

Table 5-1 The averaged RMSE and MAE data calculated between the MODIS LAI and the modelled LAI data using the three models (CSDM, DLM, TPVM).

Land	RMSE			MAE		
Cover	CSDM	DLM	TPVM	CSDM	DLM	TPVM
BLF	1.31	1.25	1.29	0.94	0.89	0.92
CCP	1.07	1.01	1.01	0.81	0.76	0.76
CF	1.44	1.33	1.31	1.06	0.95	0.94
MF	1.34	1.22	1.24	0.97	0.87	0.88
NIA	1.01	0.92	0.89	0.77	0.70	0.67
NV	1.15	1.09	1.06	0.87	0.83	0.79
PAS	1.25	1.13	1.17	0.96	0.85	0.88

5.5.3.2 Comparison with Field Measurement

As mentioned in Section 5.3.4, the measured LAI in the plot size (20m×20m) were aggregated to the pixel size of MOD15A2H (500m×500m). The LAI values of all the plots located in the pixel were averaged as the reference data for each corresponding pixel. Besides, 15 plots were measured in continuous time scales, and the aggregation was implemented for each measured date. In total, 42 pixels of the agricultural area and 22 pixels of the forest were utilized for comparison with the model results.

Figure 5.7 illustrates the comparison between the measured LAI and the original MOD15A2H LAI, and the predicted LAI from the three models. The original MOD15A2H product contains huge uncertainties comparing with the measured LAI and their Person's correlation coefficient (CC) is only 0.14 with RMSE of 2.19 and MAE of 1.69. The modelled results were improved significantly. The CC varies from 0.69 to 0.73 for the CSDM and DLM, and TPVM derives the best CC of 0.78 with the lowest RMSE of 0.99 and MAE of 0.84.
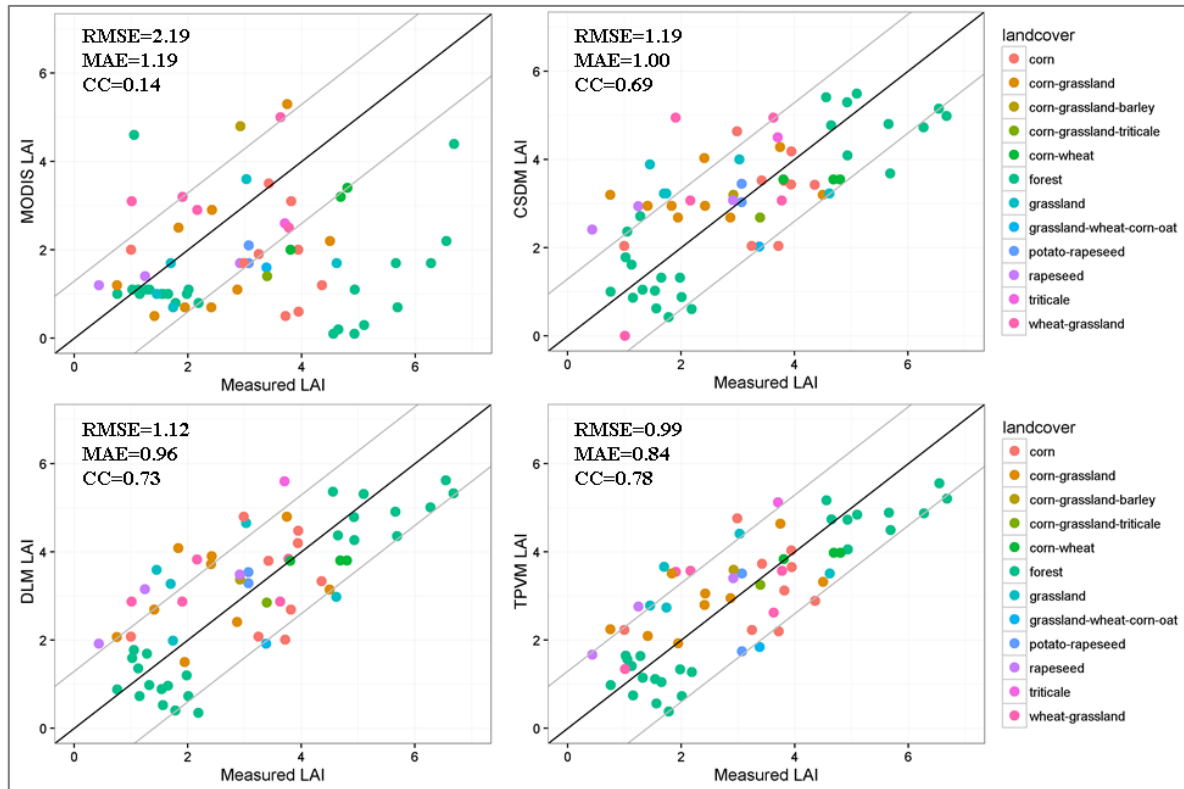
Figure 5.7 Comparison scatterplots between the measured LAI and the LAI data from MOD15A2H, CSDM, DLM and TPVM, respectively. The dark line indicates the 1:1 line and the two grey lines represent the lines with intercept of 1 and -1. The colored points represent the different land covers according to the legend.

The heterogeneous features of the mixed crops, the combination with the bare soil may increase the discrepancy between the measured LAI and the remotely sensed LAI or the modelled LAI. Therefore, when the measurement plots could not totally occupy the MODIS pixel, their averaged LAI value may still have difficulties in representing all the features of the corresponding pixel. In July 2013, the corn fields were cultivated for about one month. Whereas, most of the wheat, barley and rapeseeds maturated readily for harvest. The forage grasslands were cultivated and harvested in turn during the time series of LAI measurements. Aside from those uncertainties, based on the scatterplots the modelled LAI of forest pixels in summer time fit very well with the measured LAI. DLM and TPVM achieved almost identical forest LAI in summer. Nevertheless, for most of the croplands, TPVM performed superior than

DLM and CSDM with more compatible data to the measured results. This could be easily explained by the reality that temperature predominantly affected the BLF but together with the precipitation exert significant influence on the agricultural land covers.

5.5.4 Phenological Metrics and Climate Controls Evaluation

With the increasing awareness of the phenology importance in the study of climate change, plant phenology combined with remotely sensed data have been frequently studied in the land surface modelling. Plant phenology interacts with the climate and varies with the climate zone, vegetation type and inter-annual variability of the start and end of the growing season (Richardson et al., 2013). The phenology metrics derived from the satellite data could serve as an indicator of climate change on the terrestrial ecosystems (Menzel and Fabian, 1999). According to the report of Reed (Reed et al., 1994) and the USGS description of remote sensing phenology metrics (USGS, 2013), in the present study, the start of season time (SOST), the end of season time (EOST), the time of maximum LAI value (MAXT), length of growing season (LOGS) were derived for the climate consequences evaluation. SOST and EOST indicate the start and end of measurable photosynthesis in the vegetation canopy, which normally are described as the day of year (DOY) having a consistent upward or downward trend in time series of LAI. Here, we calculated the SOST and EOST as the half-maximum-mid-point between minimum and maximum LAI. Therefore, based on the SOST and EOST, LOGS can be attained as the number of days during the growing season. MAXT represents the time of maximum photosynthesis in the canopy.

Representative pixels of BLF, CCP and NIA from Attert Catchment were chosen for the phenology analysis. Figure 5.8 delineates the phenological metrics in DOY of BLF and CCP from 2003 to 2013. Figure 5.8 (a-b) display the growing seasons of BLF and CCP in different colours ranked by the yearly total temperature from 2003 to 2013. The green points on each line represent the time when the leaves reach the maximum value during the maturity period.

The red line of BLF in Figure 5.8 (a) demonstrates that the highest cumulative temperature of 3978 °C in 2007 was accompanied with the early beginning of the growing season at DOY of 73. The differences of LOGS between BLF and CCP can also be clearly seen, with mean number of days of 175 and 186. This phenomenon further proves that the warming weather can advance the start of season in the spring especially for temperate deciduous forest. Moreover, the unusual warming weather can also speed up the maturity and shorten the growing season. For example, in 2003, known as the European heat wave year, LOGS was the shortest compared to other years. The accelerating effect became more obvious for the CCP with the LOGS of 122 compared to the 11-year mean LOGS of 135. Figure 5.8(c-d) demonstrate the influences of inter-annual temperature variabilities on the LAI values of BLF and CCP. The green, dark-green and red dash lines respectively were subdivided as the range of SOST, MAXT and EOST within the 11 years. Uniformly, the forest area exhibited more stable manners than the agricultural sites.
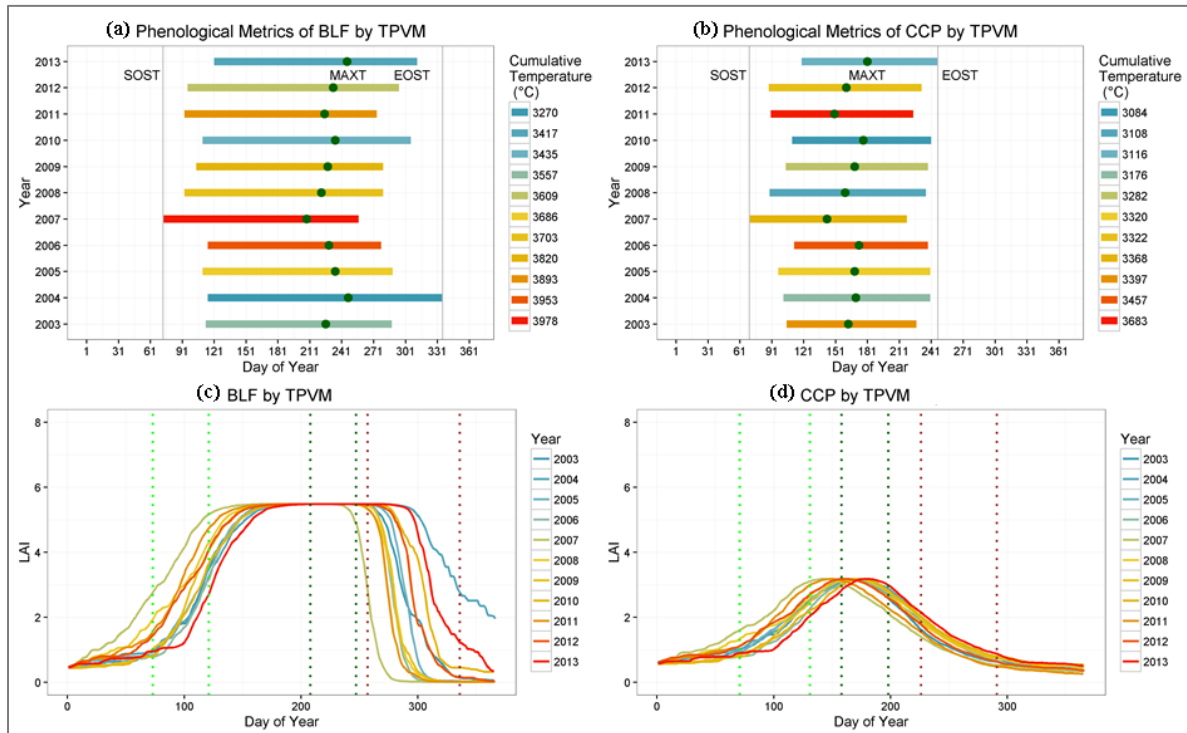
Figure 5.8 The growing season plots including the phenological metrics (SOST, MAXT, EOST) were derived from TPVM for two land covers: (a) broad-leaved forest (BLF); (b) complex cultivation patterns (CCP); (c) and (d) represent the LAI dynamics in terms of day of year (DOY) from 2003 to 2013 for BLF and CCP, respectively.

Regarding the relationship of temperature and precipitation changes on the SOST, MAXT and EOST, three exemplary pixels from BLF and NIA were plotted in Figure 5.9. SOST and EOST of BLF correlate tightly with the yearly cumulative temperature data, confirming that the higher temperature bringing the earlier SOST and EOST data for BLF. Although the temperature greatly influenced the NIA, CCP and PAS, there is no such clear relationship shown for the BLF. In the other aspect, the precipitation data accelerates the SOST and MAXT of the NIA land cover shown in Figure 5.9(c-d). The MAXT and SOST data calculated from TPVM for NIA verified that the crop growing would be delayed when no enough precipitation was available in the non-irrigated agricultural areas. Vice versa, the growth of crops could also be promoted in a certain degree with the increase of the total precipitation data. Moreover, the grey shaded area demonstrate that the higher standard derivation of SOST, MAXT and

precipitation from NIA compared to the BLF land cover. The large variabilities of NIA areas probably could partly explain this uncertainty, such as the various cultivated crops or multiple growth seasons, which influence the modelled LAI results and consequently modify the precision of the phenological metrics.
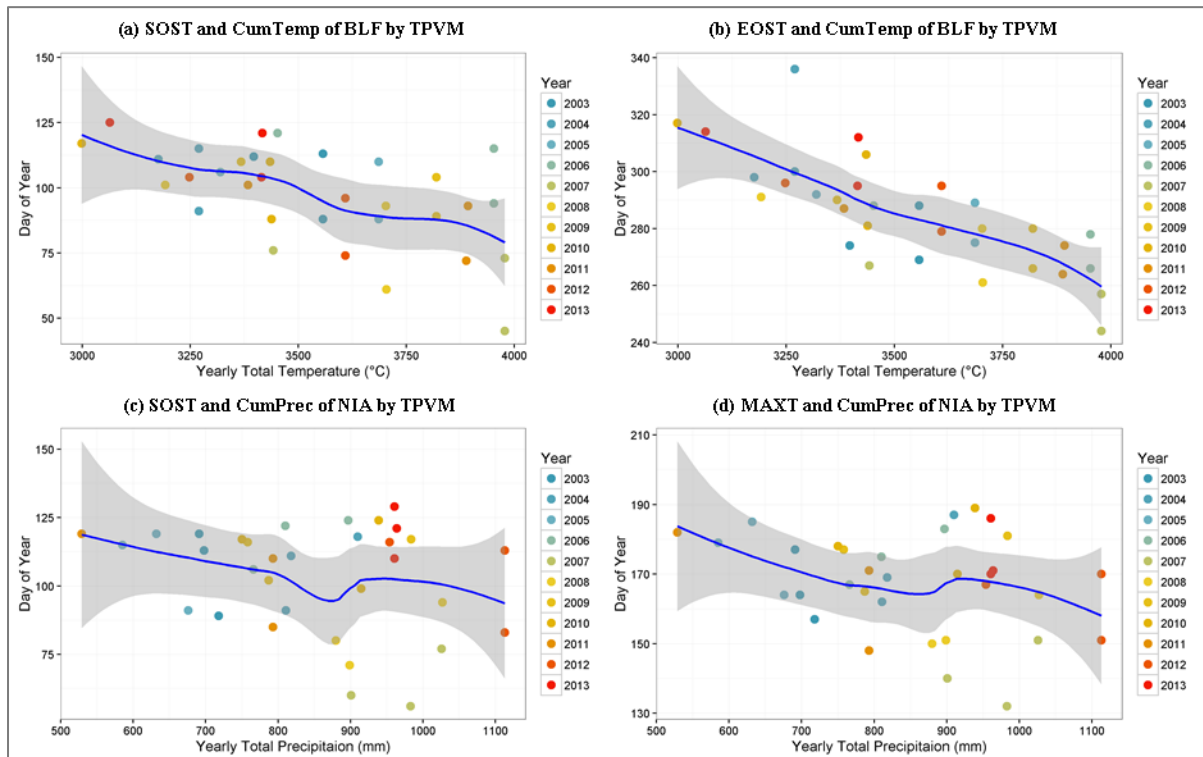
Figure 5.9 Climate variables relationship with the phenological metrics from 2003 to 2013 were plotted respectively: (a) the relationship of SOST from BLF by TPVM and yearly cumulative temperature; (b) the relationship of EOST from BLF by TPVM and yearly cumulative temperature; (c) the relationship of SOST from NIA by TPVM and yearly cumulative precipitation; (d) the relationship of MAXT from NIA by TPVM and yearly cumulative precipitation.

5.6   Conclusions

By integrating the climate data and remotely sensed data, a new vegetation dynamics model TPVM was proposed in this study. TPVM takes the observed cumulative daily mean temperature and cumulative daily sum precipitation data as input variables, and optimizes the

results by DDS to the filtered MODIS LAI dataset. Besides TPVM, CSDM and DLM models with the single input of cumulative temperature data were also implemented for comparison. TPVM derives comparable continuous LAI predictions for the deciduous forest area and superior data for the agricultural areas compared to the models solely depending on the temperature data.

The preprocessing of MODIS data by mBISE method produced more continuous datasets by eliminating the spurious spikes, which significantly improved the data quality of original MODIS product. Besides that, the weighted scheme also provided great assistance in the LAI prediction through the optimization procedure. Comparing the three models based on the BMV data, both, the temporal and spatial pattern evaluations demonstrate that the three models work quite well for the BLF forest, but have large discrepancies over the agricultural areas. The variances of RMSE and MAE for the seven land covers prove that most of the TPVM predictions retrieve the continuous LAI data with lower uncertainties than those of DLM and CSDM. In respect to the different land cover types, the overall patterns of DLM and TPVM are more realistic and continuous compared to the CSDM. Furthermore, comparing to the field measured LAI, all the three models retrieved more realistic LAI data than the original MODIS data indicated by the raise of the lowest CC of 0.14 to a higher level (ranging from 0.69 to 0.78). Nevertheless, TPVM manifested the superiority over the prediction of the agricultural fields with the overall CC of 0.78.

Moreover, the phenological metrics including the SOST, EOST, MAXT and LOGS were derived from the time series of LAI values predicted by TPVM from 2003 to 2013. Consistent with the previous research (Menzel and Fabian, 1999), the SOST and EOST of BLF advanced with the warming temperature. The LOGS of exampled CCP shortened due to the higher temperature and less precipitation such as in the Europe heat wave year of 2003. Besides that, the precipitation data exert more influences on the NIA, indicating with relatively early SOST and MAXT when more precipitation were available.

The main advantage of the TPVM model is its simplicity in predicting the dynamic LAI data with the climate observation data. In the study, we only applied the model in the meso-scale Attert Catchment, which has modest climate variabilities over the whole catchment. For future studies, we would recommend the implementation of the TPVM model in a larger and more heterogeneous catchment to test its applicability. Furthermore, in the larger-scale terrestrial ecosystem, the vegetation dynamic and the climate changes interact far more complicatedly. Other climate factors such as the photoperiod, soil moisture, soil temperature or topographic factors could also significantly affect the vegetation dynamics in different ways. Therefore, the integration with more climate controls, more meteorological observations, and finer spatial-resolution remotely sensed data could further mitigate the uncertain predictions in the vegetation dynamics modelling.

6   Conclusions and Outlook

This thesis aims at improving the capability of remote sensing techniques to retrieve land surface properties. Two essential parts of the land surface characteristics were investigated including the land cover categorization and vegetation dynamics modelling. On the one hand, the potential of TIR for improving land cover classification, on the other hand, a new vegetation dynamic model was proposed by integrating the climate variables and the satellite data for the temporal LAI prediction.

For the comprehensive evaluation of the effectiveness of TIR data, the key aspects influencing the classification results include the choice of data sources, the selection of classification algorithms and the error evaluation methods. Landsat images were classified into three-level categorization by the k-NN and RF algorithms using single-date and time series of images. Two cross validation methods based on the pixel and polygon level were evaluated for the uncertainty assessment. Considering all the evaluation results by using the two CV methods, it can be pointed out that the inclusion of the TIR data improves the land cover classification compared to the results only using the VIS/NIR bands.

Accuracy data from the single-date Landsat 8 image proved that the TIR data clearly improved the classification results especially for Level 2 and Level 3 categories when incorporating the two thermal bands with the VIS/NIR bands. The time series of Landsat images retrieved varying accuracy data by the pixel-based CV and polygon-based CV methods. For Level 1 and Level 2 category evaluated by pixel-based CV method, adding the TIR band or only using the time series of TIR bands, the accuracy data were comparable or even higher than the results from VIS/NIR data. Whereas based on the polygon-based CV method, the accuracy declined greatly when only using the time series of TIR bands for Level 2 category classification. The discrepancies between the two CV methods are mainly caused by the pixel correlation when resampling the TIR band from coarse spatial resolution to the fine resolution as the VIS/NIR

bands. In general, the pixel-based CV method showed clear weaknesses when sampling the pixels from the resampled TIR data. As complement, the polygon-based CV method substantially alleviate the correlation problem of the resampled pixels by using the independent polygons. For future studies using the resampled satellite images in land cover classification, the polygon-based method is preferred when using the CV method for training and validating. Nevertheless, in spite of the evaluation discrepancy, the land cover types could be better interpreted by incorporating the TIR data. Therefore, the TIR data is recommended in combination with the VIS/NIR information for the future investigation of land cover categorization.

Due to the limitation of Landsat images and relatively stable condition of the study area, our work still needs to be examined when applying to large-scale or rapidly-changing catchment. The time series of remote sensing data, if possible at least two images from the winter or summer seasons, could be very helpful for the agricultural land cover classification. Additionally, with the growing interest of TIR application in eco-hydrological system, more advanced TIR data from other satellite platforms (e.g. ASTER) or hyperspectral TIR sensors onboard drones have better possibility to extract the land surface properties. The further significant progress in LST retrieval from multispectral satellite data has been very slow and requires innovative fusion methods to integrate the multiple bands of multispectral and multi-temporal TIR data from the current and new satellites (Li et al., 2013). Data fusion methods such as the wavelet transform (Wu et al., 2015) or data mining sharpener (Gao et al., 2012) could also be applied for the TIR data.

 Regarding to the uncertainty evaluation, the land cover classification process needs to be carefully managed when using the resampled TIR data. The correlation issue when using the pixel-based CV methods should be noted. Actually, if the TIR data has the higher spatial resolution and does not need to be resampled, the pixel-based CV method can still be used. However, in the case similar to the present work, the polygon-based CV method would be more

suitable to avoid the correlation effect. Alternatively, other sampling methods such as the random sampling method possibly could also be helpful to avoid this problem (Foody et al., 2006). The random sampling method generates the training or validating samples randomly over the study area and undoubtedly requires more efforts for the ground truth data collection. Although the random sampling method is considered to be more subjective, the applicability in the large-scale catchment should be further examined. All in all, further study using the resampled TIR data is recommended to determine the appropriate evaluation method according to the features of three sampling methods and in consideration of the data sources as well as the possibility of large ground truth data validation.

The vegetation dynamics modelling study focused on integrating the climate controls into the newly proposed TPVM model. The assumption of the model origins from the characteristics of the deciduous canopies, which follows the logistic functions and uses the cumulative temperature and precipitation data as variables. After the preprocessing by the mBISE method, the noises caused by the cloud contamination or system errors have been well filtered. The 11-year MODIS LAI data were utilized as the reference data for the model optimized by the DDS method. Together with the TPVM, two vegetation dynamics models solely based on the cumulative temperature data were also used for the performance evaluation. For the uncertainty analysis, both, the mean block values and the pixel-based value evaluation were conducted to compare with the mean original MODIS data and the field measured LAI data respectively.

The results indicated that the TPVM model can achieve better LAI values when compared with two temperature-dependent models (DLM and CSDM), especially for the agricultural land cover types. In Attert catchment, the deciduous forest is proved to be dominated by the temperature control. Whereas, the agricultural areas including the non-irrigated arable land or complex cultivation patterns are coherently affected by the temperature and precipitation conditions. The phenological metrics derived from the proposed model also demonstrate that the warm spring could advance the start season of the beech forest. Besides, the precipitation

effect on the agricultural area is obviously shown as early start season and early crop mature time.

The uncertainty evaluation between the model results and the field measured LAI data demonstrate that TPVM obtained the best modelled LAI data compared to the original MODIS LAI product and the results of DLM and CSDM. It is not surprising to see that TPVM predicted the deciduous forest with the highest accuracy. The good capability and simplicity of the proposed model provide a robust way to predict the temporal LAI values of different vegetation covers and also promote the progress of interaction study between the climate changes and the vegetation dynamics. In fact, instead of the year-to-year constant LAI values in most of the eco-hydrological models, the dynamic LAI values predicted by the TPVM model could represent more reliable vegetation dynamics properties, therefore, quantify the energy or water processes accurately. Besides, the climate-variable based TPVM model has the necessity to be compared with the complex photosynthesis models. The further integration of TPVM into the hydrological model also need to be tested. For instance, the dynamic variation of the LAI values can be utilized for interception calculation in the hydrological process, as well as the corresponding influences could be simulated by the hydrological models.

In future studies, the proposed TPVM model should be further investigated in the large-scale catchment with more heterogeneous landscape. Not only the land cover types but also the varying topography conditions need to be considered. The elevation in Attert Catchment ranges from 220m to 550m, which has relatively homogenous temperature patterns of the same land cover type over the catchment. However, this may not fit to other large-scale catchment with diverse topography conditions, for example the Mur Catchment in Austria. Firstly, the temperature data should be generated with more meteorological observations by taking the lapse rate into account. Secondly, the precipitation with higher variability over the catchment needs to be further improved in the TPVM model. Moreover, additional meteorological and soil variables should be evaluated and integrated in the model. For example, topographical

controls such as the elevation or aspect, the photoperiod, soil moisture, soil temperature may alter the patterns of the vegetation dynamic in the large-scale catchment.

Furthermore, the TPVM model works quite well for the deciduous canopies while is constraint to the coniferous canopies. The interaction between the climate and the coniferous forest may be more stable compared to the deciduous forests. Using other functions to simulate the LAI changes of the coniferous forest would be more suitable. Existing studies have tried to describe the dynamics of coniferous forest by the polynomial functions or various empirical functions using the satellite vegetation index data (Pettorelli et al., 2005). Considering the agricultural land covers especially the croplands, it would be helpful to determine the growing season beforehand. Due to the lack of cultivation data, the present study is limited in the assumption of one growing season. This could be improved with the statistical data from the local farmers or identified using the multi-temporal remote sensing images. Nevertheless, further studies need more efforts to improve the model to fit different land covers by fully exploiting the characteristic of the vegetation growth.

The last but not least important thing for both, the land cover classification and the vegetation dynamics modelling is to improve the quality of the satellite products. The importance of the preprocessing for the satellite data has been emphasized repeatedly. No matter for the 30m Landsat images or the 500m MODIS LAI products, the preprocessing should always be done before further application. Therefore, in a future study, before any further investigation, more precise atmospheric correction methods and noise filtering algorithms could be evaluated in order to improve the accuracy of satellite data in deriving the land surface properties.

Bibliography

AghaKouchak, A., A. Farahmand, F. S. Melton, J. Teixeira, M. C. Anderson, B. D. Wardlow & C. R. Hain (2015) Remote sensing of drought: Progress, challenges and opportunities. *Reviews of Geophysics,* 53**,** 452-480.

Almeida-Filho, R. & Y. E. Shimabukuro (2002) Digital processing of a Landsat-TM time series for mapping and monitoring degraded areas caused by independent gold miners, Roraima State, Brazilian Amazon. *Remote Sensing of Environment,* 79**,** 42-50.

Amorós-López, J., L. Gómez-Chova, L. Alonso, L. Guanter, R. Zurita-Milla, J. Moreno & G. Camps-Valls (2013) Multitemporal fusion of Landsat/TM and ENVISAT/MERIS for crop monitoring. *International Journal of Applied Earth Observation and Geoinformation,* 23**,** 132-141.

Anderson, G. 2005. Encyclopedia of hydrological sciences. J. Wiley.

Anderson, J. R. 1976. A Land Use and Land Cover Classification System for Use with Remote Sensor Data. U.S. Government Printing Office.

Arora, V. (2002) MODELING VEGETATION AS A DYNAMIC COMPONENT IN SOIL-VEGETATION-ATMOSPHERE TRANSFER SCHEMES AND HYDROLOGICAL MODELS. *Reviews of Geophysics,* 40**,** 3-1-3-26.

Atkinson, P. M., C. Jeganathan, J. Dash & C. Atzberger (2012) Inter-comparison of four models for smoothing satellite sensor time-series data to estimate vegetation phenology. *Remote Sensing of Environment,* 123**,** 400-417.

Atzberger, C., A. Klisch, M. Mattiuzzi & F. Vuolo (2013) Phenological Metrics Derived over the European Continent from NDVI3g Data and MODIS Time Series. *Remote Sensing,* 6**,** 257.

Atzberger, C., K. Richter, F. Vuolo, R. Darvishzadeh & M. Schlerf. 2011. Why confining to vegetation indices? Exploiting the potential of improved spectral observations using radiative transfer models. In *SPIE Remote Sensing*, 81740Q-81740Q-16. International Society for Optics and Photonics.

Bagan, H., J. Ma, Q. Li, Z. Liu & X. Han. 2003. Use of wavelet high-frequency substitution fusion to increase remote sensing image spatial resolution. 376-379.

Ban, Y. (2003) Synergy of multitemporal ERS-1 SAR and Landsat TM data for classification of agricultural crops. *Canadian Journal of Remote Sensing,* 29**,** 518-526.

Baret, F. & R. Vintila. 2003. Satellite derived leaf area index derived from SOPT time series in the ADAM project. In *Geoscience and Remote Sensing Symposium, 2003. IGARSS '03. Proceedings. 2003 IEEE International*, 155-157 vol.1.

Bastiaanssen, W. G. M., M. Menenti, R. A. Feddes & A. A. M. Holtslag (1998) A remote sensing surface energy balance algorithm for land (SEBAL). 1. Formulation. *Journal of Hydrology,* 212–213**,** 198-212.

Beck, P. S. A., C. Atzberger, K. A. Høgda, B. Johansen & A. K. Skidmore (2006) Improved monitoring of vegetation dynamics at very high latitudes: A new method using MODIS NDVI. *Remote Sensing of Environment,* 100**,** 321-334.

Berk, A., L. S. Bernstein, G. P. Anderson, P. K. Acharya, D. C. Robertson, J. H. Chetwynd & S. M. Adler-Golden (1998) MODTRAN Cloud and Multiple Scattering Upgrades with Application to AVIRIS. *Remote Sensing of Environment,* 65**,** 367-375.

Bischof, H., W. Schneider & A. J. Pinz (1992) Multispectral classification of Landsat-images using neural networks. *Geoscience and Remote Sensing, IEEE Transactions on,* 30**,** 482-490.

Bounoua, L., R. DeFries, G. J. Collatz, P. Sellers & H. Khan (2002) Effects of Land Cover Conversion on Surface Climate. *Climatic Change,* 52**,** 29-64.

Bradley, B. A., R. W. Jacob, J. F. Hermance & J. F. Mustard (2007) A curve fitting procedure to derive inter-annual phenologies from time series of noisy satellite NDVI data. *Remote Sensing of Environment,* 106**,** 137-145.

Breiman, L. (2001) Random Forests. *Machine Learning,* 45**,** 5-32.

Brown, J. C., J. H. Kastens, A. C. Coutinho, D. d. C. Victoria & C. R. Bishop (2013) Classifying multiyear agricultural land use data from Mato Grosso using time-series MODIS vegetation index data. *Remote Sensing of Environment,* 130**,** 39-50.

Brown, M. E., D. J. Lary, A. Vrieling, D. Stathakis & H. Mussa (2008) Neural networks as a tool for constructing continuous NDVI time series from AVHRR and MODIS. *International Journal of Remote Sensing,* 29**,** 7141-7158.

Byrne, G. F., P. F. Crapper & K. K. Mayo (1980) Monitoring land-cover change by principal component analysis of multitemporal landsat data. *Remote Sensing of Environment,* 10**,** 175-184.

CAOS. 2012. CAOS: From Catchments as Organised Systems to Models based on Functional Units. Kaiserstr. 12, Karlsruhe, Germany: KIT Karlsruhe Institute of Technology.

Carlson, T. N. & S. Traci Arthur (2000) The impact of land use — land cover changes due to urbanization on surface microclimate and hydrology: a satellite perspective. *Global and Planetary Change,* 25**,** 49-65.

Carrão, H., P. Gonçalves & M. Caetano (2008) Contribution of multispectral and multitemporal information from MODIS images to land cover classification. *Remote Sensing of Environment,* 112**,** 986-997.

Chandola, V., H. Dafeng, G. Lianhong, B. Bhaduri & R. R. Vatsavai. 2010. Using Time Series Segmentation for Deriving Vegetation Phenology Indices from MODIS NDVI Data. In *Data Mining Workshops (ICDMW), 2010 IEEE International Conference on*, 202-208.

Chen, D., Y. Li, H. Liu, H. Xu, W. Xiao, T. Luo, Z. Zhou & M. Lin (2010) Biomass and carbon dynamics of a tropical mountain rain forest in China. *Science China Life Sciences,* 53**,** 798-810.

Chuine, I. (2000) A Unified Model for Budburst of Trees. *Journal of Theoretical Biology,* 207**,** 337-347.

Chuine, I., J. Belmonte & A. Mignot (2000a) A modelling analysis of the genetic variation of phenology between tree populations. *Journal of Ecology,* 88**,** 561-570.

Chuine, I., G. Cambon & P. Comtois (2000b) Scaling phenology from the local to the regional level: advances from species-specific phenological models. *Global Change Biology,* 6**,** 943-952.

Chuine, I., P. Cour & D. D. Rousseau (1999) Selecting models to predict the timing of flowering of temperate trees: implications for tree phenology modelling. *Plant, Cell & Environment,* 22**,** 1-13.

Chuine, I., K. Kramer & H. Hänninen. 2003. Plant Development Models. In *Phenology: An Integrative Environmental Science,* ed. M. D. Schwartz, 217-235. Dordrecht: Springer Netherlands.

Chuine, I., P. Yiou, N. Viovy, B. Seguin, V. Daux & E. L. R. Ladurie (2004) Historical phenology: Grape ripening as a past climate indicator. *Nature,* 432**,** 289-290.

Churkina, G., S. W. Running, A. L. Schloss & T. P. O. F. T. P. N. M. Intercomparison (1999) Comparing global models of terrestrial net primary productivity (NPP): the importance of water availability. *Global Change Biology,* 5**,** 46-55.

Cihlar, J., R. Latifovic, J. Chen, J. Beaubien, Z. Li & S. Magnussen (2000) Selecting Representative High Resolution Sample Images for Land Cover Studies. Part 2: Application to Estimating Land Cover Composition. *Remote Sensing of Environment,* 72**,** 127-138.

Clausi, D. A. (2002) An analysis of co-occurrence texture statistics as a function of grey level quantization. *Canadian Journal of Remote Sensing,* 28**,** 45-62.

Claverie, M., V. Demarez, B. Duchemin, O. Hagolle, D. Ducrot, C. Marais-Sicre, J.-F. Dejoux, M. Huc, P. Keravec, P. Béziat, R. Fieuzal, E. Ceschia & G. Dedieu (2012) Maize and

sunflower biomass estimation in southwest France using high spatial and temporal resolution remote sensing data. *Remote Sensing of Environment,* 124**,** 844-857.

Cleland, E. E., I. Chuine, A. Menzel, H. A. Mooney & M. D. Schwartz (2007) Shifting plant phenology in response to global change. *Trends in Ecology & Evolution,* 22**,** 357-365.

Colditz, R. R., T. Wehrmann, M. Bachmann, K. Steinnocher, M. Schmidt, G. Strunz & S. Dech (2006) Influence of image fusion approaches on classification accuracy: a case study. *International Journal of Remote Sensing,* 27**,** 3311-3335.

Collins, M. J., C. Dymond & E. A. Johnson (2004) Mapping subalpine forest types using networks of nearest neighbour classifiers. *International Journal of Remote Sensing,* 25**,** 1701-1721.

Congalton, R. G. (1991) A review of assessing the accuracy of classifications of remotely sensed data. *Remote Sensing of Environment,* 37**,** 35-46.

Congalton, R. G. & K. Green. 2009. Assessing the Accuracy of Remotely Sensed Data: Principles and Practices. CRC Press/Taylor & Francis.

Corcoran, J., J. Knight & A. Gallant (2013) Influence of Multi-Source and Multi-Temporal Remotely Sensed and Ancillary Data on the Accuracy of Random Forest Classification of Wetlands in Northern Minnesota. *Remote Sensing,* 5**,** 3212-3238.

Cover, T. M. & P. E. Hart (1967) Nearest Neighbor Pattern Classification. *Ieee Transactions on Information Theory,* 13**,** 21.

Crocetto, N. & E. Tarantino (2009) A Class-Oriented Strategy for Features Extraction from Multidate ASTER Imagery. *Remote Sensing,* 1**,** 1171-1189.

D'Arrigo, R. D., R. K. Kaufmann, N. Davi, G. C. Jacoby, C. Laskowski, R. B. Myneni & P. Cherubini (2004) Thresholds for warming-induced growth decline at elevational tree line in the Yukon Territory, Canada. *Global Biogeochemical Cycles,* 18**,** n/a-n/a.

DAAC, N. L. 2009. ASTER Global DEM Sioux Falls, South Dakota: USGS/Earth Resources Observation and Science (EROS) Center.

MODIS. 2012. Leaf Area Index - Fraction of Photosynthetically Active Radiation 8-Day L4 Global 1km.Version 5. In *NASA EOSDIS Land Processes DAAC*. USGS Earth Resources Observation and Science (EROS) Center, Sioux Falls, South Dakota

de Beurs, K. M. & G. M. Henebry (2004) Land surface phenology, climatic variation, and institutional change: Analyzing agricultural land cover change in Kazakhstan. *Remote Sensing of Environment,* 89**,** 497-509.

Defries, R. S., M. C. Hansen & J. R. G. Townshend (2000) Global continuous fields of vegetation characteristics: A linear mixture model applied to multi-year 8 km AVHRR data. *International Journal of Remote Sensing,* 21**,** 1389-1414.

Deng, C. & C. Wu (2013) The use of single-date MODIS imagery for estimating large-scale urban impervious surface fraction with spectral mixture analysis and machine learning techniques. *ISPRS Journal of Photogrammetry and Remote Sensing,* 86**,** 100-110.

Dickinson, R. E. (1995) Land processes in climate models. *Remote Sensing of Environment,* 51**,** 27-38.

Didan, K. (2015) MOD13Q1 MODIS/Terra Vegetation Indices 16-Day L3 Global 250m SIN Grid V006. *NASA EOSDIS Land Processes DAAC*.

Dubayah, R. O., E. F. Wood, E. T. Engman, K. P. Czajkowski, M. Zion & J. Rhoads. 2000. Remote Sensing in Hydrological Modeling. In *Remote Sensing in Hydrology and Water Management,* eds. G. A. Schultz & E. T. Engman, 85-102. Berlin, Heidelberg: Springer Berlin Heidelberg.

Eamus, D. (2003) How does ecosystem water balance affect net primary productivity of woody ecosystems? *Functional Plant Biology,* 30**,** 187-205.

EEA. 2012. CORINE Land Cover. Germany: EuropeanEnvironment Agency.

Eisavi, V., S. Homayouni, A. Yazdi & A. Alimohammadi (2015) Land cover mapping based on random forest classification of multitemporal spectral and thermal images. *Environmental Monitoring and Assessment,* 187**,** 1-14.

Emberlin, J., J. Mullins, J. Corden, W. Millington, M. Brooke, M. Savage & S. Jones (1997) The trend to earlier birch pollen seasons in the U.K.: A biotic response to changes in weather conditions? *Grana,* 36**,** 29-33.

Evrendilek, F. & O. Gulbeyaz (2008) Deriving Vegetation Dynamics of Natural Terrestrial Ecosystems from MODIS NDVI/EVI Data over Turkey. *Sensors,* 8**,** 5270.

Fang, H., S. Liang & A. Kuusk (2003) Retrieving leaf area index using a genetic algorithm with a canopy radiative transfer model. *Remote Sensing of Environment,* 85**,** 257-270.

Feng, G., J. Masek, M. Schwaller & F. Hall (2006) On the blending of the Landsat and MODIS surface reflectance: predicting daily Landsat surface reflectance. *Geoscience and Remote Sensing, IEEE Transactions on,* 44**,** 2207-2218.

Feng, G., J. T. Morisette, R. E. Wolfe, G. Ederer, J. Pedelty, E. Masuoka, R. Myneni, B. Tan & J. Nightingale (2008) An Algorithm to Produce Temporally and Spatially Continuous MODIS-LAI Time Series. *Geoscience and Remote Sensing Letters, IEEE,* 5**,** 60-64.

Fisher, J. I., J. F. Mustard & M. A. Vadeboncoeur (2006) Green leaf phenology at Landsat resolution: Scaling from the field to the satellite. *Remote Sensing of Environment,* 100**,** 265-279.

Foody, G. M. (1996) Approaches for the production and evaluation of fuzzy land cover classifications from remotely-sensed data. *International Journal of Remote Sensing,* 17**,** 1317-1340.

Foody, G. M. (2002) Status of land cover classification accuracy assessment. *Remote Sensing of Environment,* 80**,** 185-201.

Foody, G. M., A. Mathur, C. Sanchez-Hernandez & D. S. Boyd (2006) Training set size requirements for the classification of a specific class. *Remote Sensing of Environment,* 104**,** 1-14.

Forrest, J. & A. J. Miller-Rushing (2010) Toward a synthetic understanding of the role of phenology in ecology and evolution. *Philosophical Transactions of the Royal Society of London B: Biological Sciences,* 365**,** 3101-3112.

French, A. N., T. J. Schmugge, J. C. Ritchie, A. Hsu, F. Jacob & K. Ogawa (2008) Detecting land cover change at the Jornada Experimental Range, New Mexico with ASTER emissivities. *Remote Sensing of Environment,* 112**,** 1730-1748.

Friedl, M. A., D. K. McIver, J. C. F. Hodges, X. Y. Zhang, D. Muchoney, A. H. Strahler, C. E. Woodcock, S. Gopal, A. Schneider, A. Cooper, A. Baccini, F. Gao & C. Schaaf (2002) Global land cover mapping from MODIS: algorithms and early results. *Remote Sensing of Environment,* 83**,** 287-302.

Gao, F., W. Kustas & M. Anderson (2012) A Data Mining Approach for Sharpening Thermal Satellite Imagery over Land. *Remote Sensing,* 4**,** 3287-3319.

Geneletti, D. & B. G. H. Gorte (2003) A method for object-oriented land cover classification combining Landsat TM data and aerial photographs. *International Journal of Remote Sensing,* 24**,** 1273-1286.

Geosystem, E. L. 2013. ERDAS Imagine 2013. User Guide. Atlanta: ERDAS Inc.Geosystem.

Geosystems (2013) ATCOR for IMAGINE 2013. User Manual ATCOR 2 and ATCOR 3.

Giri, C., B. Pengra, J. Long & T. R. Loveland (2013) Next generation of global land cover characterization, mapping, and monitoring. *International Journal of Applied Earth Observation and Geoinformation,* 25**,** 30-37.

Gislason, P. O., J. A. Benediktsson & J. R. Sveinsson (2006) Random Forests for land cover classification. *Pattern Recognition Letters,* 27**,** 294-300.

Glenn, E., A. Huete, P. Nagler & S. Nelson (2008) Relationship Between Remotely-sensed Vegetation Indices, Canopy Attributes and Plant Physiological Processes: What Vegetation Indices Can and Cannot Tell Us About the Landscape. *Sensors,* 8**,** 2136.

Gómez, C., J. C. White & M. A. Wulder (2016) Optical remotely sensed time series data for land cover classification: A review. *ISPRS Journal of Photogrammetry and Remote Sensing,* 116**,** 55-72.

Gong, P., J. Wang, L. Yu, Y. Zhao, Y. Zhao, L. Liang, Z. Niu, X. Huang, H. Fu, S. Liu, C. Li, X. Li, W. Fu, C. Liu, Y. Xu, X. Wang, Q. Cheng, L. Hu, W. Yao, H. Zhang, P. Zhu, Z. Zhao, H. Zhang, Y. Zheng, L. Ji, Y. Zhang, H. Chen, A. Yan, J. Guo, L. Yu, L. Wang, X. Liu, T. Shi, M. Zhu, Y. Chen, G. Yang, P. Tang, B. Xu, C. Giri, N. Clinton, Z. Zhu, J. Chen & J. Chen (2012) Finer resolution observation and monitoring of global land cover: first mapping results with Landsat TM and ETM+ data. *International Journal of Remote Sensing,* 34**,** 2607-2654.

González-Sanpedro, M. C., T. Le Toan, J. Moreno, L. Kergoat & E. Rubio (2008) Seasonal variations of leaf area index of agricultural fields retrieved from Landsat data. *Remote Sensing of Environment,* 112**,** 810-824.

Goward, S. N. & S. D. Prince (1995) Transient Effects of Climate on Vegetation Dynamics: Satellite Observations. *Journal of Biogeography,* 22**,** 549-564.

Grier, C. C. & S. W. Running (1977) LEAF AREA OF MATURE NORTHWESTERN CONIFEROUS FORESTS - RELATION TO SITE WATER-BALANCE. *Ecology,* 58**,** 893-899.

Guerschman, J. P., J. M. Paruelo, C. D. Bella, M. C. Giallorenzi & F. Pacin (2003) Land cover classification in the Argentine Pampas using multi-temporal Landsat TM data. *International Journal of Remote Sensing,* 24**,** 3381-3402.

Hadjimitsis, D. G., C. R. I. Clayton & V. S. Hope (2004) An assessment of the effectiveness of atmospheric correction algorithms through the remote sensing of some reservoirs. *International Journal of Remote Sensing,* 25**,** 3651-3674.

Hansen, M. C. & S. J. Goetz. 2006. Land-Cover Classification and Change Detection. In *Encyclopedia of Hydrological Sciences*. John Wiley & Sons, Ltd.

Hartig, F., J. Dyke, T. Hickler, S. I. Higgins, R. B. O'Hara, S. Scheiter & A. Huth (2012) Connecting dynamic vegetation models to data – an inverse perspective. *Journal of Biogeography,* 39**,** 2240-2252.

Herold, M., J. S. Latham, A. Di Gregorio & C. C. Schmullius (2006) Evolving standards in land cover characterization. *Journal of Land Use Science,* 1**,** 157-168.

Hilker, T., A. I. Lyapustin, C. J. Tucker, P. J. Sellers, F. G. Hall & Y. Wang (2012) Remote sensing of tropical ecosystems: Atmospheric correction and cloud masking matter. *Remote Sensing of Environment,* 127**,** 370-384.

Holben, B. N. (1986) Characteristics of maximum-value composite images from temporal AVHRR data. *International Journal of Remote Sensing,* 7**,** 1417-1434.

Hord, R. M. 1982. Digital image processing of remotely sensed data. Elsevier.

Horn, J. & K. Schulz (2010) Post-processing analysis of MODIS leaf area index subsets. *Journal of Applied Remote Sensing,* 4.

Houborg, R., J. B. Fisher & A. K. Skidmore (2015) Advances in remote sensing of vegetation function and traits. *International Journal of Applied Earth Observation and Geoinformation,* 43**,** 1-6.

Houghton, R. A., J. I. House, J. Pongratz, G. R. van der Werf, R. S. DeFries, M. C. Hansen, C. Le Quéré & N. Ramankutty (2012) Carbon emissions from land use and land-cover change. *Biogeosciences,* 9**,** 5125-5142.

Huang, C., L. S. Davis & J. R. G. Townshend (2002) An assessment of support vector machines for land cover classification. *International Journal of Remote Sensing,* 23**,** 725-749.

Hwang, T., C. Song, P. V. Bolstad & L. E. Band (2011) Downscaling real-time vegetation dynamics by fusing multi-temporal MODIS and Landsat NDVI in topographically complex terrain. *Remote Sensing of Environment,* 115**,** 2499-2512.

Li-COR Inc., L.-C. 2010. LAI-2200 Plant Canopy Analyzer: Instruction Manual. In *LI-COR Inc.* Lincoln, Nebraska 68504, USA.

Jiang, B., S. Liang, J. Wang & Z. Xiao (2010) Modeling MODIS LAI time series using three statistical methods. *Remote Sensing of Environment,* 114**,** 1432-1444.

Jianwen, M. & H. Bagan (2005) Land-use classification using ASTER data and self-organized neutral networks. *International Journal of Applied Earth Observation and Geoinformation,* 7**,** 183-188.

Johnson, B. A. (2015) Scale issues related to the accuracy assessment of land use/land cover maps produced using multi-resolution data: Comments on "The Improvement of Land Cover Classification by Thermal Remote Sensing". Remote Sens. 2015, 7(7), 8368-8390. *Remote Sensing*.

Jonsson, P. & L. Eklundh (2002) Seasonality extraction by function fitting to time-series of satellite sensor data. *Geoscience and Remote Sensing, IEEE Transactions on,* 40**,** 1824-1832.

Jönsson, P. & L. Eklundh (2004) TIMESAT—a program for analyzing time-series of satellite sensor data. *Computers & Geosciences,* 30**,** 833-845.

Justice, C. O., J. R. G. Townshend, B. N. Holben & C. J. Tucker (1985) Analysis of the phenology of global vegetation using meteorological satellite data. *International Journal of Remote Sensing,* 6**,** 1271-1318.

Kandasamy, S., F. Baret, A. Verger, P. Neveux & M. Weiss (2013) A comparison of methods for smoothing and gap filling time series of remote sensing observations – application to MODIS LAI products. *Biogeosciences,* 10**,** 4055-4071.

Kathuroju, N., M. A. White, J. Symanzik, M. D. Schwartz, J. A. Powell & R. R. Nemani (2007) On the use of the advanced very high resolution radiometer for development of prognostic land surface phenology models. *Ecological Modelling,* 201**,** 144-156.

Kerr, J. T. & M. Ostrovsky (2003) From space to species: ecological applications for remote sensing. *Trends in Ecology & Evolution,* 18**,** 299-305.

Kimes, D. S., Y. Knyazikhin, J. L. Privette, A. A. Abuelgasim & F. Gao (2000) Inversion methods for physically‐based models. *Remote Sensing Reviews,* 18**,** 381-439.

Knyazikhin, Y., J. V. Martonchik, R. B. Myneni, D. J. Diner & S. W. Running (1998) Synergistic algorithm for estimating vegetation canopy leaf area index and fraction of absorbed photosynthetically active radiation from MODIS and MISR data. *Journal of Geophysical Research: Atmospheres,* 103**,** 32257-32275.

Koetz, B., F. Baret, H. Poilvé & J. Hill (2005) Use of coupled canopy structure dynamic and radiative transfer models to estimate biophysical canopy characteristics. *Remote Sensing of Environment,* 95**,** 115-124.

Kogan, F. N. (2001) Operational Space Technology for Global Vegetation Assessment. *Bulletin of the American Meteorological Society,* 82**,** 1949-1964.

Kohavi, R. 1995. A study of cross-validation and bootstrap for accuracy estimation and model selection. In *Proceedings of the 14th international joint conference on Artificial intelligence - Volume 2*, 1137-1143. Montreal, Quebec, Canada: Morgan Kaufmann Publishers Inc.

Kramer, K., I. Leinonen & D. Loustau (1999) The importance of phenology for the evaluation of impact of climate change on growth of boreal, temperate and Mediterranean forests ecosystems: an overview. *International Journal of Biometeorology,* 44**,** 67-75.

Krishnaswamy, J., R. John & S. Joseph (2014) Consistent response of vegetation dynamics to recent climate change in tropical mountain regions. *Global Change Biology,* 20**,** 203-215.

Kustas, W. & M. Anderson (2009) Advances in thermal infrared remote sensing for land surface modeling. *Agricultural and Forest Meteorology,* 149**,** 2071-2081.

Lambin, E. F., H. J. Geist & E. Lepers (2003) DYNAMICS OF LAND-USE AND LAND-COVER CHANGE IN TROPICAL REGIONS. *Annual Review of Environment and Resources,* 28**,** 205-241.

Langley, S. K., H. M. Cheshire & K. S. Humes (2001) A comparison of single date and multitemporal satellite image classifications in a semi-arid grassland. *Journal of Arid Environments,* 49**,** 401-411.

Leith, H. (1974) Phenology and seasonal modeling. *Ecological Studies,* 8.

Li, C., J. Wang, L. Wang, L. Hu & P. Gong (2014) Comparison of Classification Algorithms and Training Sample Sizes in Urban Land Classification with Landsat Thematic Mapper Imagery. *Remote Sensing,* 6**,** 964-983.

Li, Z.-L., B.-H. Tang, H. Wu, H. Ren, G. Yan, Z. Wan, I. F. Trigo & J. A. Sobrino (2013) Satellite-derived land surface temperature: Current status and perspectives. *Remote Sensing of Environment,* 131**,** 14-37.

Liang, L. & M. Schwartz (2009) Landscape phenology: an integrative approach to seasonal vegetation dynamics. *Landscape Ecology,* 24**,** 465-472.

Liang, S. 2008. Advances in Land Remote Sensing: System, Modeling, Inversion and Application. Springer Netherlands.

Liang, X., E. F. Wood & D. P. Lettenmaier (1999) Modeling ground heat flux in land surface parameterization schemes. *Journal of Geophysical Research: Atmospheres,* 104**,** 9581-9600.

Linders, J. (2000) Comparison of three different methods to select feature for discriminating forest cover types using SAR imagery. *International Journal of Remote Sensing,* 21**,** 2089-2099.

Liu, L. & Y. Zhang (2011) Urban Heat Island Analysis Using the Landsat TM Data and ASTER Data: A Case Study in Hong Kong. *Remote Sensing,* 3**,** 1535-1552.

Lovell, J. L. & R. D. Graetz (2001) Filtering Pathfinder AVHRR Land NDVI data for Australia. *International Journal of Remote Sensing,* 22**,** 2649-2654.

Lu, D. & Q. Weng (2006) Use of impervious surface in urban land-use classification. *Remote Sensing of Environment,* 102**,** 146-160.

Lu, D. & Q. Weng (2007) A survey of image classification methods and techniques for improving classification performance. *International Journal of Remote Sensing,* 28**,** 823-870.

Lucas, R., A. Rowlands, A. Brown, S. Keyworth & P. Bunting (2007) Rule-based classification of multi-temporal satellite imagery for habitat and agricultural land cover mapping. *ISPRS Journal of Photogrammetry and Remote Sensing,* 62**,** 165-185.

LUNETTA, R. S., BALOGH & M. E. 1999. *Application of multi-temporal Landsat 5 TM imagery for wetland identification*. Bethesda, MD, ETATS-UNIS: American Society for Photogrammetry and Remote Sensing.

Lunetta, R. S., J. F. Knight, J. Ediriwickrema, J. G. Lyon & L. D. Worthy (2006) Land-cover change detection using multi-temporal MODIS NDVI data. *Remote Sensing of Environment,* 105**,** 142-154.

Mahmood, R., R. A. S. R. Pielke, K. G. Hubbard, D. Niyogi, G. Bonan, P. Lawrence, R. McNider, C. McAlpine, A. Etter, S. Gameda, B. Qian, A. Carleton, A. Beltran-Przekurat, T. Chase, A. I. Quintanar, J. O. Adegoke, S. Vezhapparambu, G. Conner, S. Asefi, E. Sertel, D. R. Legates, Y. Wu, R. Hale, O. W. Frauenfeld, A. Watts, M. Shepherd, C. Mitra, V. G. Anantharaj, S. Fall, R. Lund, A. Treviño, P. Blanken, J. Du, H.-I. Chang, R. Leeper, U. S. Nair, S. Dobler, R. Deo & J. Syktus (2010) IMPACTS OF LAND USE/LAND COVER CHANGE ON CLIMATE AND FUTURE RESEARCH PRIORITIES. *Bulletin of the American Meteorological Society,* 91**,** 37-46.

Manandhar, R., I. Odeh & T. Ancev (2009) Improving the Accuracy of Land Use and Land Cover Classification of Landsat Data Using Post-Classification Enhancement. *Remote Sensing,* 1**,** 330-344.

Marçal, A. R. S., J. S. Borges, J. A. Gomes & J. F. Pinto Da Costa (2005) Land cover update by supervised classification of segmented ASTER images. *International Journal of Remote Sensing,* 26**,** 1347-1362.

Martínez, B. & M. A. Gilabert (2009) Vegetation dynamics from NDVI time series analysis using the wavelet transform. *Remote Sensing of Environment,* 113**,** 1823-1842.

Mather, P. & M. Koch. 2010. Computer Processing of Remotely-Sensed Images: An Introduction. Wiley.

Maximov, I. A. 2003. INTEGRATED ASSESSMENT OF CLIMATE AND LAND USE CHANGE EFFECTS ON HYDROLOGY AND WATER QUALITY OF THE UPPER AND LOWER GREAT MIAMI RIVER. University of Cincinnati.

Maxwell, S. K., J. R. Nuckols, M. H. Ward & R. M. Hoffer (2004) An automated approach to mapping corn from Landsat imagery. *Computers and Electronics in Agriculture,* 43**,** 43-54.

Menzel, A. & P. Fabian (1999) Growing season extended in Europe. *Nature,* 397**,** 659-659.

Migliavacca, M., E. Cremonese, R. Colombo, L. Busetto, M. Galvagno, L. Ganis, M. Meroni, E. Pari, M. Rossini, C. Siniscalco & U. Morra di Cella (2008) European larch phenology

in the Alps: can we grasp the role of ecological factors by combining field observations and inverse modelling? *International Journal of Biometeorology,* 52**,** 587-605.

Morisette, J. T., A. D. Richardson, A. K. Knapp, J. I. Fisher, E. A. Graham, J. Abatzoglou, B. E. Wilson, D. D. Breshears, G. M. Henebry, J. M. Hanes & L. Liang (2008) Tracking the rhythm of the seasons in the face of global change: phenological research in the 21st century. *Frontiers in Ecology and the Environment,* 7**,** 253-260.

Müller, B., M. Bernhardt & K. Schulz (2014) Identification of catchment functional units by time series of thermal remote sensing images. *Hydrol. Earth Syst. Sci. Discuss.,* 11**,** 7019-7052.

Murai, H. & S. Omatu (1997) Remote sensing image analysis using a neural network and knowledge-based processing. *International Journal of Remote Sensing,* 18**,** 811-828.

Muttitanon, W. & N. K. Tripathi (2005) Land use/land cover changes in the coastal zone of Ban Don Bay, Thailand using Landsat 5 TM data. *International Journal of Remote Sensing,* 26**,** 2311-2323.

Nemani, R. R., C. D. Keeling, H. Hashimoto, W. M. Jolly, S. C. Piper, C. J. Tucker, R. B. Myneni & S. W. Running (2003) Climate-Driven Increases in Global Terrestrial Net Primary Production from 1982 to 1999. *Science,* 300**,** 1560-1563.

Nilsson, C., J. E. Pizzuto, G. E. Moglen, M. A. Palmer, E. H. Stanley, N. E. Bockstael & L. C. Thompson (2003) Ecological Forecasting and the Urbanization of Stream Ecosystems: Challenges for Economists, Hydrologists, Geomorphologists, and Ecologists. *Ecosystems,* 6**,** 659-674.

Oetter, D. R., W. B. Cohen, M. Berterretche, T. K. Maiersperger & R. E. Kennedy (2001) Land cover mapping in an agricultural setting using multiseasonal Thematic Mapper data. *Remote Sensing of Environment,* 76**,** 139-155.

Ozdogan, M. & G. Gutman (2008) A new methodology to map irrigated areas using multi-temporal MODIS and ancillary data: An application example in the continental US. *Remote Sensing of Environment,* 112**,** 3520-3537.

Palacios-Orueta, A., M. Huesca, M. L. Whiting, J. Litago, S. Khanna, M. Garcia & S. L. Ustin (2012) Derivation of phenological metrics by function fitting to time-series of Spectral Shape Indexes AS1 and AS2: Mapping cotton phenological stages using MODIS time series. *Remote Sensing of Environment,* 126**,** 148-159.

Parmesan, C. & G. Yohe (2003) A globally coherent fingerprint of climate change impacts across natural systems. *Nature,* 421**,** 37-42.

Peñuelas, J., I. Filella, X. Zhang, L. Llorens, R. Ogaya, F. Lloret, P. Comas, M. Estiarte & J. Terradas (2004) Complex spatiotemporal phenological shifts as a response to rainfall changes. *New Phytologist,* 161**,** 837-846.

Pérez-Hoyos, A., F. J. García-Haro & J. San-Miguel-Ayanz (2012) Conventional and fuzzy comparisons of large scale land cover products: Application to CORINE, GLC2000, MODIS and GlobCover in Europe. *ISPRS Journal of Photogrammetry and Remote Sensing,* 74**,** 185-201.

Pettorelli, N., J. O. Vik, A. Mysterud, J.-M. Gaillard, C. J. Tucker & N. C. Stenseth (2005) Using the satellite-derived NDVI to assess ecological responses to environmental change. *Trends in Ecology & Evolution,* 20**,** 503-510.

Pielke, R. A., A. Pitman, D. Niyogi, R. Mahmood, C. McAlpine, F. Hossain, K. K. Goldewijk, U. Nair, R. Betts, S. Fall, M. Reichstein, P. Kabat & N. de Noblet (2011) Land use/land cover changes and climate: modeling analysis and observational evidence. *Wiley Interdisciplinary Reviews: Climate Change,* 2**,** 828-850.

Prentice, I. C., A. Bondeau, W. Cramer, S. P. Harrison, T. Hickler, W. Lucht, S. Sitch, B. Smith & M. T. Sykes. 2007. Dynamic Global Vegetation Modeling: Quantifying Terrestrial Ecosystem Responses to Large-Scale Environmental Change. In *Terrestrial Ecosystems in a Changing World,* eds. J. G. Canadell, D. E. Pataki & L. F. Pitelka, 175-192. Berlin, Heidelberg: Springer Berlin Heidelberg.

Press, W. H., S. A. Teukolsky, W. T. Vetterling & B. P. Flannery. 1996. *Numerical recipes in C.* Cambridge university press Cambridge.

R. Myneni, Y. K., T. Park. 2015a. MOD15A2H MODIS/Terra Leaf Area Index/FPAR 8-Day L4 Global 500m SIN Grid V006. In *NASA EOSDIS Land Processes DAAC.* Sioux Falls, South Dakota: USGS Earth Resources Observation and Science (EROS) Center.

MODIS. 2015b. MODIS Collection 6 (C6) LAI/FPAR Product User's Guide. In *NASA EOSDIS Land Processes DAAC.* Sioux Falls, South Dakota: USGS Earth Resources Observation and Science (EROS) Center.

Reed, B. C., J. F. Brown, D. VanderZee, T. R. Loveland, J. W. Merchant & D. O. Ohlen (1994) Measuring Phenological Variability from Satellite Imagery. *Journal of Vegetation Science,* 5**,** 703-714.

Richards, J. A. & X. Jia. 2006. Remote Sensing Digital Image Analysis: An Introduction. Springer.

Richardson, A. D., A. S. Bailey, E. G. Denny, C. W. Martin & J. O'Keefe (2006) Phenology of a northern hardwood forest canopy. *Global Change Biology,* 12**,** 1174-1188.

Richardson, A. D., T. F. Keenan, M. Migliavacca, Y. Ryu, O. Sonnentag & M. Toomey (2013) Climate change, phenology, and phenological control of vegetation feedbacks to the climate system. *Agricultural and Forest Meteorology,* 169**,** 156-173.

Riha, S., D. Wilks & P. Simoens (1996) Impact of temperature and precipitation variability on crop model predictions. *Climatic Change,* 32**,** 293-311.

Rodriguez-Galiano, V. F., M. Chica-Olmo, F. Abarca-Hernandez, P. M. Atkinson & C. Jeganathan (2012a) Random Forest classification of Mediterranean land cover using multi-seasonal imagery and multi-seasonal texture. *Remote Sensing of Environment,* 121**,** 93-107.

Rodriguez-Galiano, V. F., B. Ghimire, J. Rogan, M. Chica-Olmo & J. P. Rigol-Sanchez (2012b) An assessment of the effectiveness of a random forest classifier for land-cover classification. *ISPRS Journal of Photogrammetry and Remote Sensing,* 67**,** 93-104.

Roerink, G. J., M. Menenti & W. Verhoef (2000) Reconstructing cloudfree NDVI composites using Fourier analysis of time series. *International Journal of Remote Sensing,* 21**,** 1911-1917.

Rozenstein, O. & A. Karnieli (2011) Comparison of methods for land-use classification incorporating remote sensing and GIS inputs. *Applied Geography,* 31**,** 533-544.

Running, S. W., D. D. Baldocchi, D. P. Turner, S. T. Gower, P. S. Bakwin & K. A. Hibbard (1999) A Global Terrestrial Monitoring Network Integrating Tower Fluxes, Flask Sampling, Ecosystem Modeling and EOS Satellite Data. *Remote Sensing of Environment,* 70**,** 108-127.

Running, S. W. & J. C. Coughlan (1988) A general model of forest ecosystem processes for regional applications I. Hydrologic balance, canopy gas exchange and primary production processes. *Ecological Modelling,* 42**,** 125-154.

Saadat, H., J. Adamowski, R. Bonnell, F. Sharifi, M. Namdar & S. Ale-Ebrahim (2011) Land use and land cover classification over a large area in Iran based on single date analysis of satellite imagery. *ISPRS Journal of Photogrammetry and Remote Sensing,* 66**,** 608-619.

Sakamoto, T., M. Yokozawa, H. Toritani, M. Shibayama, N. Ishitsuka & H. Ohno (2005) A crop phenology detection method using time-series MODIS data. *Remote Sensing of Environment,* 96**,** 366-374.

Salovaara, K. J., S. Thessler, R. N. Malik & H. Tuomisto (2005) Classification of Amazonian primary rain forest vegetation using Landsat ETM+ satellite imagery. *Remote Sensing of Environment,* 97**,** 39-51.

Samaniego, L., A. Bardossy & K. Schulz (2008) Supervised Classification of Remotely Sensed Imagery Using a Modified k-NN Technique. *Geoscience and Remote Sensing, IEEE Transactions on,* 46**,** 2112-2125.

Samaniego, L. & K. Schulz (2009) Supervised Classification of Agricultural Land Cover Using a Modified k-NN Technique (MNN) and Landsat Remote Sensing Imagery. *Remote Sensing,* 1**,** 875-895.

Scheiter, S., L. Langan & S. I. Higgins (2013) Next-generation dynamic global vegetation models: learning from community ecology. *New Phytologist,* 198**,** 957-969.

Schulz, K., J. Horn, L. Samaniego & R. Kumar. 2008. Parsimonious LAI-model development from long term MODIS data. In *AGU Fall Meeting Abstracts*, 02.

Schwartz, M. D. (1998) Green-wave phenology. *Nature,* 394**,** 839-840.

Schwartz, M. D., R. Ahas & A. Aasa (2006) Onset of spring starting earlier across the Northern Hemisphere. *Global Change Biology,* 12**,** 343-351.

Schwartz, M. D. & T. R. Karl (1990) Spring Phenology: Nature's Experiment to Detect the Effect of "Green-Up" on Surface Maximum Temperatures. *Monthly Weather Review,* 118**,** 883-890.

Schwartz, M. D., B. C. Reed & M. A. White (2002) Assessing satellite-derived start-of-season measures in the conterminous USA. *International Journal of Climatology,* 22**,** 1793-1805.

Segl, K., S. Roessner, U. Heiden & H. Kaufmann (2003) Fusion of spectral and shape features for identification of urban surface cover types using reflective and thermal hyperspectral data. *ISPRS Journal of Photogrammetry and Remote Sensing,* 58**,** 99-112.

Sexton, J. O., D. L. Urban, M. J. Donohue & C. Song (2013) Long-term land cover dynamics by multi-temporal classification across the Landsat-5 record. *Remote Sensing of Environment,* 128**,** 246-258.

Shalaby, A. & R. Tateishi (2007) Remote sensing and GIS for mapping and monitoring land cover and land-use changes in the Northwestern coastal zone of Egypt. *Applied Geography,* 27**,** 28-41.

Shi, W., C. Zhu, C. Zhu & X. Yang (2003) Multi-Band Wavelet for Fusing SPOT Panchromatic and Multispectral Images. *Photogrammetric Engineering & Remote Sensing,* 69**,** 513-520.

Singh, A. (1989) Review Article Digital change detection techniques using remotely-sensed data. *International Journal of Remote Sensing,* 10**,** 989-1003.

Sitch, S., B. Smith, I. C. Prentice, A. Arneth, A. Bondeau, W. Cramer, J. O. Kaplan, S. Levis, W. Lucht, M. T. Sykes, K. Thonicke & S. Venevsky (2003) Evaluation of ecosystem dynamics, plant geography and terrestrial carbon cycling in the LPJ dynamic global vegetation model. *Global Change Biology,* 9**,** 161-185.

Sobrino, J. A. & N. Raissouni (2000) Toward remote sensing methods for land cover dynamic monitoring: Application to Morocco. *International Journal of Remote Sensing,* 21**,** 353-366.

Song, C., C. E. Woodcock, K. C. Seto, M. P. Lenney & S. A. Macomber (2001) Classification and Change Detection Using Landsat TM Data: When and How to Correct Atmospheric Effects? *Remote Sensing of Environment,* 75**,** 230-244.

Southworth, J. (2004) An assessment of Landsat TM band 6 thermal data for analysing land cover in tropical dry forest regions. *International Journal of Remote Sensing,* 25**,** 689-706.

Steele, B. M., J. C. Winne & R. L. Redmond (1998) Estimation and Mapping of Misclassification Probabilities for Thematic Land Cover Maps. *Remote Sensing of Environment,* 66**,** 192-202.

Stefanov, W. L., M. S. Ramsey & P. R. Christensen (2001) Monitoring urban land cover change: An expert system approach to land cover classification of semiarid to arid urban centers. *Remote Sensing of Environment,* 77**,** 173-185.

Stephenson, N. L. (1990) Climatic Control of Vegetation Distribution: The Role of the Water Balance. *The American Naturalist,* 135**,** 649-670.

Su, Z. (2000) Remote sensing of land use and vegetation for mesoscale hydrological studies. *International Journal of Remote Sensing,* 21**,** 213-233.

SEBS (2002) The Surface Energy Balance System (SEBS) for estimation of turbulent heat fluxes. *Hydrology and Earth System Sciences,* 6**,** 85-100.

Sun, L. & K. Schulz (2015) The Improvement of Land Cover Classification by Thermal Remote Sensing. *Remote Sensing,* 7**,** 8368.

Tesemma, Z. K., Y. Wei, A. W. Western & M. C. Peel (2014) Leaf Area Index Variation for Crop, Pasture, and Tree in Response to Climatic Variation in the Goulburn–Broken Catchment, Australia. *Journal of Hydrometeorology,* 15**,** 1592-1606.

Thuiller, W. (2007) Biodiversity: Climate change and the ecologist. *Nature,* 448**,** 550-552.

Tian, Y., C. E. Woodcock, Y. Wang, J. L. Privette, N. V. Shabanov, L. Zhou, Y. Zhang, W. Buermann, J. Dong, B. Veikkanen, T. Häme, K. Andersson, M. Ozdogan, Y. Knyazikhin & R. B. Myneni (2002) Multiscale analysis and validation of the MODIS LAI product: I. Uncertainty assessment. *Remote Sensing of Environment,* 83**,** 414-430.

Tolson, B. A. & C. A. Shoemaker (2007) Dynamically dimensioned search algorithm for computationally efficient watershed model calibration. *Water Resources Research,* 43**,** W01413.

Tyagi, P. & U. Bhosle (2011) Atmospheric correction of remotely sensed images in spatial and transform domain. *International Journal of Image Processing,* 5**,** 564-579.

USGS. 2013. Remote Sensing Phenology.

Verstraete, M. M., B. Pinty & R. B. Myneni (1996) Potential and limitations of information extraction on the terrestrial biosphere from satellite remote sensing. *Remote Sensing of Environment,* 58**,** 201-214.

Vicente-Serrano, S. M., F. Pérez-Cabello & T. Lasanta (2008) Assessment of radiometric correction techniques in analyzing vegetation variability and change using time series of Landsat images. *Remote Sensing of Environment,* 112**,** 3916-3934.

Viovy, N., O. Arino & A. S. Belward (1992) The Best Index Slope Extraction (BISE): A method for reducing noise in NDVI time-series. *International Journal of Remote Sensing,* 13**,** 1585-1590.

Vuolo, F. & C. Atzberger (2012) Exploiting the Classification Performance of Support Vector Machines with Multi-Temporal Moderate-Resolution Imaging Spectroradiometer (MODIS) Data in Areas of Agreement and Disagreement of Existing Land Cover Products. *Remote Sensing,* 4**,** 3143-3167.

Wang, L. T. & T. L. De Liberty. 2005. Landsat Atmospheric Correction: The Good, the Bad, and the Ugly. In *2005 ESRI International User Conference Proc*.

Watson, D. J. (1947) Comparative Physiological Studies on the Growth of Field Crops: I. Variation in Net Assimilation Rate and Leaf Area between Species and Varieties, and within and between Years. *Annals of Botany,* 11**,** 41-76.

Weiss, M., F. Baret, S. Garrigues & R. Lacaze (2007) LAI and fAPAR CYCLOPES global products derived from VEGETATION. Part 2: validation and comparison with MODIS collection 4 products. *Remote Sensing of Environment,* 110**,** 317-331.

White, M. A. & R. R. Nemani (2006) Real-time monitoring and short-term forecasting of land surface phenology. *Remote Sensing of Environment,* 104**,** 43-49.

White, M. A., P. E. Thornton & S. W. Running (1997) A continental phenology model for monitoring vegetation responses to interannual climatic variability. *Global Biogeochemical Cycles,* 11**,** 217-234.

Wilkinson, G. G. (2005) Results and implications of a study of fifteen years of satellite image classification experiments. *Geoscience and Remote Sensing, IEEE Transactions on,* 43**,** 433-440.

Wilson, E. H. & S. A. Sader (2002) Detection of forest harvest type using multiple dates of Landsat TM imagery. *Remote Sensing of Environment,* 80**,** 385-396.

Wu, B., Q. Fu, L. Sun & X. Wang (2015) Enhanced hyperspherical color space fusion technique preserving spectral and spatial content. *Journal of Applied Remote Sensing,* 9**,** 097291-097291.

Xiao, Q., E. G. McPherson, J. R. Simpson & S. L. Ustin (1998) Rainfall interception by Sacramento's urban forest. *Journal of Arboriculture,* 24**,** 235-244.

Xie, Y., Z. Sha & M. Yu (2008) Remote sensing imagery in vegetation mapping: a review. *Journal of Plant Ecology,* 1**,** 9-23.

Y. Knyazikhin, J. G., J. L. Privette, Y. Tian, A. Lotsch, Y. Zhang, Y. Wang, J. T. Morisette, P.Votava, R.B. Myneni, R. R. Nemani, S. W. Running (1999) MODIS Leaf Area Index (LAI) and Fraction of Photosynthetically Active Radiation Absorbed by Vegetation (FPAR) Product (MOD15) Algorithm Theoretical Basis Document. *http://eospso.gsfc.nasa.gov/atbd/modistables.html*.

Yuan, F., K. E. Sawaya, B. C. Loeffelholz & M. E. Bauer (2005) Land cover classification and change analysis of the Twin Cities (Minnesota) Metropolitan Area by multitemporal Landsat remote sensing. *Remote Sensing of Environment,* 98**,** 317-328.

Zehe, E., U. Ehret, L. Pfister, T. Blume, B. Schröder, M. Westhoff, C. Jackisch, S. J. Schymanski, M. Weiler, K. Schulz, N. Allroggen, J. Tronicke, L. van Schaik, P. Dietrich, U. Scherer, J. Eccard, V. Wulfmeyer & A. Kleidon (2014) HESS Opinions: From response units to functional units: a thermodynamic reinterpretation of the HRU concept to link spatial organization and functioning of intermediate scale catchments. *Hydrol. Earth Syst. Sci.,* 18**,** 4635-4655.

Zhang, L., W. R. Dawes & G. R. Walker (2001) Response of mean annual evapotranspiration to vegetation changes at catchment scale. *Water Resources Research,* 37**,** 701-708.

Zhang, R. & D. Zhu (2011) Study of land cover classification based on knowledge rules using high-resolution remote sensing images. *Expert Systems with Applications,* 38**,** 3647-3652.

Zhang, X., M. A. Friedl & C. B. Schaaf (2006) Global vegetation phenology from Moderate Resolution Imaging Spectroradiometer (MODIS): Evaluation of global patterns and comparison with in situ measurements. *Journal of Geophysical Research: Biogeosciences,* 111**,** n/a-n/a.

Zhang, X., M. A. Friedl, C. B. Schaaf, A. H. Strahler, J. C. F. Hodges, F. Gao, B. C. Reed & A. Huete (2003) Monitoring vegetation phenology using MODIS. *Remote Sensing of Environment,* 84**,** 471-475.

Zhang, X., M. A. Friedl, C. B. Schaaf, A. H. Strahler & Z. Liu (2005) Monitoring the response of vegetation phenology to precipitation in Africa by coupling MODIS and TRMM instruments. *Journal of Geophysical Research: Atmospheres,* 110**,** D12103.

Zheng, G. & L. M. Moskal (2009) Retrieving Leaf Area Index (LAI) Using Remote Sensing: Theories, Methods and Sensors. *Sensors,* 9**,** 2719.

Zhu, G. & D. G. Blumberg (2002) Classification using ASTER data and SVM algorithms: The case study of Beer Sheva, Israel. *Remote Sensing of Environment,* 80**,** 233-240.

Zhu, X., J. Chen, F. Gao, X. Chen & J. G. Masek (2010) An enhanced spatial and temporal adaptive reflectance fusion model for complex heterogeneous regions. *Remote Sensing of Environment,* 114**,** 2610-2623.

Curriculum Vitae

Personal

Name:	Liya Sun
Date of Birth:	03.11.1986
Place of Birth:	Shandong, China
Nationality:	China
Degree:	M.Sc.
Email:	liya.sun@boku.ac.at

School and Education:

2012-2016	Ph.D student at the Department of Geography, LMU Munich.
2011	Master of Science in Cartography and Geography Information System.
	Master thesis: Study on red tide detecting methods based on time series of ocean color remote sensing data.
2008-2011	Spatial Information Research Center, Fuzhou University, Fuzhou, China.
2008	Bachelor of Science in Resources Environment and Management of Urban and Rural Planning.
	Undergraduate thesis: Development of Water Resource Management System of Longkou City.
2004-2008	Jinan University, Jinan, China
1998-2004	Middle School and High School at the Huayang School, Yanggu, China

Projects Involved:

2009-2011	Key Science Project of Fujian Province: Red Tide Prediction Based on Time-series Ocean Color Remote Sensing Data Code: NO.2008Y0050

	Normalization and Integration of Forest LAI in spatial and temporal scales Based on Multi Optical Remote Sensing Data Code: NO. 2009J06024
2012-2015	From Catchments as Organised Systems to Models based on Functional Units, Subproject B. DFG, FOR 1598, SCHU1271/5-1

Scientific Publications:

Sun, L., and K. Schulz, 2016, Vegetation Dynamics Modelling of Temporal LAI Prediction by Integrating the Climate Variables and MODIS LAI Data in a Mesoscale Catchment. Remote Sens. 2016, in review.

Sun, L., and K. Schulz, 2015, Response to Johnson B.A. Scale Issues Related to the Accuracy Assessment of Land Use/Land Cover Maps Produced Using Multi-Resolution Data: Comments on "The Improvement of Land Cover Classification by Thermal Remote Sensing". Remote Sens. 2015, 7, 8368–8390: Remote Sensing, v. 7, p. 13440.

Sun, L., and K. Schulz, 2015, The Improvement of Land Cover Classification by Thermal Remote Sensing: Remote Sensing, v. 7, p. 8368.

Wu, B., Q. Fu, **L. Sun**, and X. Wang, 2015, Enhanced hyperspherical color space fusion technique preserving spectral and spatial content: Journal of Applied Remote Sensing, v. 9, p. 097291-097291.

Wu, B., C. Chen, T. M. Kechadi, and **L. Sun**, 2013, A comparative evaluation of filter-based feature selection methods for hyper-spectral band selection: International Journal of Remote Sensing, v. 34, p. 7974-7990.

Sun, L., Y. Chen, and X. Wang, 2012, Remote Sensing Detection of Red Tide by Time-series MODIS Data : Remote Sensing Information, v.13, n.3, Jun., 2012 (in Chinese)

Sun, L., Y. Chen, and X. Wang, 2010, Comparison of multi-sensor data application in algal bloom detection: 2010 3rd International Congress on Image and Signal Processing (CISP), p. 2144-2148.

Chen, Y., X. Wang, **L. Sun**, and B. Wu, 2010, Application of adaptive weighted averaging method for ocean color data in East China Sea: 2010 3rd International Congress on Image and Signal Processing (CISP), p. 2107-2110.

Sun, L., Y. Chen, and X. Wang, 2009, Red Tide Information Extraction Based on MODIS Data: Remote Sensing Annual Meeting of Fujian Province, 2009, Xiamen, Fujian. (in Chinese)